Winter 12-22-2021

A Solid-State Phase Camera for Advanced Gravitational Wave Detectors

Erik Muniz
Syracuse University

ABSTRACT

From Muñiz et. al. (2021):

I present a novel way of wavefront sensing using a commercially available, continuous-wave time-of-flight camera with QVGA-resolution. This CMOS phase camera is capable of sensing externally modulated light sources with frequencies up to 100 MHz. The high-spatial-resolution of the sensor, combined with our integrated control electronics, allows the camera to image power modulation index as low as -62 dBc/second/pixel. The phase camera is applicable to problems where alignment and mode-mismatch sensing is needed and suited for diagnostic and control applications in gravitational-wave detectors. Specifically, I explore the use of the phase camera in sensing the beat signals due to thermal distortions from point-like heat absorbers on the test masses in the Advanced LIGO detectors. The camera is capable of sensing optical path distortions greater than about two nanometers in the Advanced LIGO input mirrors, limited by the phase resolution. In homodyne readout, the performance can reach up to 0.1 nm, limited by the modulation amplitude sensitivity.

A SOLID-STATE PHASE CAMERA FOR ADVANCED GRAVITATIONAL WAVE DETECTORS

By

Erik A. Muñiz

B.S. California State University, Fullerton, CA, 2016

Dissertation
Submitted in Partial Fulfillment of the Requirements
for the degree of
Doctor of Philosophy in Physics

Syracuse University
December 2021

ACKNOWLEDGEMENTS

To my lovely wife Valora, your love and support mean everything to me. You've helped get me through some of the hardest times in my journey and I will forever be grateful.

Contents

List of Tables

List of Figures

Preface

The work presented in this thesis stems from my participation in the LIGO Scientific Collaboration (LSC). This work does not reflect the scientific opinion of the LSC nor was it reviewed by the collaboration.
LIGO DCC Number: P2100323

Chapter 1

Introduction

For the past five years, the Advanced LIGO and VIRGO gravitational wave detectors have been making observations of compact binary mergers [7, 8]. The first ever gravitational wave detection, GW150914 [9], was marked by the coincident detection of the inspiral and merger of two binary black holes marking the beginning of the field of gravitational wave astronomy. Since then, each of the detectors has undergone two phases of upgrades [2] to improve measurement sensitivity. The subsequent observing runs have yielded over 50 gravitational wave detections from binary collisions [10, 11].

This chapter intends to provide the reader with the necessary background in the field of gravitational wave astronomy with the purpose of motivating the new technologies for gravitational wave detectors, which is the principal topic of this thesis. Section 1.1 begins with a relevant, but brief historical discussion on the birth of gravitational wave metrology. The proceeding sections describe the experimental method of detection as well as design considerations when operating a gravitational wave detector.

1.1 A brief history of gravitational waves

In his theory of general relativity, Einstein correctly predicted the existence and nature of gravitational radiation. He assessed that asymmetric, accelerating bodies would create wave-like distortions in spacetime and that these waves propagate outward at the speed of light – this was the first definition of what we later come to know as *gravitational waves* [12, 13]. In other words, the gravitational field produced

by a moving source does not change instantaneously at arbitrary distances from the source. Therefore, we can consider as a relativistic problem, in which the Special Theory of Relativity tells us that the space-time interval ds between two neighboring points is given by

$$
\begin{aligned}
ds^2 &= -c^2dt^2 + dx^2 + dy^2 + dz^2 \\
&= \eta_{\mu\nu}dx^\mu dx^\nu,
\end{aligned} \tag{1.1}
$$

where $\eta_{\mu\nu}$ is the Minkowski metric for flat space-time and the indices μ and ν, represent the coordinates t,x,y,z from 0 to 3. The same physics carries over to into the General Theory of Relativity; however, we consider that gravity causes the "flat" space-time described by the Minkowski metric to curve. This leads to a very general definition for the space-time interval is

$$
ds^2 = g_{\mu\nu}dx^\mu dx^\nu \tag{1.2}
$$

In the case where spacetime is close to flat, we can apply the weak field approximation to field equations and arrive at a description for curved spacetime:

$$
g_{\mu\nu} = \eta_{\mu\nu} + h_{\mu\nu} \tag{1.3}
$$

The perturbative term, $|h_{\mu\nu}| \ll 1$, describes the deviation from flat spacetime. By choosing to work in the transverse traceless gauge, Einstein's field equation, in vacuum, simplifies to the more familiar wave equation with coordinates defined by freely-falling test masses; where we gloss over some details related to the choice of the coordinate system (gauge choice).

$$
\left(\nabla^2 - \frac{1}{c^2}\frac{\partial^2}{\partial t^2}\right)h_{\mu\nu} = 0 \tag{1.4}
$$

It is often more intuitive to view gravitational wave theory through the lens of electromagnetic theory. In this case, we see that the solution to the wave equation 1.4 has the familiar form of plane wave for a gravitational wave propagating in the z-direction:

$$
h_{\mu\nu} = A_{\mu\nu}e^{i\omega_g t - kx}, \tag{1.5}
$$

$$A_{\mu\nu} = \begin{pmatrix} h_+ & h_\times \\ h_\times & h_+ \end{pmatrix}, \tag{1.6}$$

where $A_{\mu\nu}$ is the amplitude of the gravitational wave and $h_+ = A_{xx} = -A_{yy}$ and $h_\times = A_{xy} = A_{yx}$. Other than the wave-like nature of gravitational waves, the solution also reveals that there are two orthogonal polarization directions, h_+ and h_- associated with the wave. From the constraints imposed in the construction of our coordinate system, the requirements for constructing a detector of gravitational radiation become more obvious. In fact, it was the insight of Pirani[14] in his publication on the significance of the Riemann tensor, that gives us our first clue at a means of measuring gravitational waves:

> It is assumed that an observer can, by the use of light signals or otherwise, determine the coordinates of a neighboring particle in his local Cartesian coordinate system

Pirani's statement implied that light could be used as a metric for measuring the relative distance between coordinate masses. The transition from *gedanken* to gravitational wave detector was ushered in by the development of the Michelson inteferometer [15] and advancements in laser technology. The realization of a gravitational wave detector came in the form of Rai Weiss's quarterly progress report in 1972 where the fundamental noise sources are defined with remarkable precision and the inteferometer design is proposed[16]. In the proceeding chapters, I will detail the basic components of a gravitational wave detector and design considerations and limitations that motivated the advancements to the LIGO detectors in the present day.

1.2   Using Interferometry to Detect Gravitational Waves

The schematic design of a gravitational wave detector begins with understanding that in our gauge choice, gravity does not act as a force; but rather is a result of motion through space-time. Therefore, a set of freely-falling masses would not accelerate in the presence of a gravitational wave and can be used to define a coordinate system
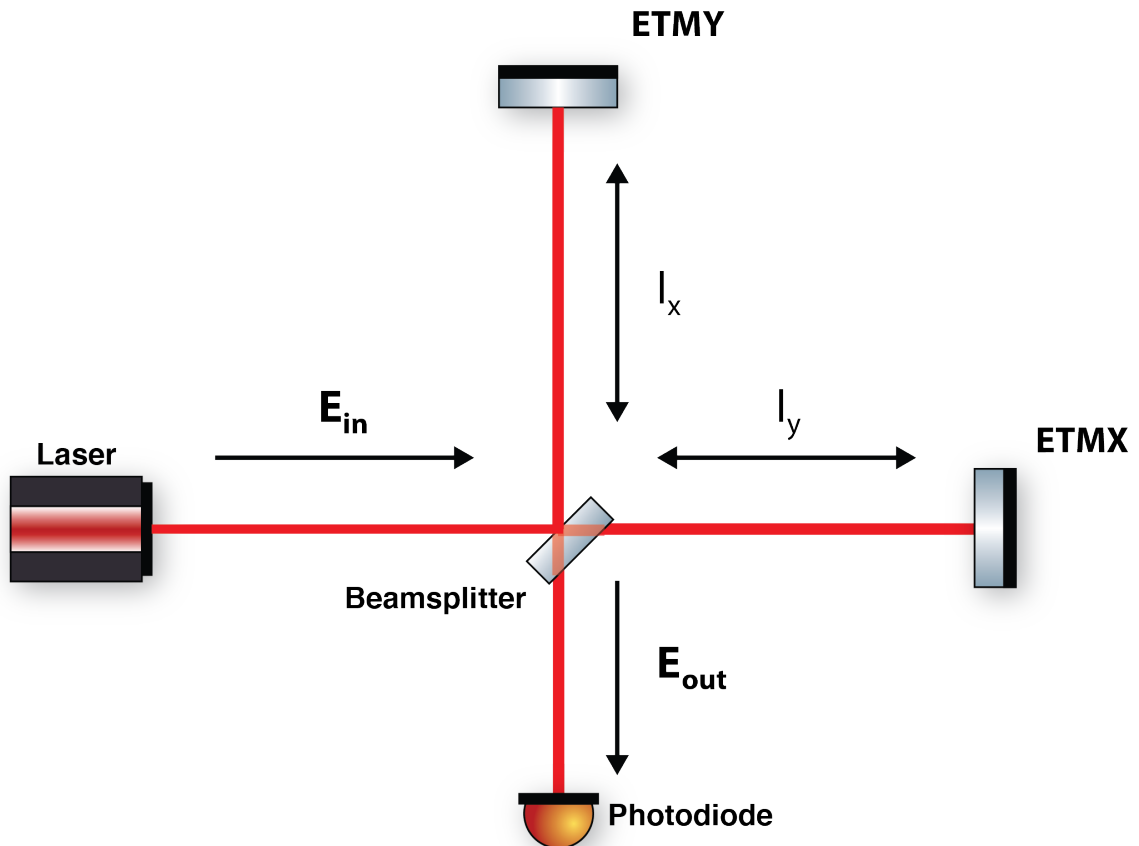
Figure 1: **The Michelson Interferometer** consists of an incident electric field that is partially reflected and transmitted from the beam splitter. As the two light beams propagate along the adjacent arms, they accumulate a phase proportional to the length of each arm. The recombined output field is a superposition of the *single-bounce* fields in the $\hat{x}$ and $\hat{y}$ directions.

in space-time. Relativity tells us that it is possible to use the light travel time between a set of coordinate test masses to get a measure of the distance between them. Consider the light propagation starting at the beam splitter in the simple Michelson interferometer in Fig 1. From principles of Special Relativity, we know neighboring events linked by a light beam are considered lightlike. Thus, the proper length is given by

$$ds^2 = 0. \tag{1.7}$$

We can simplify the math without loss of generality by choosing our axes such that each of the detector arms are aligned with both the $\hat{x}$ and $\hat{y}$ directions, respectively. If we only consider propagation along the arm in the $\hat{x}$-axis then the space-time interval is given by

$$
\begin{aligned}
ds^2 = 0 &= g_{\mu\nu}dx^\mu dx^\nu \\
&= c^2 dt^2 - (1 + h_+)dx^2
\end{aligned}
\tag{1.8}
$$

Rearranging,

$$
\begin{aligned}
\frac{dt}{dx} &= \frac{1}{c}\sqrt{1 + h_+} \\
&\approx \frac{1}{c}\left[1 + \frac{1}{2}h_+\right].
\end{aligned}
\tag{1.9}
$$

The time required for light to reach the end mirror (for an initial time of t = 0) is then given by

$$t_1 = \frac{1}{c}\int_0^{l_x}\left[1 + \frac{1}{2}h_+(x)\right]dx, \tag{1.10}$$

where l_x is the length of the x-arm. Therefore, the total round trip time for the light in the x-arm is

$$t_{rt_x} = \frac{2l_x}{c} + \frac{1}{2c}\int_0^{l_x}[h_+(x) + h_+(x + l_x)]\,dx \tag{1.11}$$

The round trip time of light along the y-arm is given by

$$t_{rt_y} = \frac{2l_y}{c} - \frac{1}{2c}\int_0^{l_y}[h_+(y) + h_+(y + l_y)]\,dx \tag{1.12}$$

In the case that the gravitational wave period is much larger than the round trip of light in the interferometer (i.e. $2\pi f_{gw} t_{rt} \ll 1$), the perturbation can be approximated as constant, or $h_+(\eta_i) \approx h_+(\eta_i + l_i) = constant$). Therefore, we can calculate the difference in travel time between the arms as

$$\Delta\tau = t_{rt_x} - t_{rt_y} = \frac{2l}{c} h_+ \tag{1.13}$$

where $l_x = l_y = l$. The measurable quantity of interest is the differential phase shift, which is related to the round trip time by $2\pi f$, where f is the frequency of the light in the interferometer:

$$\Delta\Phi = \Phi_x(t_{rt_x}) - \Phi_y(t_{rt_y}) = \frac{4\pi l}{\lambda} h_+ \tag{1.14}$$

This reveals that the measured phase shift produced by a gravitational wave is related to the phase accumulation of light in a round trip of the interferometer arms by a fractional amount h_+.

1.2.1 Basic Michelson Configuration

In the previous section, I showed that a gravitational wave propagating along the $\hat{z}$ direction of an interferometer can produce a differential phase shift at the output of the arms. By design, the Michelson interferometer acts as a transducer for differential phase shift to optical power fluctuations at the output. This is precisely the effect we want to measure.

Consider the basic Michelson interferometer configuration shown in Fig 1. If we place our origin at the beam splitter, then the incident monochromatic light source has the form $E_{in} = E_0 e^{i\omega t}$. The effect of the beam splitter is to equally split the beam along two adjacent paths. Thus, the incident field experiences a factor of $r = 1/\sqrt{2}$ in reflection and $t = i/\sqrt{2}$ in transmission of the beam splitter. Additionally, the reflection off the end test masses produces an additional π phase shift; however, this term is canceled out because the effect is common to both arms. Therefore, after one round trip through the interferometer, the respective fields at the output are given by

$$E_x = \frac{i}{2} E_{in} e^{-2ik_x l_x}, \tag{1.15}$$

$$E_y = \frac{i}{2} E_{in} e^{-2ik_y l_y} \tag{1.16}$$

Notice that the input field E_{in} accumulates a phase of $2kl$ for a single round trip in each of the respective interferometer arms. We can then write the total field at the output as a superposition of the individual fields in each of the arms $E_{out} = E_x + E_y$. Because we are actually measuring the output power on a photodiode, we must integrate the beam intensity $I \propto |E_{out}|^2$ over the area of the photodiode:

$$P_{ASY} = \int_A I dA = P_{in} \cos^2(\Delta\Phi), \tag{1.17}$$

where $\Delta\Phi = \phi_x - \phi_y = k_x l_x - k_y l_y$. Equation 1.17 shows that the relative length change between the two arms produces a fluctuation of power at the output port. It follows that if a gravitational wave incident on the interferometer caused a small shift in the differential arm length, then the power at the output can be approximated as $P_{ASY|bright} \approx P_{in}(1 - \Delta\Phi^2)$. Consequently, this means that the DC term dominates the measured output power, making it difficult to measure the fluctuation due to a small phase shift. From a technical standpoint, operating on a bright fringe also couples laser intensity noise into the output.

Alternatively, one can consider introducing a phase difference of $\pi/2$ between the arms, such that the light at the output undergoes complete destructive interference. Conservation of energy also requires that there is power reflected back toward the laser when there is a $\pi/2$ phase difference between the arms (upgrades to the base interferometer which mitigate this effect will be discussed in the next section). In this case, we are operating on a complete *dark fringe*, which means measuring a second order fluctuation in the power produced by an already infinitesimally small change in length.

$$P_{ASY|dark} = P_{in} \sin^2(\Delta\Phi) \approx P_{in}(\Delta\Phi^2) \tag{1.18}$$

1.3 A brief overview: Readout Schemes

In this section I will provide an introductory discussion for various readout methods as applied to the simple michelson interferometer in Section 1.2.1. Figure 2 illustrates each of the different readout schemes: heterodyne, homodyne, and DC readout. In
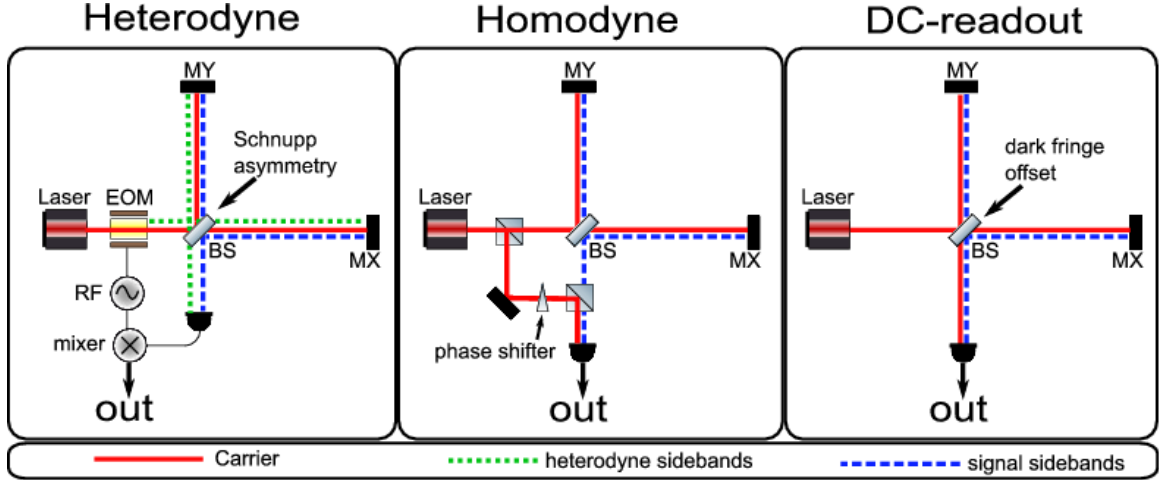
Figure 2: Various readout schemes in gravitational wave interferometry [3].

each of these readout schemes, a strong case is made for operating the interferometer on a dark fringe. If instead the desired measurement is of a "zero", or *null*, then this proves to be a viable measurement method. Immediately, this would ensure that the measured output is independent of fluctuations in the laser power. When operating on a dark fringe the carrier, with frequency f_c, is suppressed at the output, instead, the relative beat between carrier and gravitational wave sidebands f_{gw} is measured at the output: $f_{sig} = f_c \pm f_{gw}$. All of these methods require an optical local oscillator field to produce a significant amplitude modulation of the power measured at the anti-symmetric port.

1.3.1 Heterodyne readout

Heterodyne detection methods often involve a phase modulation of the input carrier field. This is typically performed using an electro-optic modulator (EOM), which adds radio frequency (RF) sidebands (f_{sb}) at $\pm$ the carrier frequency. The frequency offset ensures that the sideband fields accumulate phase differently from the carrier as they propagate through the interferometer. The difference in accumulated phase results in the leakage of the sideband field at the anti-symmetric port if a small differential offset is introduce between the arms of the interferometer (colloquially known as the *Schnupp Asymmetry* [17]).

Recall Equation 1.17, if we introduce a path difference the arms such that $\Delta\Phi =$

$k\Delta l = \pi/2$, this ensures that the bright carrier field at the output destructively interferes. Therefore, the RF sidebands act as a optical reference oscillator for the output field resulting in a beat term at $f_{sb} \pm f_{sig}$. All higher frequency terms (2ω terms), are subsequently filtered by the low bandwidth of the receiver electronics. In Figure 2, a photodiode with an RF amplifier is used to measure the heterodyne beat signal, which is proportional to a voltage signal. The output voltage is demodulated (mixed with the same reference signal used to drive the EOM) at the heterodyne frequency to extract the baseband gravitational wave signal.

One caveat of the heterodyne detection method is that the appropriate *demodulation phase* ϕ_{demod} must be configured via some adjustment of cable length or other method of tuning phase, in order to ensure the appropriate sin or cos function is mixed with the output. The in-phase (I) and quadrature (Q) sampling of the signal during demodulation introduces an undesirable oscillatory term in the shot noise of a heterodyne readout (for a comprehensive description of this effect refer to [18]). For this reason, and many others that will be made apparent, heterodyne readout is not used in modern-day gravitational wave interferometers; however, there are other applications for heterodyne sensing methods which will be introduced in Section 1.5.

1.3.2   Homodyne readout

Here I discuss a traditional homodyne readout for breadth of discussion; however, this method is not directly employed as a readout scheme for advanced gravitational wave interferometers. In the homodyne readout scheme, part of the carrier field is split at the input of the interferometer and is used as a reference LO oscillator at the output. When a gravitational wave produces a differential change in the arms, the audio frequency sidebands interfere with the phase shifted optical reference LO. This method has the advantage that ϕ_{demod} can be dynamically tuned along the optical path, removing the need for any additional electronics.

The immediate drawback of this method is that laser intensity noise couples directly into the readout as in the simple Michelson scheme previously mentioned. Additionally, the added optical path requires precise alignment and control schemes, which contribute to additional noise coupling in the interferometer and provide and pathway for additional optical loss. Although traditional methods of homodyne detection are not practical for gravitational wave detection, one important advantage

of homodyne readout is the feasibility of achieving quantum-limited measurement through squeezed states of light [19].

1.3.3   Special Case of Homodyne readout: DC readout

DC readout is a special case of homodyne readout, where a small asymmetry, typically on the order of a few picometers is introduced between the arms of the interferometer. In this case, the interferometer is operated slightly off the dark fringe (*dark fringe offset*), which allows the carrier field to leak into the output and serve as an optical reference oscillator. Consider the introduction of a static offset between the arms, $\Delta\Phi_{DC}$, then the bright fringe operation defined in Equation 1.17 can be described by:

$$P_{ASY} \propto P_{in}(1 + 2\Delta\Phi_{GW}\Delta\Phi_{DC}) \tag{1.19}$$

Here we observe that the mixing of the reference field with the gravitational wave sidebands creates an amplitude modulation of the output power that scales linearly with the gravitational wave amplitude. The main drawback to DC readout is that noise couples directly into the readout as an amplitude modulation of the gravitational wave sideband. Noise is not necessarily limited to laser intensity noise in this case; misalignment and *point defects* can also degrade the readout. With that said, second generation detectors benefit from highly stabilized lasers with reduced intensity noise and using optical cavities helps ensure the purity of the beam at the readout.

One significant benefit of the DC readout scheme is that the optical LO path is intrinsic to the interferometer, meaning that no additional alignment is needed for ensuring that the LO remain along the carrier path. This also means that the readout phase is fixed with the static offset introduced between the interferometer arms. DC readout remains the current readout method used in the advanced LIGO detectors.

It is worth mentioning a fourth readout method, known as "balanced homodyne readout" [20], which improves upon the DC readout method. Much like the traditional homodyne readout, an additional optical path is used to generate the optical LO. The optical LO and the field at the ASY are combined on a 50/50 beamsplitter, which the power is then measured on two photodiodes placed in reflection and transmission of the beamsplitter. The "balanced" readout comes from the fact that the dominant DC power and subsequent noise couplings appear as the sum of the measured power

on the photodiodes, while the gravitational wave signal appears as the difference. Balanced homodyne detection is currently planned for third generation detectors as an upgrade to facilitate the implementation of squeezed light states for quantum noise reduction [20].

1.4   The Advanced LIGO Detector

The advanced LIGO detector features upgrades to improve sensitivity and extend the frequency bandwidth of the simple Michelson interformeter. The advanced interferometer is comprised of two main resonant cavities and two complementary cavities as shown in Figure 3. The addition of two input test mirrors in the Michelson create Fabry-Perot cavities in each of the arms. Therefore, the Fabry-Perot Michelson increases the effective arm length in the interferometer by building up power in the arms. The power buildup in the arm cavities effectively increases the signal strength at ASY proportional to the gain of the cavity. Additionally, this also results in a reduction of shot noise by the same factor. This will be discussed in more detail in the next section.

The power recycling mirror (PRM) is added between the laser and the beamsplitter to increase effective laser power in the interferometer. The power recycling cavity (PRC) is tuned such that the light reflected from the interferometer is in phase with the incident light. Additionally, a signal recycling mirror (SRM) is placed at the ASY port to tune the frequency response of the detector. The signal recycling cavity (SRC) serves to enhance the gravitational wave signal measured at the output of the interferometer. The following sections discuss ways in which these optical cavities improve sensitivity in the advanced LIGO detector.

1.4.1   Fabry-Perot Cavities

Eqn. 1.14 tells us that sensitivity to gravitational waves is proportional to the differential change in length of the arms. Therefore, increasing the length of the arms is a way to improve sensitivity to gravitational wave signals. One way of achieving this and meeting the practical limitations of detector design, is to design an optical resonator, or Fabry-Perot cavity, in each of the arms. By setting the distance between the arms to be half-integers of the wavelength of the incident light, the light incident
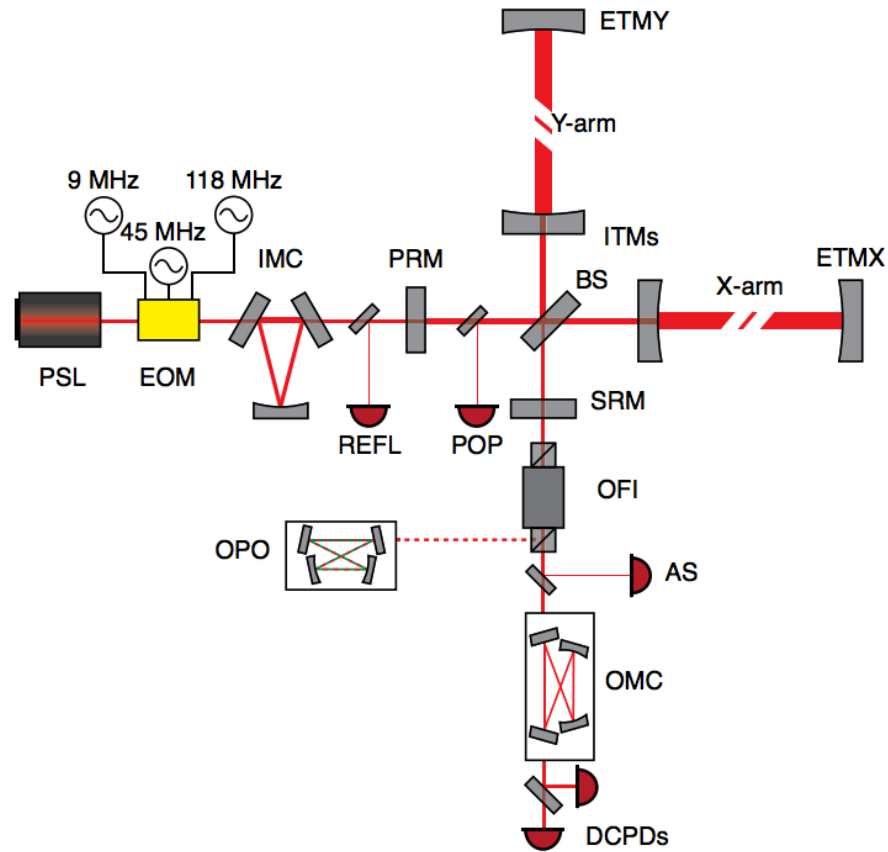
Figure 3: A simplified design scheme of the Advanced LIGO detector during O3 [2]. The input laser is a pre-stabilized Fabry-Perot Nd:YAG laser. A phase modulation electro-optic modulator (EOM) adds sidebands to the main beam at three radio frequencies used for length and angular control. An input mode cleaner (IMC) is then used to clean the spatial modes of the laser, allowing only the fundamental mode to resonate; along with the sidebands. Arm cavities are formed from the input test masses (ITMs) and end test masses (ETMs). The power recycling mirrors (PRM) signal recycling mirrors (SRM), and beamsplitter (BS) form composite cavities with the main arm cavities and work to enhance resonant power buildup and tune frequency dependence. Power is picked off in reflection of the power recycling mirror (REFL) and in the power recycling cavity (POP) for sensing and control of auxiliary degrees of freedom. An output Faraday isolator (OFI) is positioned at the anti-symmetric (AS) port to prevent any back reflected light from reentering the interferometer. The OFI is also used to inject squeezed light from the optical parametric oscillator (OPO). The output mode cleaner (OMC) is a bow-tie cavity, which filters higher order spatial modes at the AS port. The output photodiodes (DCPDs) measure the gravitational wave signal in the differential arm length (DARM).
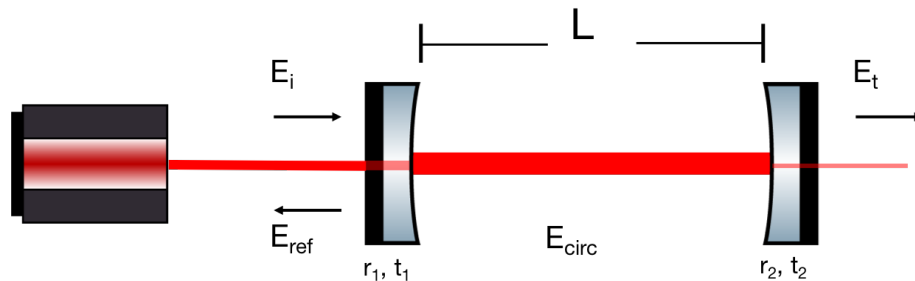
Figure 4: Representation of the carrier field as it propagates through a Fabry-Perot cavity.

on the cavity and the light circulating throughout the cavity constructively interfere. The light is effectively "trapped" in the cavity and optical power is increased.

To see how this is works, consider the schematic diagram of the Fabry-Perot cavity in Figure. 4 – we can ignore the transverse direction of light in this example since we are only concerned with the longitudinal propagation and accumulated phase. In this configuration monochromatic light, E_i, enters a two mirror cavity of length L, with the input and end mirrors having reflection and transmission coefficients of: r_1, t_1, r_2, t_2, respectively. Some of the light is reflected off the first input mirror, E_{ref}, and another fraction is transmitted through into the cavity. A fraction of this light is transmitted through the end mirror of the resonator, E_t, and another fraction of the light is reflected back toward the input mirror of the cavity. The successive bounces of light between the mirrors of the cavity can be represented as a geometric series. Therefore, we can represent the reflection and transmission coefficients, as well as the cavity gain as:

$$r_{FP} = \frac{E_r}{E_t} = -r_1 + \frac{t_1^2 r_2 e^{-i2kL}}{1 - r_1 r_2 e^{-i2kL}}, \tag{1.20}$$

$$t_{FP} = \frac{E_t}{E_i} = \frac{t_1 t_2 e^{-ikL}}{1 - r_1 r_2 e^{-i2kL}}, \tag{1.21}$$

$$g_{FP} = \frac{E_{cav}}{E_i} = \frac{t_1}{1 - r_1 r_2 e^{-i2kL}} \tag{1.22}$$

The power reflectivity and transmissivity, in Figure 5a,45b and the phase of the light, in Figure 5c, are plotted as a function of the cavity shift off resonance. As the cavity

length is sweeped, the point at which the maximum amount of power is reflected and transmitted by the Fabry-Perot cavity, known as resonance, is given by the condition $(kL = \pi n)$. Here, the maximum gain of the cavity is also achieved and the phase of the incident light goes through a full 360^{circ} phase shift.

The sign of the reflected light as the cavity passes through resonance is an important for gravitational wave detector operation. To illustrate this consider the reflectivity of the lossless $(r_1 + r_2 = 1)$ cavity in Equation. 1.20 at resonance.

$$r_{FP}(0) \approx \frac{-r_1 + r_2}{1 - r_1 r_2} \tag{1.23}$$

The advanced LIGO detectors are designed such that the reflectivity of the ETM is greater than the ITM (or $r_1 < r_2$ for our Fabry-Perot cavity). If we consider this case of Equation 1.23, then, a majority of the light leaks back through the ITM on resonance and the cavity is said to be *over-coupled*. Another special case with relevance to gravitational wave detection is when $r_1 = r_2$. This type of cavity is deemed as *critically-coupled* and all of the incident light is transmitted through the end mirror. This cavity design sees application in LIGO *mode cleaner* cavities, which help removed unwanted spatial modes from the fundamental beam.

Another relevant parameter that characterizes a Fabry-Perot cavity is the sharpness of the resonance peak, or the *finesse* $\mathcal{F}$. Finesse is defined as the ratio of free spectral range $\nu_{FSR} = c/2L$, or spacing between resonance peaks, to the cavity linewidth, or full-width at half maximum. This is represented mathematically as follows

$$\mathcal{F} = \frac{\nu_{FSR}}{FWHM} = \frac{\pi \sqrt{r_1 r_2}}{1 - r_1 r_2} \tag{1.24}$$

Notice that the expression in Equation 1.24 depends entirely on the reflectivities of the mirrors. The higher the mirror reflectivities, the more prominent the resonance peak. In the case where $r_2 = 1$ This directly translates to an enhancement of the cavity storage time τ_{FP} by a factor of $\mathcal{F}/2\pi$ written as

$$\tau_{FP} = \frac{L}{c} \frac{\mathcal{F}}{\pi} \tag{1.25}$$

Therefore, the effective length of the cavity increases proportionally with higher finesse (*this is only true until the gravitational wave period reaches storage limit of*
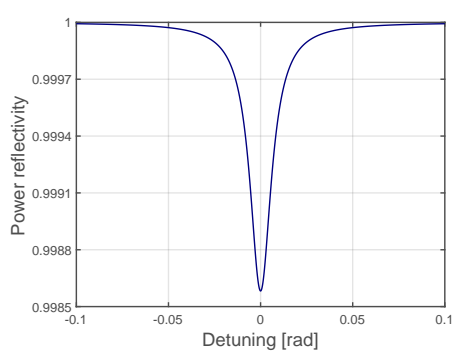
(a) Power reflectivity $|r_{FP}|^2$
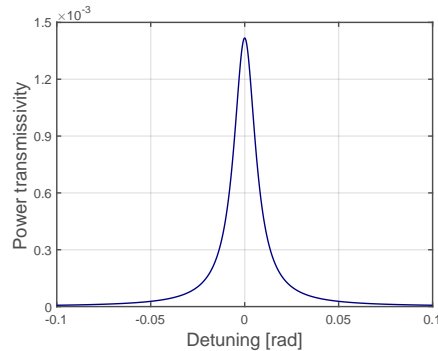
(b) Power transmissivity $|t_{FP}|^2$
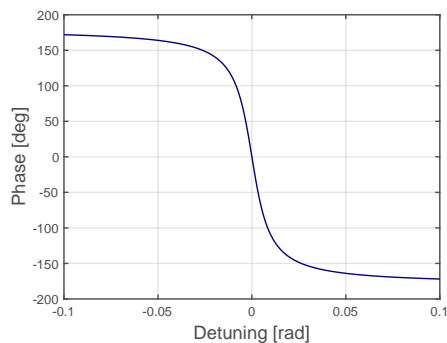
(c) Phase
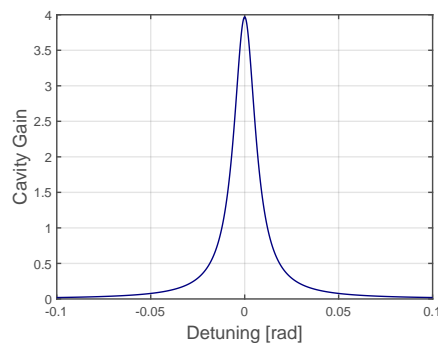
(d) Cavity gain

Figure 5: A lossless over-coupled cavity ($r_1 < r_2$ similar to the arm cavity in aLIGO. The power in each case is normalized by the total incident power. This cavity has a finesse of 450. Each plot considers only a single *fsr* of the cavity. (a) The fractional power reflected from the cavity as a function of the shift off resonance. (b) The fractional power transmitted from the cavity as a function of the shift off resonance. (c) Phase shift of light in the cavity as a function of the shift off resonance. (d) Cavity gain as a function of the shift off resonance.

the cavity). Converting this into improvement in phase sensitivity simply involves multiplying $\mathcal{F}/2\pi$ by a factor of 4. It is worth noting that any noise associated with the displacement of the cavity mirrors also increases by a factor of the finesse as well. Discussion on methods for mitigating optical losses from cavity misalignments and degradation of the phase signal will be elaborated on in later sections.

1.4.2 Power Recycled Fabry-Perot Interferometer

One significant consequence of choosing an operating point near the dark fringe, is that conservation of energy requires that all the light be reflected back toward the symmetric port. A more efficacious use of this reflected power would be to reinject it back into the Fabry-Perot Michelson (FPM). The solution is simple when considering that the Fabry-Perot Michelson can be seen as a effective cavity with frequency dependence (Fig. 6). Then, by positioning mirror between the laser and the FPM at a length l_{PRC}, we can create another cavity such that the light reflected from the FPM constructively interferes with the light coming from the laser. Fritschel et. al [21] show that placing a "recycling" mirror at the symmetric port increases the optical gain of the FPM, thus reducing shot noise.

To determine the gain of the power-recycling FPM, we can use Eqn. 1.22 in the case where the reflectivity of the second mirror is given by the composite reflectivity of the FPM r_{FPM}. The input mirror is simply a partially transmitting mirror with a reflectivity r_p. If we consider the light transmitted through the end mirror of the FPM as an optical loss $\mathcal{L}_{FPM}$ of the power recycling cavity, then conservation of energy tells us

$$r_{FPM} = 1 - \frac{N_{FPM}}{2}\mathcal{L}_{FPM}, \tag{1.26}$$

where the loss scales with the round trip number of bounces in the cavity N_{FPM}[1]. Plugging this into Eqn. 1.22, the power gain in the power-recycled cavity takes the form

---

[1]The effective number of bounces in a Fabry-Perot cavity is related to the finesse of the cavity by

$$N = \frac{2\mathcal{F}}{\pi} \tag{1.27}$$
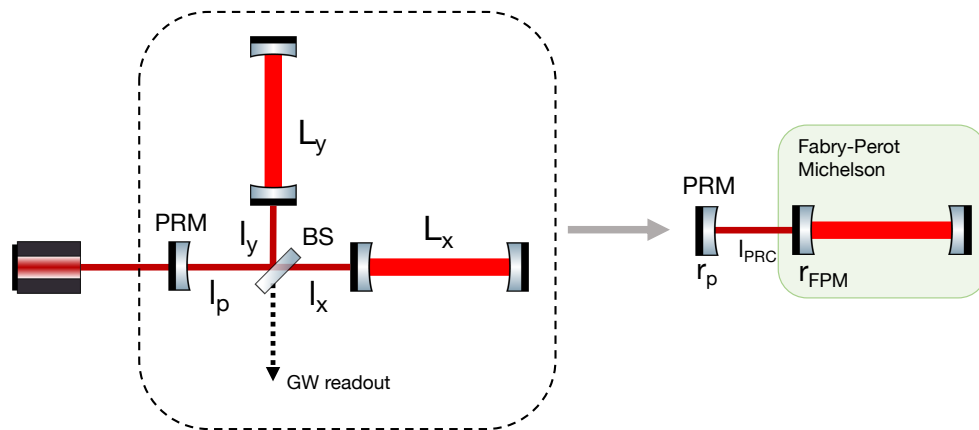
Figure 6: **A power-recycled Fabry-Perot Michelson inteferometer**. In this configuration, a mirror *PRM*, having a reflectivity of r_p is added to the symmetric port at a distance l_p from the beamsplitter. This forms a coupled cavity between the Fabry-Perot Michelson interferometer and the PRM. the effective length of the cavity is given by $l_{PRC} = l_p + \frac{l_x + l_y}{2}$

$$G_{PRC} = \frac{P_{PRC}}{P_{in}} = \frac{1 - r_p^2}{\left[1 - r_{PRM}(1 - \frac{N_{FPM}}{2}\mathcal{L}_{FPM})\right]^2} \tag{1.28}$$

By differentiating Eqn. 1.28 with respect to r_p and setting the derivative equal to zero, we can determine where the gain is maximized. The gain is maximized when $r_p = 1 - r_{FPM}$ and to first order we see

$$G_{PRC}^{max} \approx \frac{1}{N_{FPM}\mathcal{L}_{FPM}} \tag{1.29}$$

or that gain is inversely proportional to the total loss in the FPM. This reveals that the optical losses in the FPM must be kept low to realize significant gain of the PRC.

The power recycling cavity does not alter the frequency response of the interferometer. In the same sense, the phase shift produced by a gravitational wave is not increased by the addition of a power recycling cavity. This can be reasoned heuristically by considering that the gravitational wave sidebands only appear in the signal at the anti-symmetric port. Therefore, only the power of the carrier is the enhanced by the power recycling gain. This also results in a reduction of the shot noise of a power-recycled interferometer by $1/G_{PRC}$. The next section will discuss ways in which the frequency response is tailored in the aLIGO detector.

1.4.3 Dual-Recycled Fabry-Perot Interferometer

Signal Recycled FPMI

It was shown in the previous section that with power recycling, the circulating carrier power is increased by adding a mirror at the symmetric port. A similar technique involving recycling can be used to enhance the power in the gravitational wave signal sideband. By placing a partially-reflective, signal recycling mirror (SRM), at the output port, a resonant cavity is formed which increases the storage time of the gravitational wave signal sidebands [22], thus increasing sensitivity below the cavity pole frequency.

If we consider the power recycling cavity operating in tandem, then the result is a dual-recycled FPMI, with increased carrier power in the arms and higher sensitivity to gravitational wave signal sidebands. One drawback of this method, is that increased storage time of the gravitational wave signals means the interferometer operates in
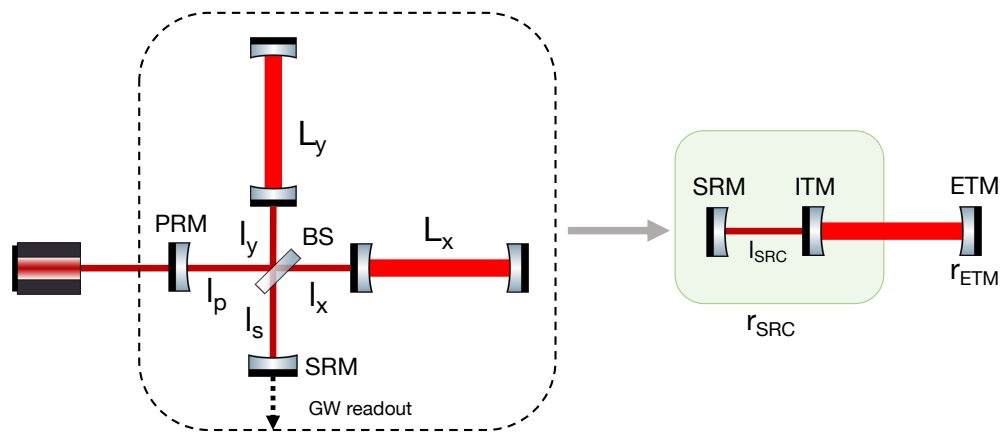
Figure 7: **A dual-recycled Fabry-Perot Michelson inteferometer**. This modification is one of the defining changes made in the transition from initial LIGO to aLIGO. In this configuration, a signal recycling mirror SRM, is added at the anti-symmetric port at a length l_s from the beamsplitter. The signal recycling mirror forms a coupled cavity with the two inner test masses, which "traps" the gravitational wave signal sidebands. The light sees the SRM and ITMs as have a composite reflectivity of r_{SRC}. The effective length of the cavity is given by $l_{SRC} = l_s + \frac{l_x + l_y}{2}$

a much more narrower frequency bandwidth, which is not always ideal for detection. The next section, discusses ways in which the signal-recycling cavity is tuned to allow for a much more broadband detector response.

Resonant Sideband Extraction

Resonant sideband extraction is a technique which decreases the signal storage time of the gravitational wave sidebands in the arm cavity, while increasing the carrier power [23]. It is the current technique of signal enhancement used by advanced LIGO detectors.

To see how it works, consider the light propagating toward the ITM after reflecting off the ETM in Figure 7. The reflectivity *seen* by the light in this case represents the combined reflectivities of the SRC and ITM, r_{SRC}. Additionally, we know that when a gravitational wave modulates the circulating light in the arm cavities, it generates sidebands that are offset at a frequency f_{gw}. Therefore, the signal sidebands and carrier light can be made to see very different cavities depending on the microscopic tuning of the length of the SRC. In this case, it is possible to lower the finesse of the signal sidebands in the arm cavity, while increasing the finesse for the carrier light. This also ensures that much of the carrier power is trapped in the arms of the interferometer and doesn't exit through the input mirrors, mitigating the effects of thermal absorption in the substrates of the test masses. The consequences of high power operation, will be highlighted in detail in later sections.

1.5   Length Control and Alignment Sensing in LIGO

In previous sections, the layout of the aLIGO system was discussed as being composed of a large network of coupled optical cavities with suspended optics. In order to effectively measure the distances between the test masses to integer multiples of the light wavelength, techniques for reducing motion along the seven degrees of freedom in the interferometer have to be employed. The requirement for aLIGO is that the longitudinal motion for aLIGO to be controlled to less than a picometer[7]. In this section, I will discuss the cornerstone method for active length control in aLIGO and elaborate on how this is generalized for a large-scale dual-recycled Fabry-Perot Michelson Interferometer (DRFPMI).

1.5.1   The Pound-Drever-Hall Technique
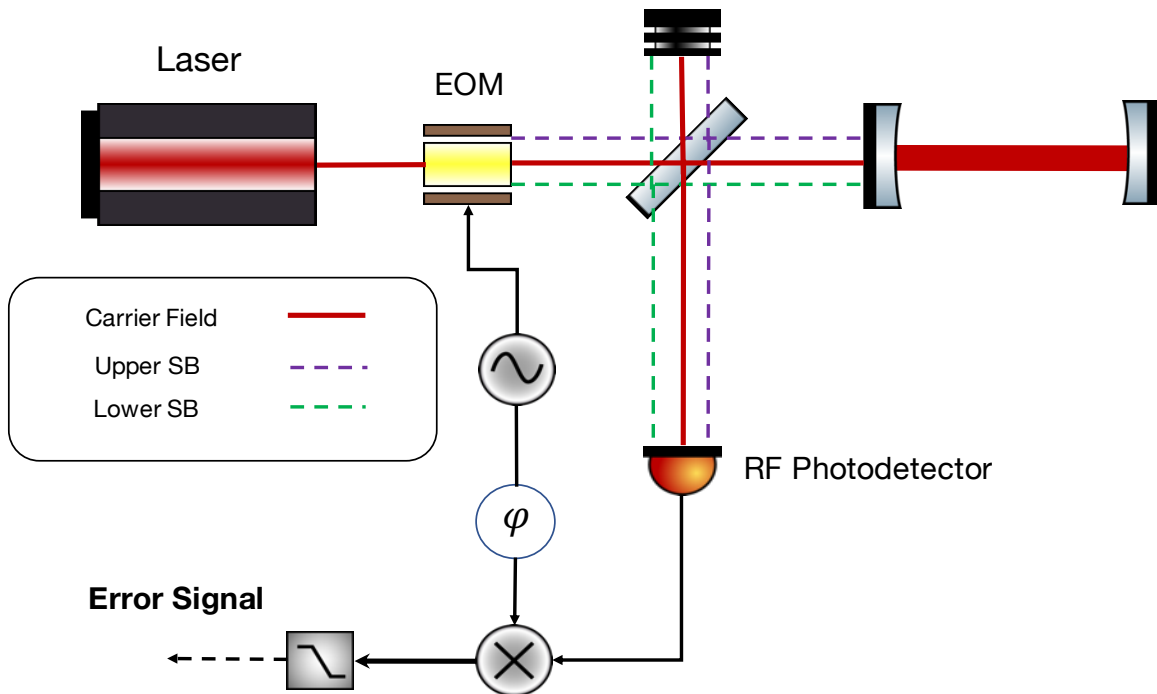
Figure 8: Illustration of the Pound-Drever-Hall locking scheme used to achieve resonance in a Fabry-Perot cavity. The phase modulated sidebands undergo a separate round-trip phase propagation as they are reflected from the cavity on resonance, thus acting as a reference field. When the cavity is offset from resonance the immediately reflected sidebands and carrier field are optically-mixed and detected by the photodiode. The resulting phase difference between the carrier and sideband fields appears as a modulation of the incident power on the photodiode.

The fundamental application of the Pound-Drever-Hall (PDH) technique is to stabilize the laser frequency and ensure that fluctuations in the laser frequency from the linewidth are mitigated. From an application standpoint, PDH works by using the phase relationship between an optical carrier field and RF modulated sidebands to keep a cavity on resonance. This also ensures, that any technical laser noise is decoupled from laser frequency fluctuations. To see how this works, consider that the carrier field $E_c = E_0 e^{i\omega_c t}$ incident on a symmetric cavity with no losses (as shown in Figure 8). The incident light is phase modulated using an electro-optic modulator

(EOM), which adds sidebands at a frequency of $\pm\Omega$[2]. Therefore, the field incident on the cavity is given by:

$$E_{in} = E_c e^{i\Gamma \sin(\Omega t)} \tag{1.30}$$

$$\approx E_c(1 + i\Gamma \sin(\Omega t) \tag{1.31}$$

$$= E_c \left[1 + \Gamma \left(\frac{e^{i\Omega t} - e^{-i\Omega t}}{2}\right)\right], \tag{1.32}$$

where here it is assumed that the modulation index Γ is kept relatively small ($\Gamma << 1$) such that only the carrier and first order sidebands are dominant. The modulation frequency is such that the sideband frequency sits outside the bandwidth of the cavity. This is done such that the when the cavity is resonant on the carrier, the sidebands are rejected from the cavity. By applying the reflection coefficient for the cavity to the sidebands, Equation 1.20, we can show how the cavity response differs:

$$r_{sb\pm} = -r_1 + \frac{t_1^2 r_2 e^{-i2(k+k_\Omega)L}}{1 - r_1 r_2 e^{-i2(k+k_\Omega)L}} \tag{1.33}$$

Here k_Ω is the sideband wavenumber at the given modulation frequency. The reflected field is given by the heterodyne beat between the carrier and sidebands. In terms of the optical power, this represents an amplitude modulation of the optical power at the modulation frequency (The formal derivation is provided in Black [24]). The measured optical power is then converted into a photocurrent. The output signal is demodulated using a mixer, which extracts the modulated signal to baseband. All frequencies above DC are subsequently filtered out using a low pass filter and the error signal is given by

$$\epsilon = 2\sqrt{P_c P_{sb}} \Im\left[r_c r_{sb_+}^* + r_c^* r_{sb_-}\right], \tag{1.34}$$

where r_c is simply the reflection coefficient for the carrier field.

Figure 9 shows the error signal as a function of the cavity detuning for a lossless, symmetric cavity. As the cavity is misaligned from the resonance, we see that the measured error signal is proportional to the phase of the carrier. The slope can then be used to determine on which side of resonance the cavity is on. Therefore, by

[2]Phase modulation is the appropriate choice where control over fast oscillations is needed resulting in a large servo bandwidth [24] [25].
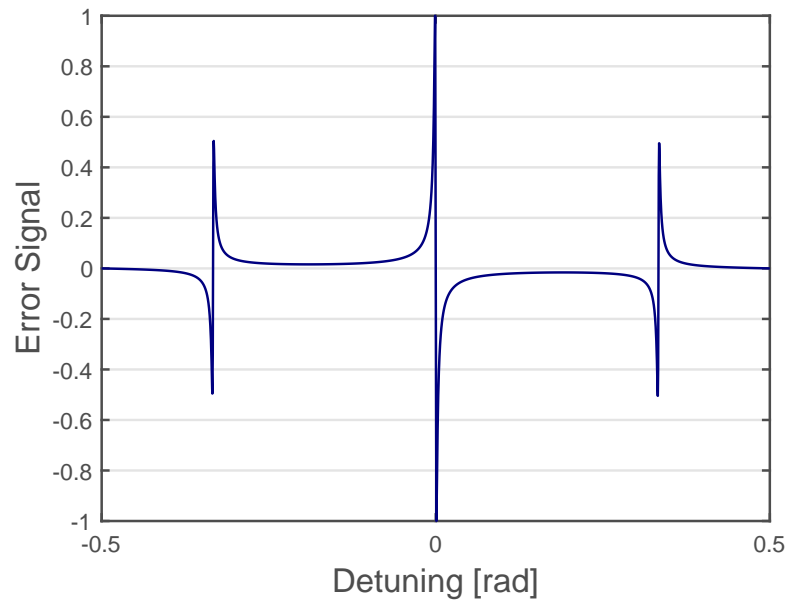
Figure 9: Here the normalized error signal is plotted as a function of the cavity detuning for a modulation frequency of 25MHz. The cavity is modeled as a losses cavity with symmetric mirrors with a finesse of 500. Notice the regime around the resonance is where the error signal is linear, which is ideal for feedback controls.

actuating on the cavity length or laser frequency, it is possible to hold a cavity on resonance[3]. It is important to note that the slope of the carrier and sidebands have opposite signs going through resonance. This implies that it is possible to lock to a given sideband provided a sign flip in the feedback loop electronics (This method is later used in Section 4.3.1 for measuring the phase of a single sideband). Since information about the cavity length is also encoded in the error signal around the resonance condition, it is also possible to extract information about how much the cavity length was perturbed. In the next section I will explore this as a generalized method for PDH used in the aLIGO detectors.

1.5.2 Length sensing and control of a DRFPMI

The individual lengths of optical cavities and the interferometer are given by the graphic in Figure 7. Since sensing and control of the interferometer is done with respect to the differential and common arm motion, then by symmetry we can condense these motions into five degrees of freedom representing the sum and difference of the arm cavity motion. The various degrees of freedom are given in Table 1.

Table 1: Five degrees of longitudinal motion in a DRFPMI.

Degree of Freedom	Parameter	Acronym
Differential Arm Cavity	$L_x - L_y$	DARM
Common Arm Cavity	$L_x + L_y$	CARM
Differential Michelson	$l_x - l_y$	MICH
Power-Recycling Cavity	$l_p - (l_x + l_y)/2$	PRCL
Signal-Recycling Cavity	$l_s - (l_x + l_y)/2$	SRCL

As previously mentioned, sensing these degrees of freedom require a generalized application of PDH, where multiple sidebands are used for sensing in different parts of the interferometer. It turns out that only two modulation frequencies, 9MHz and 45MHz, are required for global sensing of the differential and common motion of the arm cavities in aLIGO[7]. By allowing these sidebands to resonate in the

---

[3]An application note on PDH locking: The cavity must be tuned close to resonance in order for the servo to have sufficient bandwidth to lock the cavity.

interferometer and picking off the signal at specifically selected ports, it is possible to sense the five degrees of freedom associated with the DRFPMI.

The various sensing ports are illustrated in Figure 3. The sensing ports used at the symmetric port are the *reflection port* (REFL) and the *pick-off port* (POP). REFL is used to measure information associated with 9MHz and POP measures information relating to the relative beat between the 9MHz and 45MHz sideband. The Schnupp asymmetry allows for the 45MHz sideband to couple into the dark port (DP)[4].

Length sensing and control is one facet of interferometer control, similarly, LIGO is also concerned with alignment and control of the various optical cavities. Many of the same techniques and sensing ports used for length sensing also apply to alignment sensing, such as the use of RF sidebands to generate error signals for active control. However, the formal name for a sensing system used to achieve alignment control is a wavefront sensor (WFS). This will be discussed in more detail in the next chapter as it applies directly to the work done in this thesis.

1.6   Alignment Sensing and Control (ASC) in LIGO

In the previous section, I discussed how we can maintain control over the length degrees of freedom in LIGO. In this section I will briefly discuss how we maintain control over the angular degrees of freedom and challenges to maintaining control of alignment in LIGO. The angular degrees of freedom in LIGO refer to the "pitch"-rotation about the horizontal axis-and "yaw"-rotation about the vertical axis experienced by the mirrors in the interferometer. In order to achieve optimal strain sensitivity, the ASC must meet the following control requirements[25]:

1. The ASC must maintain angular degrees of freedom in the interferometer to ~ 10nrad in accuracy. This ensures that coupling from intensity noise, beam jitter or oscillator noise is reduced. This also means that angular motion of the optics must be controlled to < 10nrad RMS [27, 28].

2. The beam deviation from the center of the mirrors must be held to within 1 mm [28]. Additionally, the displacement noise introduced by the ASC must be a

---

[4]The Schnupp asymmetry is carefully chosen so that: 1) A sufficient amount of sideband is present at the dark port for sensing. 2) Intensity fluctuations of the laser do not couple into the interferometer readout. The amount of asymmetry in the aLIGO detectors is 8 cm [26]

factor of 10 lower than the interferometer displacement noise in the gravitational wave detection bandwidth.

3. Additionally, angular displacements in the direction of the input laser must be less than 1.5×10^{-14} rad/$\sqrt{\text{Hz}}$ and transverse deviations must be less than 2.8×10^{-10} m/$\sqrt{\text{Hz}}$

The content in this section requires prior knowledge of the Gaussian beams and higher-order modes, as well as coupling of Gaussian beams in optical cavities. The reader is encouraged to take a look at Appendix A, for a review on Gaussian beams, higher-order modes, and coupling into optical cavities. First, I will discuss the framework for alignment theory developed by Anderson and then the practical application of alignment sensing for interferometers.

1.6.1 Misalignment and Mode Mismatch

If we consider a beam incident on a Fabry-Perot cavity, the beam is said to be aligned with the cavity if the optical axis and cavity axis are coincident. Conversely, a displacement or rotation of the cavity mirrors produces a misalignment of the optical axis with the cavity axis. This results in reduction of the resonant beam power in the cavity due only a fraction of the incident beam coupling into the cavity. Theory on the misalignment of optical resonant cavities is explored by Anderson [29] and experimental methods are demonstrated by Morrison [30].

Anderson tells us that the most convenient way to express the spatial modes of a stable resonant cavity is using the HG modes. This ensures minimal losses as the beam resonates in the cavity and that the beam retains its shape as well. Additionally, we can also express our input beam as a linear combination of the HG modes, which is useful for describing when the input beam is either displaced or rotated about the cavity axis (shown in Figure 10 a and b). The lowest order HG modes in one dimension (x dimension) are:
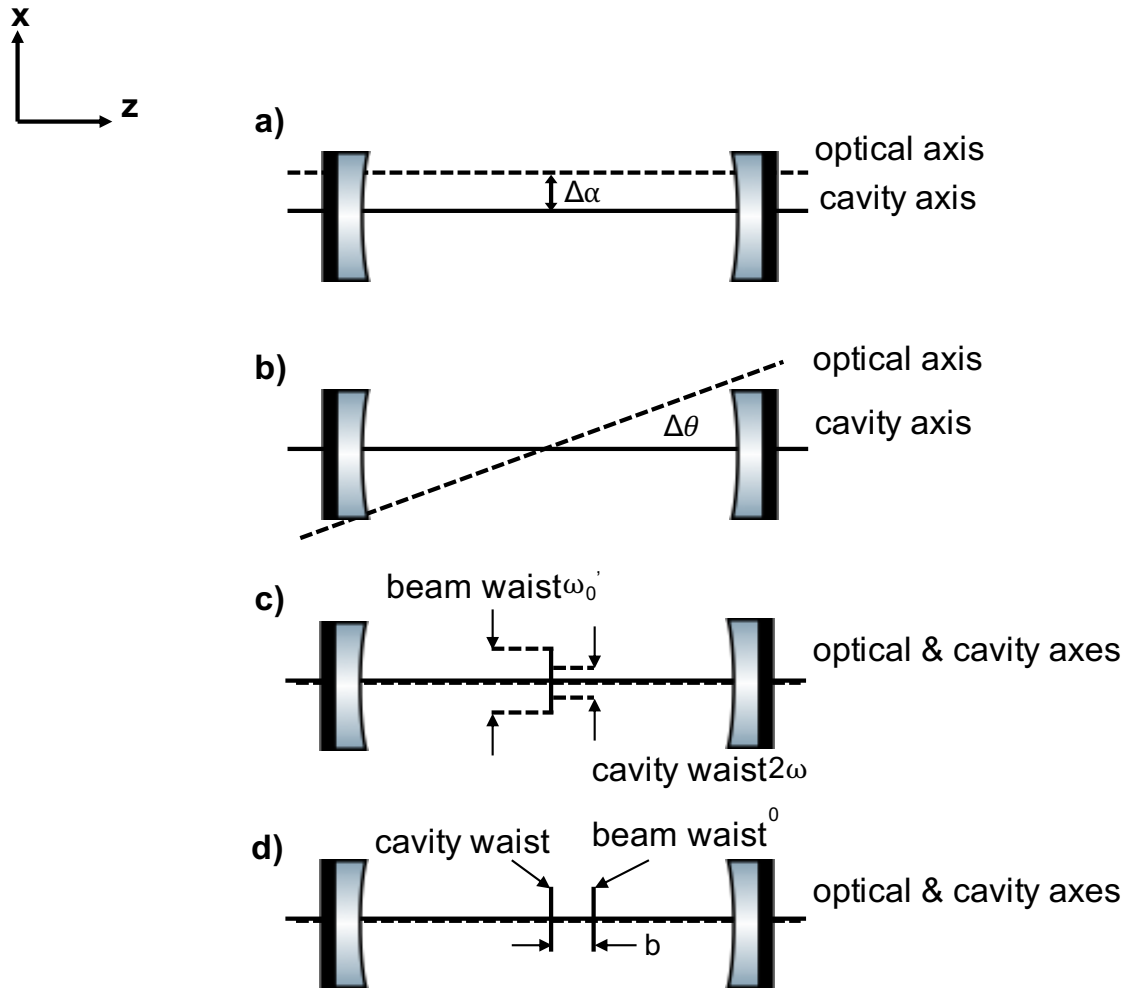
Figure 10: Cases of misalignment of the input beam with respect to the cavity: (a) Transverse displacement of $\Delta\alpha$ along the x direction; (b) Rotation of the input axis by an angle $\Delta\theta$ with respect to the cavity axis; (c) mismatch of the beam waist; (d) displacement of the beam waist with respect to the cavity waist along the direction of propagation

$$U_0(x) = \left(\frac{2}{\pi\omega_0^2}\right)^{1/4} e^{-x^2/\omega_0^2}$$

$$U_1(x) = \left(\frac{2}{\pi\omega_0^2}\right)^{1/4} \frac{2x}{\omega_0} e^{-x^2/\omega_0^2} \tag{1.35}$$

Notice that for simplicity, we consider a point at the waist at which the radius of curvature goes to infinity and the relative phase accumulation of the beam is zero. We expand these lowest order modes to describe the input beam in the case where: 1) it is displaced from the cavity axis and 2) it is rotated about the cavity axis. Mode mismatch is described by the bottom two cases in Figure 10; where 1) the size of the input beam waist does not match the cavity waist and 2) the beam waist is displaced from the cavity waist. The radial symmetry of the cavity leads us to choose the LG modes as our cavity eigenmodes. Similar to before, we can expand the input beam as a linear combination of the LG modes. The lowest order LG modes assuming radial symmetry ($l=0$) are:

$$V_0(r) = \frac{2}{\pi} \frac{1}{\omega_0} e^{-r^2/\omega_0^2}$$

$$V_1(r) = \frac{2}{\pi} \frac{1}{\omega_0} \left(1 - \frac{2r^2}{\omega_0^2}\right) e^{-r^2/\omega_0^2} \tag{1.36}$$

In general, if we want to calculate cavity coupling, we would compute the overlap intergral of the incident beam mode ψ_1 with the cavity mode ψ_2. it is desired that the input beam maximally couples (complete overlap) with the cavity mode. The coupling coefficient is given by [31]:

$$\eta = \frac{|\int \psi_1^* \psi_2 dA|}{\int |\psi_1|^2 \int |\psi_2|^2} \tag{1.37}$$

Transverse displacement of input beam

If we consider a small displacement $\alpha_x/x_0 \ll 1$ of the input beam from the cavity axis this leads to coupling into the first order HG mode. The importance of this result

Degree of Freedom	Parameter	Coupling co-efficient	Mode	Phase(deg)	Frequency
Transverse displace-ment	$\Delta\alpha_\mu$	$\Delta\alpha_\mu/\omega_0$	$U_1(\mu)$	0	ν_0
Tilt	$\Delta\theta_\mu$	$\Delta\theta_\mu\frac{\pi\omega_0}{\lambda}$	$U_1(\mu)$	90	ν_0
Waist size	ω_0'	$\omega_0'/\omega_0 - 1$	$V_1(r)$	0	$2\nu_0$
Waist posi-tion	b	$\frac{\lambda b}{2\pi\omega_0^2}$	$V_1(r)$	90	$2\nu_0$

Table 2: First order cavity misalignment and mode mismatch coupling coefficients as given in [29], where $\mu = $ x or y. $\Delta\alpha_\mu$ is the amount of transverse displacement experienced by the input beam and $\Delta\theta_\mu$ denotes the amount of tilt the input beam experiences relative to the cavity axis. ω_0' denotes the input beam waist and b represents the difference in waist position from the cavity waist. ν_0 is the frequency difference between the TEM$_{00}$ Gaussian mode and higher order modes given by: $\nu_0 = \frac{c}{2d}\frac{1}{\pi}\cos^{-1}\left[\left(1 - \frac{d}{R_1}\right)\left(1 - \frac{d}{R_2}\right)\right]^{1/2}$, where R$_1$ and R$_2$ are the radius of curvatures of the cavity mirrors and d is the distance between the mirrors.

is that transverse displacements of the optical axis with respect to the input beam axis can be described by the first order HG modes. This holds true for translations of the input beam along both x and y directions of the cavity axis since we defined the HG modes to be separable in x and y. The coupling coefficient for a transverse displacement of the optical axis is given in Table 2. As mentioned, this approximation only holds if the displacement is taken to be much smaller than the cavity waist.

Tilt of input beam

Another case of misalignment occurs when the optical axis is rotated in either pitch or yaw by some angle $\Delta\theta_\mu$ with respect to cavity axis (see Figure 10) . Similarly, we see that the misalignment due to tilt produces coupling of the input beam into the first order mode; however, there is a phase shift of 90 degrees at the waist. We can see from Figure 10 that a large rotation of the optical axis in the near field results in a negligible phase shift in the far field. Conversely, a small translation of the optical axis in the near field results in a significant phase difference in the far field.

Waist size shift

Next, we consider a small perturbation to the input beam waist such that $\omega_0' = \omega_0(1 + \epsilon)$. Following the calculation in [29], we see that waist mismatch produces coupling into the lowest order LG_{01}, or "bullseye" mode (for reference a spatial map of this mode is shown in Appendix A). The Laguerre-Gauss basis is used in this case based on the radial symmetry; however, we can also choose to express coupling due to mode mismatch in the cavity basis, or as a sum of the two second order HG modes. In this sense, we can consider mode mismatch to be a second order effect.

Waist position shift

Finally, we consider the case where the beam size is matched but the waist is shifted a distance b along the z direction. Since the radius of curvature is finite at the cavity waist, we need to include this term in the expressions for the eigenmodes of the cavity. The result is that a shift in waist position of the input beam couples into the first order LG mode similar to a shift in waist size; however, the mismatch mode is now in quadrature with the fundamental Gaussian mode.

1.6.2 Wavefront Sensing

The application of wavefront sensing in gravitational wave detectors is for the purpose of detecting higher order mode content coupling into the interferometer via misalignment or mode mismatch. Similar to the PDH locking method discussed in Section 1.5.2, wavefront sensing uses non-resonant sidebands in reflection of a cavity to extract alignment and mismatch signals. The use of non-resonant sidebands also allows length signals to be acquired by the detector. In the case of wavefront sensing, intensity modulation of the optical beat between the carrier and sidebands is used to probe the alignment of the optical cavity. One of the key differences between the Pound-Drever Hall technique and wavefront sensing is, *typically*, a segmented, radio-frequency (RF) photodiode is used to measure the optical beat field of the immediately reflected sidebands and the carrier after a single pass through the cavity. The error signals are then extracted by subtracting the appropriate segments of photodiode corresponding to geometry of the misalignment or mode mismatch.

To illustrate wavefront sensing analytically, consider the modulated one-dimensional carrier field incident on the cavity of the form

$$E_1 = A_1 a_0 U_0, \tag{1.38}$$

where A_1 is the amplitude coefficient and U_0 is the fundamental Gaussian mode. We describe the time dependence of the field using a_0 which contains the phase modulation $m(t)$ and the relative phase difference Φ between the two fundamental mode components of the two beams. We write a_0 as

$$a_0 = e^{j(\omega t + m(t) + \Phi)}, \tag{1.39}$$

where ω is the angular frequency of the incident light. Notice, fundamentally there is no difference between Equations 1.30 and 1.38, with the exception that here we are choosing to express the incident field as an eigenmode of the cavity. When the cavity is on resonance, the sidebands are immediately reflected and the carrier field is transmitted through the cavity. If there is a misalignment or mode mismatch, the part of the field inside the cavity couples into the respective higher order modes. The form of the beam in the presence of misalignment or mode mismatch can be described by

	Transverse displacement	Tilt	Waist size	Waist position
r_0	1	1	1	1
θ_0	0	0	0	0
r_1	$\ll 1$	$\ll 1$	0	0
θ_1	0	$\frac{\pi}{2}$	0	0
r_2	0	0	$\ll 1$	$\ll 1$
θ_2	0	0	0	$\frac{\pi}{2}$

Table 3: Parameters used to characterize tilt, transverse displacement, waist size, and waist position of the higher order misalignment/mismatch modes resonant in the cavity.

$$E_2 = A_2 \left(b_0 U_0 + b_1 U_1 + b_2 U_2 \right), \tag{1.40}$$

where again A_2 represents the amplitude coefficient for the field inside the cavity and U_n describes the modes resonant in the cavity. The complex coefficients, b_n determine the magnitude of the misalignment and/or mismatch present in the cavity. It is given by

$$b_n = r_n e^{i(\theta_n + \omega t + \phi_n(z))} \tag{1.41}$$

Table 3 shows the values of r_n and θ_0 for each of the discussed misalignment/mismatch types, where in all cases $r_0 = 1$. As previously mentioned before, the phase difference present between the fundamental beam and the higher order modes allows one to distinguish each of the cases of misalignment /mode mismatch. Another thing to note is that the beam inside the cavity is not modulated; therefore, the higher order modes associated with misalignment and mode mismatch are unmodulated upon leaking output from the cavity input mirror. The resulting field in reflection of the cavity is given by the sum of the two fields

$$E = E_1 + E_2 = (a_0 A_1 + b_0 A_2)U_0 + b_1 A_2 U_1 + b_2 A_2 U_2, \tag{1.42}$$

and the optical power is given by EE^*. In the case that the m(t) $\ll 1$, evaluating

for the optical power gives us a spatially dependent intensity modulated signal at the modulation frequency of interest. I will show that by integrating this signal over various photodiode geometries, we can extract both length and alignment error signals of interest.

Detecting with a single element photodiode

Since we are only considering optical power incident in the x-direction, we only need to integrate in one-dimension. We can assume that the beam size at the detector is much smaller than the sensor area, which allows us to ignore clipping of the photodiode. Therefore, the modulated intensity can be found by evaluating the integral from $\pm\infty$

$$I = \int_{-\infty}^{\infty} |EE^*| \, dx$$
$$\propto m(t) A_1 A_2 \sin \Phi \tag{1.43}$$

The result of Equation 1.43 shows that the higher order mode contributions from misalignment and mode mismatch produce no net contribution to the measured modulated intensity at our detector. Here, the intensity is proportional to relative phase difference between the two beams. In essence, integrating over the entire area of the sensor allows us to recover information about differential changes in the length of the cavity, which is consistent with the error signal obtained via the traditional PDH method in Section 1.5.2.

Detecting with a split photodiode

Consider now an RF photodiode split along the y-axis. If the incident signal is distributed symmetrically over the detector, then the difference of the integrated intensities can be used to determine the misalignment error signals

$$I \propto \int_0^{\infty} |EE^*| \, dx - \int_{-\infty}^0 |EE^*| \, dx \tag{1.44}$$

Because this is also true for the orthogonal direction, photodiodes used for sensing are typically split into four quadrants. Subtraction of the left and right quadrants allows for sensing of "yaw" and top and bottom for sensing of "pitch" degrees of freedom.

The integration of the quadrants result in a cancellation of the cosine terms; therefore, the intensity is given by

$$I \propto r_1 m(t) A_1 A_2 \sin\left(\theta_1 + \varphi_1(z)\right), \tag{1.45}$$

$$\text{where} \quad \varphi_1 = \arctan\left(\frac{\lambda z}{\pi \omega_0^2}\right)$$

where r_1 and θ_1 are given by the values in Table 3 and φ_1 is the Gouy phase shift of the higher order mode. We see that for errors in tilt ($\theta_1 = \pi/2$), the error signal is proportional to $\cos[\varphi_1(z)]$ and we get a maximum signal at the waist ($z = 0$). Additionally, for misalignments due to translation ($\theta_1 = 0$), the error signal is proportional to $\sin[\varphi_1(z)]$ and we get a maximum signal in the far field where $\varphi_1 \to \pi/2$.

This result is significant because it determines where our photodiode should be placed in order to sense both types of misalignment. In the near-field, or close to the beam waist, a tilt produces an error signal on our phototdiode since the plane wave phase fronts of the two beams produce a differential phase pattern. Conversely, in the far-field the phase fronts of the two beams can be approximated as spherical waves in which both of the radii of curvature become equal to the distance of propagation in the far field. In this case, no interference pattern is produce in the far field and no error signal is detected.

The opposite is true for translations, which produce no signal at the waist, but at a distance far from the waist the photodiode will see a larger intensity contribution along the direction of the shifted beam.

Detecting with an annularly split photodiode

An annularly split, or "bullseye" photodiode is the pragmatic choice in the detection of radially symmetric mismatch modes. Annular photodiodes commonly feature an inner circular region upon which the beam is centered, a null point around the central region, and an outer ring. By subtracting the integrated intensity of the inner region from the outer region, we can obtained the measured error signal.

$$I \propto \int_r^\infty |EE^*| \, r dr - \int_0^r |EE^*| \, r dr \tag{1.46}$$

The cylindrical symmetry means that the integral only needs to be evaluated over the radial coordinate. The result of the integral is similar to the case for the split photodiode, with the exception that only the even terms are left after integration. Therefore, the measured intensity is of the form

$$I \propto r_2 m(t) A_1 A_2 \sin \left(\theta_2 + \varphi_2(z) \right), \qquad (1.47)$$
$$\text{where} \quad \varphi_2 = 2 \arctan \left(\frac{\lambda z}{\pi \omega_0^2} \right).$$

In this case, positioning our photodiode at the waist would optimize sensitivity for measuring waist position mismatch ($\theta_2 = \pi/2$). A simple qualitative explanation for this is because the input beam now has some curvature at the cavity waist due to the offset in waist position. The signal is maximum when $\varphi(z)_2 = 0$. Sensitivity to mismatches in waist size ($\theta_2 = 0$) is maximum when the measuring at $\varphi(z)_2 = \pi/2$, or when $z = \pi \omega_0^2 / \lambda$.

1.6.3 Wavefront sensing of a Dual-Recycled Fabry-Perot Michelson Interferometer

The section aims to highlight the *in-situ* sensing of wavefront sensing aLIGO. For more general discussion on wavefront sensing in aLIGO see [33, 32]. For a dual-recycled interferometer with Fabry-Perot arms the complexity of sensing becomes much more challenging. The four longitudinal degrees of freedom are sensed using the typical Pound-Drever Hall length sensing technique, where RF-sensitive photodiodes are placed at three separate detection ports in the interferometer: the reflection port, antisymmetric port, and the recycling cavity pick-off port. By sampling the intensity modulated signal between carrier and sideband, it is possible to extract an error signal for length, proportional to the relative phase difference of the two reflected beams.

The alignment sensing technique used in aLIGO also has the added benefit that the same sensors can be used for both length and angular sensing. This is because the spatial pattern between the carrier field and sidebands can also carry misalignment information. One key difference between alignment signals and length signals is that the relative Gouy phase shift accumulated by the higher order misalignment modes. By positioning a wavefront sensor at the appropriate location, we can distinguish
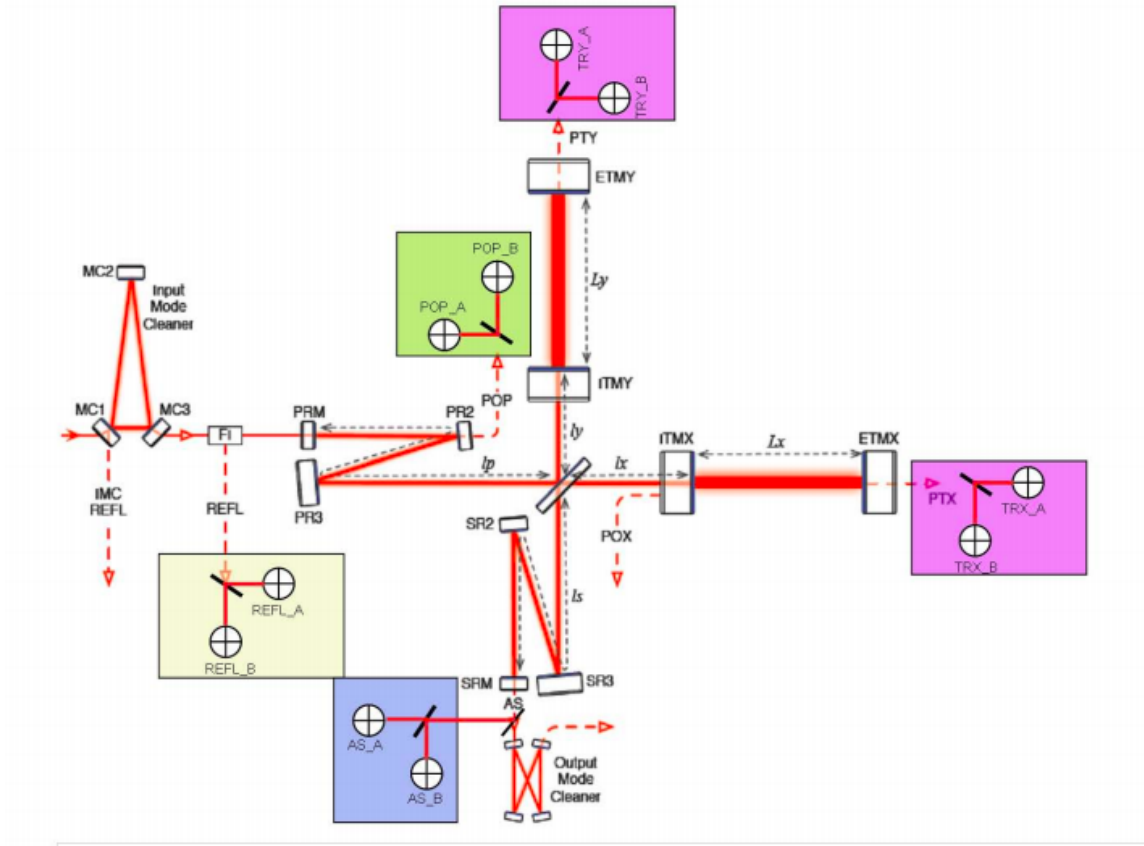
Figure 11: aLIGO optical sensors layout [32].

between a misalignment produced by the input or end mirrors. The presence of a misalignment in either mirror of the cavity will cause either the TEM_{10} or TEM_{01} mode to resonate in the cavity, thus the magnitude of the misalignments can be detected in the beat signal measured at the detector. The interference pattern produced between the TEM_{10} and TEM_{00} will depend on the relative Gouy phase shift between the two modes, which is a function of the longitudinal position of the sensors along the optical axis.

Comparing both DC and RF signals, we can see that DC signals are used to sense the absolute position of the beam on the cavity optics and the RF signals are used to sense the relative positions of the cavity mirrors with respect to each other. Because the aLIGO detector is a coupled network of optical cavities, several degrees of freedom must be sensed in both transverse position and angle. First, the input beam contributes a degree of freedom in both pitch and yaw. Each of the core optics in the interferometer contributes an additional angular degrees of freedom for each optic – this includes the four arm cavity mirrors, beam splitter, and signal and recycling cavity mirrors – for a total of 13 degrees of freedom in total. Because the input beam and recycling mirrors can be described by relative motion of the other cavity optics, we only need to consider 10 independent degrees of freedom. For the aLIGO interferometer, generally there will be at least two wavefront sensors, separated by 90° Gouy phase[5], at each of the output ports (REFL, AS, POP, TRX, TRY as shown in Figure 12). The suffixes _A and _B in Figure 12 denote the two respective sensors. The RF amplitude-modulated signal detected by each wavefront sensor positioned at one of the four detection ports has the general form given by [28]

$$WFS(\eta, \Theta, \Gamma) \propto P_{in}f(\Gamma) \times \sum_{i=1}^{N} A_i\Theta_i \cos(\eta - \eta_i) \cos(\omega_m t - \phi_{Di}), \qquad (1.48)$$

where, P_{in} is the input power, Γ is the modulation index – where $f(\Gamma) \approx \Gamma$ for $\Gamma \ll 1$, η is the additional Gouy phase shift due to the longitudinal position of the WFS, and N are the total number of degrees of freedom. For the ith angular degree of freedom, we also define: A_i the magnitude of the intensity modulated beat between the fundamental and misalignment modes, Θ_i the misalignment angle, η_i the

---

[5]The concept of Gouy phase in a gravitational wave detector is detailed in Appendix B.

relative Gouy phase shift between the fundamental and misalignment modes measured at the detector, and ϕ_{Di} is the phase of the signal at the modulation frequency. By demodulating in the respective quadrature, we are able to spatially resolve any amplitude fluctuations due to misalignment and mode mismatach. The sensitivity to a particular degree of freedom in the interferometer depends highly on the demodulation phase. For maximum sensitivity to differential motion at the AS port, the sensing signal is demodulated in quadrature (Q-phase). The signal demodulation phase is set in quadrature (Q). Since sensing at the AS port is the main focus of this thesis, I will limit the discussion to sensing at the AS port. (For more detailed information on sensing schemes refer to [32].

The total power available for each sensor, considering the nominal operating power of 125 W for aLIGO, is 50 mW. This applies to every sensor before the AS port, where 99% of the power is used to control length and 1% is used for angular sensing leaving only 5 mW of power for 2 sensors or 2.5 mW of incident power [32]. This means that logistically, sensors placed at the AS port must be able to sense modulated signals of much less power in order to measure any significant spatial features of the alignment signals. A discussion on how this was considered in our sensor design is discussed in Chapter 3 and 4.

Overview: Sensing Scheme

In practice, solving the analytical form of Equation 1.48 for each coupled DOF is quite challenging; therefore, in order to measure the response of each sensor to multiple degrees of freedom, numerical models have been developed [32] which extract the response of each sensor to a particular degree of freedom. The response of each sensor to an excitation of a particular degree of freedom can be used to develop a *sensing matrix*. By inverting the sensing matrix, an *input matrix* is generated which reconstructs the error signals for a particular degree of freedom. The error signals for each degree of freedom are then filtered and sent as inputs to the suspension system to control angular position of the optics.

An example of the architecture overview of the sensing scheme in aLIGO is shown in Figure 12. The signal flow is described by the following:
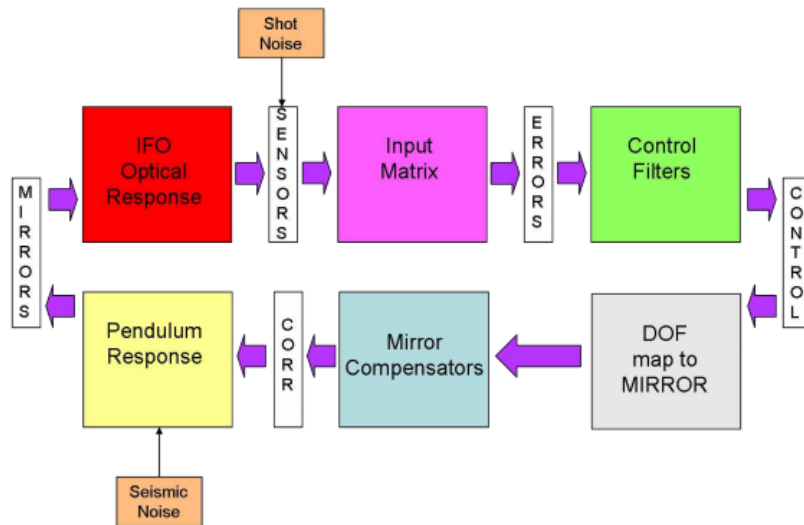
Figure 12: Feedback loop for the ASC in aLIGO [32]. The optical response of the mirrors is measured by the wavefront sensors, which is used to develop an input matrix for feeding back the error signals into the actuators.

IFO optical response Initial response of a particular degree of freedom to an angular motion.

Input matrix The signals on the sensor, with the addition of sensor noise (in the form of shot noise in this example) are combined in an input matrix to define the error signals for a particular degree of freedom.

Control filters and mirror compensators The resulting error signals are filtered and mapped onto the respective mirror degree of freedom.

Pendulum response The compensating force applied to the suspension system to actuate on a particular degree of freedom.

1.7 ASC considerations on sensitivity

Any misalignment or mode-mismatch (due to static or transient sources) between the four main interferometer cavities will cause non-resonant HOMs to couple into the optical cavities. Since HOMs accumulate a different Gouy phase from the fundamental mode, this will result in a degradation of alignment signals and greater loss

of sensitivity. There are a few progenitors of problems that afflict the ASC chain that are worth highlighting for the scope of discussion; however, I refer the reader to [32, 34] for a much more elaborate description of these issues. Here are a few issues that are of particular interest to this thesis because of the potential for a detectable amplitude modulation measurement:

- *Angular noise coupling to DARM*: Residual beam spot motion on the main cavity mirrors produces an effective length change of the main optical cavities. This can be converted into a modulated intensity noise upon reflection from one of the filter cavities.

- *Influence of radiation pressure*: High power operation causes significant radiation pressure torque on the cavity mirrors leading to coupling between pitch and yaw resonances. This is referred to as the *soft* and *hard* mode resonances, which are used as the eigenbasis for alignment schemes in aLIGO [33].

1.8 Conclusion

The aLIGO detectors contain a complex network of coupled optical cavities that require precision control in order to maintain sufficient sensitivity to gravitational wave signals. The Pound-Drever-Hall method for controlling length uses high-frequency modulation/demodulation of the RF beat between carrier and sidebands to ensure control of mirror position. Moreover, the addition of wavefront sensors, positioned at the appropriate Gouy phase separation, measure the two lowest order HOMs (TEM_{10} and TEM_{01}) associated with tilt and displacement of the interferometer mirrors.

This chapter highlighted each of these methods to motivate the need for a dynamic and high resolution wavefront sensor. As I will show in the next chapter, external environmental and physical effects can disturb the alignment and mode matching of the interferometer during operation. Therefore, it is crucial that LIGO wavefront sensors can characterize the spatial information produced by these disturbances in the readout of the interferometer.

Chapter 2

Motivation for Developing a Solid-State Phase Camera

Upgrades to the advanced LIGO detectors include increasing laser power and implementing squeezed states of light. In particular, higher laser power has the benefit of adding increasing sensitivity to gravitational wave signals and reducing detector shot noise by $1/\sqrt{P_{in}}$. With that said, transitioning to higher power has created several problems for current generation gravitational wave detectors during the third observing run.

In particular, high power operation has lead to optical absorption of power in the coatings and substrate of the test masses, worsening the effects of material inhomogeneities and point-defects already present in the test masses. This has led to distortion of the optical wavefront of the beam entering and exiting the main LIGO cavities, which acts as a vehicle for HOM coupling into the control signals and readout of the interferometer (discussed in Section 2.1.1). In Section 2.1.1 I will discuss specifically how the coupling of HOM from wavefront distortion can affect sideband quality, interferometer operation, and readout sensitivity to gravitational wave signals. Section 2.2 addresses other effects of high power on sideband quality as it relates to the input beam and is included for breadth of discussion; although, this is not the main focus of the work in this thesis.

In Section 2.3 I cover some of the existing wavefront sensing technology used in the aLIGO detectors for identifying these wavefront distortions either through direct measurement of the optical wavefront or through measurement of the sideband beat

signal. In Section 2.4 I will discuss image sensors and their potential for imaging spatial mode content in gravitational wave detectors.

2.1 Effects of high power in LIGO detectors

During O3, the aLIGO detectors operated with a nominal operating power of 30-45 W. Considering the power recycling cavity gain $g_{PRC} \approx 45$ and the main arm cavity gain $g_{ARM} \approx 225$, the total circulating arm power in each arm can be determined by

$$P_{ARM} \approx \frac{1}{2} \left(g_{PRC} * g_{ARM} * P_{in} \right), \tag{2.1}$$

which leads to a nominal circulating arm power of ≈ 150 kW. Considering this amount of circulating power, and an effective optical absorption of 0.5 ppm [6] on the highly reflective coatings of the test masses, this results in a loss of 0.075- 0.1 W due to absorbed optical power in the test masses. There are two effects that result from absorbed power in the test masses:

1. **Thermo-refractive effect:** a change in the refractive index of the substrate leading to significant wavefront distortion as the beam propagates through the test mass.

2. **Thermo-elastic effect:** thermal expansion leads to a change in the shape of the test mass. A common result of this effect is a physical deformation ("bump" as shown on the highly-reflective coating of the ITM in Fig. 13) appears on the surface of the test mass. This results in a change in the radius of curvature of the test mass, which affects the Gaussian mode resonant in the cavity.

Both effects scale proportionally to temperature change produced by the heating profile of the beam. Therefore, higher laser power worsens these effects by increasing the amount of thermal energy absorbed in the test masses. Furthermore, absorbed power can be classified as either *uniform* or *non-uniform*:

- *Uniform absorption* results in low-spatial frequency thermal lenses and curvature errors of the test mass substrate. Uniform absorption effects are typically much easier to deal with as they are easily modeled by spherical wavefront errors [36]. In aLIGO, a thermal compensation system (TCS) is used to provide
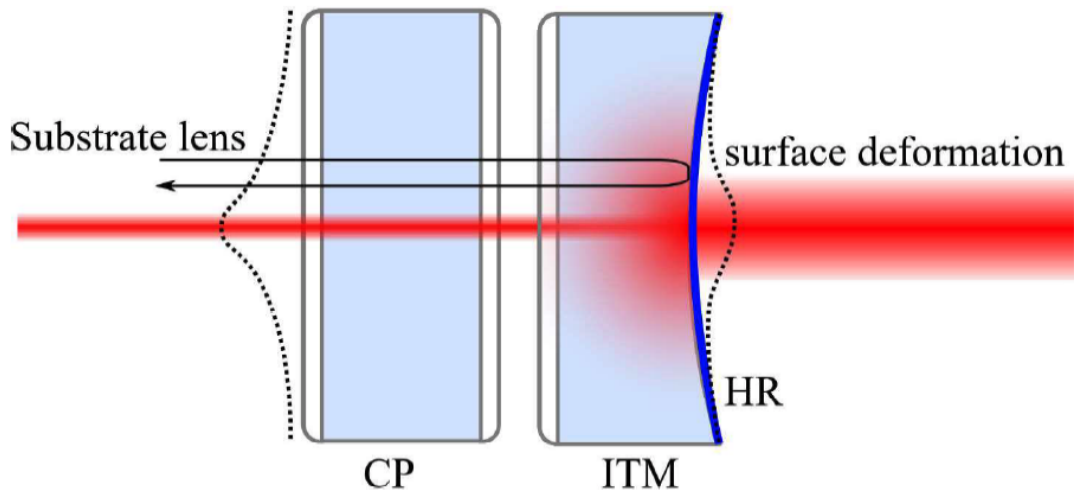
Figure 13: An illustration of the optical wavefront distortion induced as a result of thermal lensing in the substrate and curvature errors of the mirror due to heating of the test mass [35]. The surface deformation appears almost as a "bump" on the mirror surface, which scatters light into HOMs.

correction for low-spatial frequency thermal lensing. This consists of a system of sensors (e.g. Hartmann wavefront sensors (HWS)) and actuators (ring heaters attached to the barrel of the test masses and a CO_2 laser heating compensation plates) to apply correction to the mirrors. Discussion of the TCS is outside the scope of this thesis; however, a good summary of the TCS is provided in [35].

- *Non-uniform absorption* gives rise to high-spatial frequency features on the test masses. A common example of high -spatial frequency features in aLIGO are infamous *point absorbers*. Research into the origin of point absorbers is still an on-going effort; however, the wavefront distortion produced by point absorbers remains a current issue to advanced gravitational wave detectors. Because point absorbers are incredibly small (refer to Fig. 14 for scale) compared to the resolution of current sensors, wavefront distortions induced by the thermal lens of a point absorber becomes difficult to characterize. Additionally, point absorber features scatter light into HOMs beyond the resolution of quadrant or bullseye photodiodes.
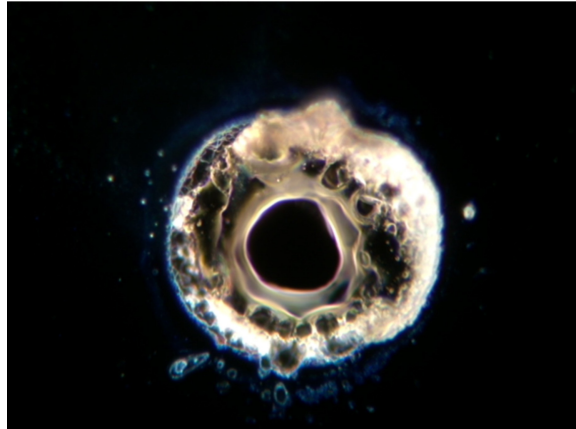
Figure 14: A dark field microscope image of a point absorber as measured on an aLIGO optic [6].

2.1.1   Wavefront distortions

Wavefront distortions are defined as the spatial deviations from the nominal phase front of an electromagnetic field following transmission through or reflection off an optical element. For simplicity, we can consider the case where a beam of wavelength λ with a non-uniform spatial profile $I(x, y)$ is absorbed on the surface of the optic. The resulting phase distortion induced by the uniform heating is then proportional to the amount of optical path length change $\Delta S(x, y)$ induced by the thermal effects mentioned above

$$\Phi(x, y) = \frac{2\pi}{\lambda} \Delta S(x, y) \tag{2.2}$$

For this analysis, we can ignore the individual thermal effects on $\Delta S(x, y)$ and use the fact that the thermo-optic effect is the dominant source of thermal distortion in fused silica [37]. Assuming the light incident on a cavity is purely U_{00} (written in the basis of the cavity), then the distortion will cause some of the light to be scattered into higher order modes. We can model this as the incident field U_{00} subject to the phase distortion $\Phi(x, y)$

$$E = U_{00} e^{i\Phi(x, y)} \tag{2.3}$$

The scattering of the field between modes is then expressed by calculating the overlap

$$M_{mnpq} = \left\langle U_{pq} | e^{i\Phi(x, y)} | U_{mn} \right\rangle \tag{2.4}$$

Let's say we are interested in the coupling as it relates to the fundamental mode since that is what carries the GW signal sideband. Therefore, we can describe the coupling in terms of the fraction of power scattered out of the TEM_{00} mode due to the wavefront distortion by

$$S_{00,00} \equiv 1 - M_{00,00}^2$$
$$= 1 - |\langle U_{00}|e^{i\Phi(x,y)}|U_{00}\rangle|^2 \tag{2.5}$$

In the limit that $\Delta S(x, y) \ll \lambda$, we can expand the exponential and to first order we get

$$S_{00,00} \approx 1 - |\langle U_{00}|1 + i\Phi(x, y)|U_{00}\rangle|^2$$
$$\approx 2 \langle U_{00}|i\Phi(x, y)|U_{00}\rangle \tag{2.6}$$

In this case, we can see that the power scatter due to the phase distortion can be considered as a loss to the total cavity gain by extension of Equation 1.26. As a corollary, increasing optical power will also increase the thermal distortions leading to a decrease of optical arm cavity gain. Now, consider that the sidebands included in our example and assume that the WD distortion produced by thermal effects are purely spherical such that power is predominately scattered in the TEM_{20} mode. In this case, we get [25]

$$S_{20,00} = \left\langle U_{20}|e^{i\frac{2\pi}{\lambda}\Delta S}|U_{00}\right\rangle \tag{2.7}$$
$$= \left\langle U_{20}|e^{i\frac{\pi Dr^2}{\lambda}}|U_{00}\right\rangle$$
$$\approx \left\langle U_{20}|i\frac{\pi D\omega^2}{4\lambda}|U_{20}\right\rangle, \quad \text{for k}\frac{D\omega^2}{2} \ll 1$$
$$= i\frac{\pi D\omega^2}{4\lambda}, \tag{2.8}$$

where ω is the beam waist size and $D \propto P_{abs}/\omega$ is the defocus. The result of Equation 2.7 shows that the amount of power loss due to the TEM_{20} mode is directly proportional to the amount of power absorbed by the optic. There a number of ways in which higher order mode coupling from wavefront distortions can lead to difficulty in controlling the interferometer and a reduction in signal sensitivity.

2.1.2 Impact of wavefront distortions on interferometer performance

Reduced sideband power: Measurement of 9MHz sideband during O3

This section discusses the sideband power level measurements taken by Daniel Sigg following the replacement of ITM X and Y at LHO [38]. A persistent issue during the third observing run was the "missing" 9 MHz sideband power when measuring in reflection of the arm cavities. After the ITMs were replaced, the sideband power levels were re-measured. Table 4 summarizes these measurements as a ratio of the normalized power before and after replacing the ITMs.

Port	DC	45 MHz	9 MHz	Carrier
Input power	1	1	0.98	1
POP_A_NSUM	1.21	1.07	1.69	1.20
POP_B_NSUM	1.20	0.85	1.71	1.19
OMC_A_NSUM	1.04	1.19	0.24	0.79
OMC_B_NSUM	1.10	1.22	0.24	0.81
AS_C_NSUM	1.00	1.22	0.29	0.68

Table 4: The normalized power ratio of old vs. new sideband and carrier power after replacing ITMs.

Some interesting results of this measurement, which identified the contaminated ITMs as the main culprit behind the reduced 9 MHz sideband power buildup are:

- The 9 MHz power recycling gain *increased by roughly a factor of 1.7*

- Accounting for the input efficiency and losses along the optical path of PSL to REFL, the percentage of power in the carrier, 45 MHz and 9 MHz was estimated to be roughly 9%, 25%, and 65%.

- The 9 MHz power at the AS port was *reduced by a factor of ∼4* in comparison, thus reducing the amount of "junk" light from the 9 MHz at the AS port.

- Out of the 320 mW of power measured at the AS port, 269 mW was measured in the 45 MHz sideband, 32-46 mW in the carrier and 4-5 mW in the 9 MHz sideband. In the carrier, 23.3 mW of power was measured in the TEM_{00} and 9

- 23 mW was measured in higher order modes. In comparison, before the ITMs were replaced, the higher order mode power and fundamental mode power were measured at roughly equal levels.

Maintaining adequate sideband power in the interferometer is important for generating reliable control signals and for the readout of gravitational wave signals. For most of O3, the LHO had to deal with sub-par 9 MHz sideband power buildup because the spatial map of the 9 MHz sideband could not be directly imaged. Therefore, these measurements stress the need for a phase camera as a diagnostic tool.

Reduced optical gain in the power recycling cavity

Recall from Equation 1.26 that the maximum gain of the PRC scales inversely with the amount of optical loss in the cavity. When power is scattered out of the fundamental mode of the interferometer after reflection from a distorted test mass, the power in the fundamental mode is reduced leading to optical loss in the cavity.

This effect was observed during O3 when the incident optical power on the PRC was increased from 25 W to ~ 40 W and the corresponding power increase did not increase the power buildup in the PRC. Figure 15 shows the relationship between the input power and the measured power in the recycling cavity. The measured power buildup is given for two separate beam spot locations on the ETMs at LLO. The difference between the measurements at separate locations indicates that the reduction in optical gain could be mitigated by simply changing the location of the beam spot.

Increased jitter noise coupling

Input beam jitter coupling has been an important technical noise source for LHO during the second and third observing runs of aLIGO. Beam jitter is the result of fluctuations in the beam propagation direction or beam position. This often leads to the excitation of first-order HG-modes that co-propagate with the fundamental TEM_{00}. Input beam jitter is worsened by cavity mismatch, which results in amplitude modulation of the beam jitter modes coupling back into the main interferometer detection port.
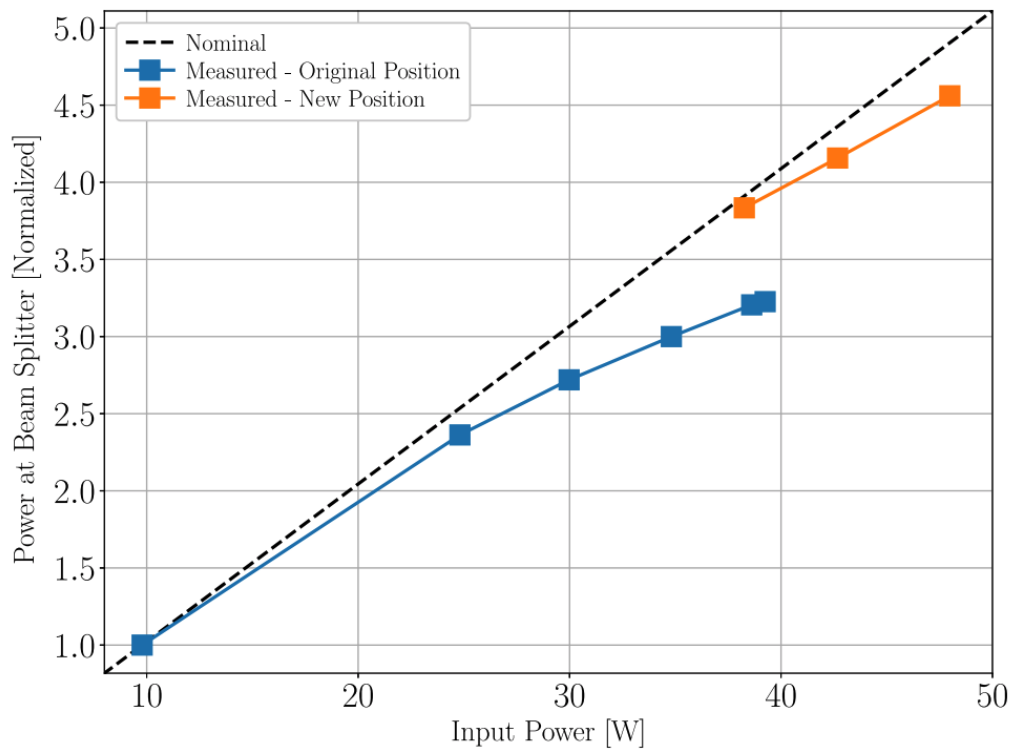
Figure 15: Power incident on the beam splitter as a function of the interferometer input power at LIGO Livingston Observatory (LLO) [2]. The dashed line is the expected power buildup assuming no losses. Power is measured at POP and taken for two separate locations on the end test masses.

During O2 at LHO, it was observed that arm cavity mismatch contributed a significant amount of beam jitter noise coupling into the differential arm (DARM). Efforts to reduce beam jitter included reducing motion of optics on the PSL table and periscope in addition to subtraction of jitter noise from the readout. However, it was found that replacing input X-arm test mass, which had a point absorber in the coating, reduced the amount of coupled jitter noise from the pre-stabilized laser to DARM [40]. Following O3, the ITMY test mass was also replaced, which also resulted in an additional reduction of input beam jitter coupling due to the increased arm symmetry and common mode rejection of jitter modes. The overall reduction in beam jitter was measured to be close to a factor of 10 (see Fig. 16). Additionally, the same factor of improvement in beam jitter was also observed in DARM, in particular,
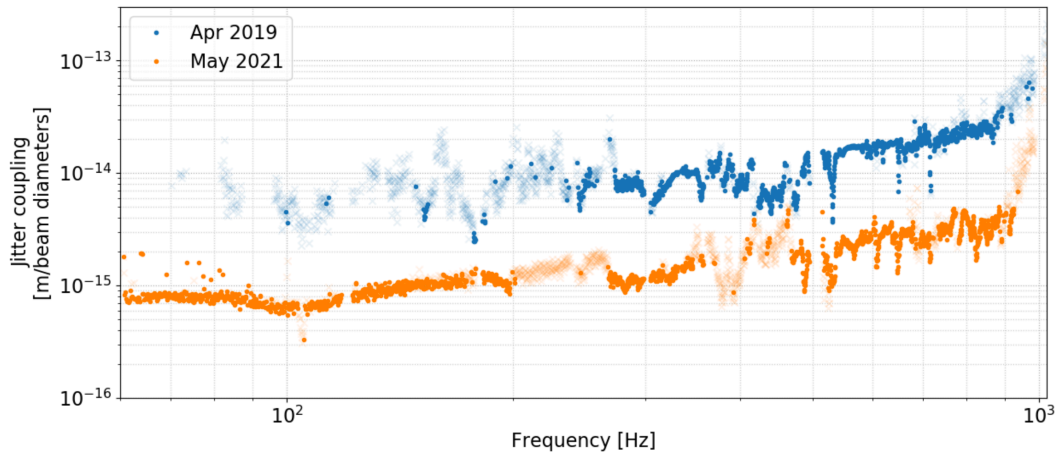
Figure 16: A comparison of beam jitter during pre-O2 (Apr 2019) and post-O3 (May 2021) after removal of the point absorber-affected input test masses [39].

at around 500 Hz where a small peak due to beam jitter coupling had been present throughout O3.

Increases in noise at the anti-symmetric port

There are two mechanism by which noise can couple into the anti-symmetric port due to wavefront distortions:

- *Common-mode WD* are distortions that are symmetric to the front surface of the beam splitter, which reduce the mode matching in the power recycling cavity. An example in LIGO would be a common-mode change in the radii of curvature of the ETMs. The change in curvature of the ETMs would not alter the input mode into the PRC; however, the mode size of the beam re-entering the cavity

would be altered. This leads to a mode mismatch of the PRC, reducing the power gain at the beam splitter. Consequently, the shot noise increases by the square of the calculated overlap between the input mode and fundamental mode (Equation 2.4).

- *Differential-mode WD* are distortions that are anti-symmetric to the front surface of the beam splitter, which increase the amount of "junk" light at the anti-symmetric port. Generally, an imbalance in the reflectivity between the ITMs will cause the light to interfere constructively at the anti-symmetric port. This "junk" light does not contain any information about the phase changes produced by a GW signal. An additional side effect is that intrinsically this light will have some shot noise and potentially some intensity noise.

Loss in achievable squeezing

Planned upgrades for advanced gravitational wave detectors include the use of squeezed vacuum states of light for improving vacuum fluctuations at the detector output [41, 42]. This is done by injecting squeezed vacuum states of light into the AS port, which have the effect of reducing the uncertainty in the quadrature phase of the field that we are interested in and increasing uncertainty in the in-phase signal. Implementation of squeezed light states are done in a effort to improve shot-noise limited sensitivity at high frequencies [43]. The main challenge with squeezing is mitigating the optical losses in the interferometer. Optical losses occur when power is coupled out of the fundamental mode due to either scattering, absorption, or wavefront distortion during transmission or reflection from an optical interface.

To better understand how optical losses impact squeezed light states, consider that any optical loss can be modeled by a beamsplitter (see Fig. 17) with a power reflectivity of $\eta_{loss} = 1 - L$, where L is the amount of optical loss. Figure 17 shows that in the presence of optical losses, the unsqueezed vacuum field δE_{vac} enters the beamsplitter and combines with the transmitted field δE_{in}. The fluctuations in the output field is then given by the sum of the fluctuations in the input field [44]

$$\delta E_{out} = \sqrt{\eta_{loss}}\delta E_{in} + i\sqrt{1 - \eta_{loss}}\delta E_{vac} \tag{2.9}$$

Calculating the variance of the fluctuations,
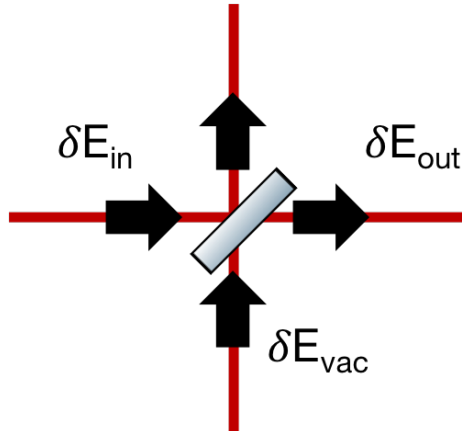
Figure 17: Beamsplitter model of optical loss.

$$\mathbf{V_{out}} = \eta_{loss}\mathbf{V_{in}} + (1 - \eta_{loss})\,\mathbf{V_{vac}} \qquad (2.10)$$

It follows from Equation 2.10, that an increase in optical losses directly correlates with an increase in the amplitude of the vacuum fluctuations. Generally, this model can be considered for several sources of optical loss, in which the total loss throughout the interferometer is given by the product of the individual losses. When applying this to the case of the entire interferometer, as is done in McCuller et. al (2021), the principle mechanism of optical loss at high frequencies is revealed to be due to the imperfections in spatial overlap between the input beam mode and the resonant cavity mode (i.e. mode mismatch) [45].

The current target level for achievable squeezing in the aLIGO detectors in 3dB of squeezing; however, the highest level of measured squeezing was 2.2 and 3.1 dB for the LIGO Hanford (LHO) and Livingston (LLO) observatories, respectively [46]. The discrepancy between squeezing levels can be attributed to the amount of optical loss due to mode matching between the in-vacuum optical parametric oscillator (VOPO) – squeezing source – and the output mode cleaner (OMC), which is around 30% [47]. Therefore, improving squeezing levels requires robust sensing elements that prioritize characterization of transverse-modes that propagate through the interferometer.

2.2 Other effects of high power: sideband imbalances from residual amplitude modulation of electro-optic modulator

To extract error signals we use a technique where phase modulation is applied to the incident carrier field which generates sidebands that are offset in frequency from the carrier. Upon reflection from an optical cavity, the sideband and carrier fields interfere and produce the beat signal of interest at the modulation frequency. The measured demodulated signal is then used determine if the cavity shifts off-resonance due to changes in length. As explained previously in Section 1.5.1, this is colloquially known as the Pound-Drever-Hall technique. Based on this, it is easy to see how alignment of the interferometer is highly-dependent on the quality of the sidebands and the phase modulation used to generate the sidebands. When an electro-optic modulator (EOM) generates sidebands on the incident electric field, the amount of phase shift is given by the familiar expression [48]

$$\Delta\phi = \frac{\pi n_x^3 r V}{\lambda}, \tag{2.11}$$

where n_x, r, V, and λ are the unperturbed refractive index in the x direction, an electro-optic coefficient, the applied voltage, and the laser wavelength, respectively. During the phase modulation it has also been shown [49, 50] that a residual amplitude modulation (RAM) of the field can appear as a result of mismatch between the incident field polarization axis and crystal axis. Additionally, ref. [51] has also shown that optical cavities formed within the crystal can also contributed to undesired amplitude modulation. Typically, these issues are a result of temperature drifts, which result in thermal expansion of the crystal. To see how a residual amplitude modulation would impose imbalances in the sidebands consider that the field incident on our cavity experiences both amplitude and phase modulation due to the RAM of the EOM

$$E = E_c \left[1 + \Gamma_a \sin\left(\omega_m t + \Delta\phi\right)\right] e^{i\Gamma_p \sin\omega_m t}, \tag{2.12}$$

where $E_c = E_{in} e^{i\omega_c t}$ is the carrier field, ω_m is the modulation frequency, Γ_a and Γ_p are the modulation depths of the RAM and phase modulation, respectively. Here,

$\Delta\phi$ represents the relative phase difference between the RAM and phase modulation. Solving for the case of a single sideband for $\Gamma_p \ll 1$

$$E = E_c \left[1 + \Gamma_a \left(\cos\phi \sin\omega_m t + \sin\phi \cos\omega_m t\right)\right]\left[1 + \frac{\Gamma_p}{2}e^{i\omega_m t}\right] \qquad (2.13)$$

$$E = E_c \left[1 + \frac{\Gamma_a}{2}\cos\phi e^{i\omega_m t} + \frac{\Gamma_a}{2}\sin\phi e^{i\omega_m t} + \frac{\Gamma_p}{2}e^{i\omega_m t}\right]$$

I have assumed here that the beat frequencies at $2\omega_m$ are filtered by the bandwidth of the detector and can therefore be ignored from this analysis. The result of the field in Equation 2.13 implies that an additional phase offset is introduced as a result of the amplitude modulation.

2.3   Overview of Wavefront Sensing Technology in LIGO

In this section, I present a literature review of current wavefront sensing technology used in LIGO.

2.3.1   Hartmann Wavefront Sensors

Parameter	Value
CCD size	12.3 mm × 12.3 mm
Spatial resolution	7 mm × 7 mm ITM
Wavefront sensitivity	1.3 nm RMS
Frame rate	1 Hz

Table 5: Specifications for the Hartmann wavefront sensor used in aLIGO.

Hartmann Wavefront Sensors (HWS) provide a direct measurement of the WD by measuring the gradient change of a wavefront relative to a reference state. The HWS is composed of an auxiliary probe beam, typically a super-luminescent diode (SLED), and charge-coupled device (CCD) with a Hartmann plate. Direct measurement is achieved by measuring the wavefront distortions accumulated by the injected probe beam after reflection or transmission through the optic of interest. To see how this works, consider the case where the probe beam returns after experiencing a WD

Figure 18: An illustration of the usage of the Hartmann wavefront sensor. The probe beam is magnified onto the imaging plane P of the optic by a telescope and the wavefront (dashed line) experiences the distortion (solid line) induced by the deformities in the test mass substrate. The return probe beam is refocused onto the Hartmann sensor and measured it the conjugate image plane *P'*, which ensures one-to-one mapping of the induced WD.

through a thermal lens in the optic. Here we find it is useful to describe each point on the undistorted wavefront as an individual ray, where the undistorted state is considered the reference. Therefore, any distortions to the optical wavefront will produce a displacement of each ray from the reference position, thus creating a local gradient of the incident wavefront. By integrating over the gradients a spatial map of the wavefront distortion incident on the HWS can be generated.

In the aLIGO, there are four HWS positioned at each of the test masses to monitor the amount of wavefront distortion induced by thermal lensing. The incident probe beam is first magnified by a telescope in order to sample a 200 mm diameter space on the HR surfaces of the test masses. Upon return to the CCD, the distorted probe beam passes through the Hartmann plate and the deviations in the wavefront are measured. A schematic diagram of the usage of the HWS is provided in Figure 18. For reference, some relevant specifications of the Hartmann wavefront sensor are also shown in Table 5.

One significant limitation of the Hartmann sensors is the inability to resolve features smaller than the spatial resolution of the sensor ($\sim$ 7 mm in both of the
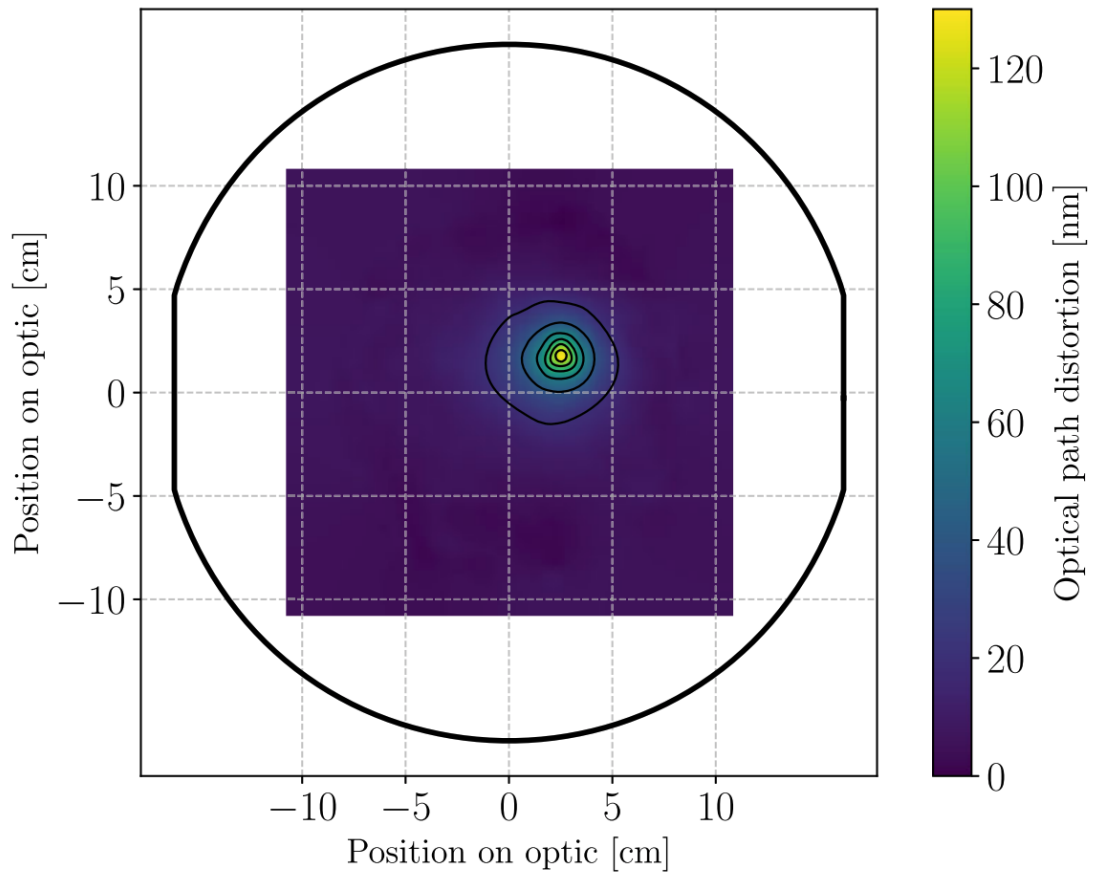
Figure 19: Hartmann sensor image of the point absorber shown in Fig. 14 [2]. The main interferometer beam spot on the optic is indicated by the shaded part of the grid and the illuminated defect is given by the step contour region. The contour spacing is 20 nm and the largest contour ring represents a distortion of 20 nm. The Hartmann wavefront sensors has an uncertainty of about ± 1 cm in the location of the origin of the coordinate system.

	QPD Combination	BPD Combination
Mode Mismatch	+ A − B + C − D	+ E − F − G − H
Pitch	+ A − C	+ F −½G −½H
Yaw	+ B − D	− G + H
Sum	+ A + B + C + D	+ E + F + G + H
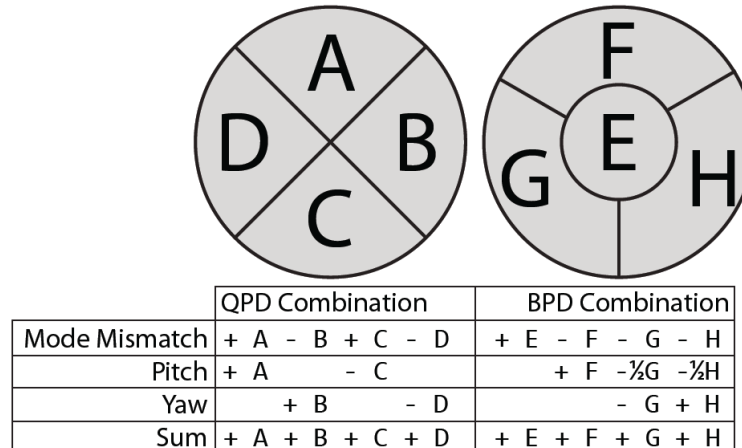
Figure 20: An illustration of the sensor layout for quadrant and bullseye photodiodes [52]. Pitch, yaw, mode mismatch and sum signals can be extracted by taking the appropriate combination of sensor elements.

transverse directions). As previously mentioned, most point absorber features are in the sub-millimeter regime, which induce WD much smaller than the resolution of the Hartmann sensors. An example of an optical path distortion measurement (includes thermo-elastic and thermo-refractive deformations) using the Hartmann sensor is shown in the contour map of Figure 19.

Hartmann sensors offer the advantage of independent monitoring of the spatial profile of each of the test masses. This decouples the resonant effects of other cavities in the interferometer. Using this we can reliably provide compensation to a single test mass via the TCS. Consequently, this means that changes in interferometer beam mode cannot be sampled with the HWS, which is important for understanding the quality of mode matching and alignment between cavities. In Section 2.3.2, I will present sensors complementary to the HWS, that are designed to directly monitor the beam mode propagating throughout the different cavity subsystems.

2.3.2 Resonant quadrant and bullseye photodiodes

Under ideal operating conditions, the fundamental U_{00} mode is the dominate mode propagating throughout the interferometer. Recall from Section 1.6, that in the event that of a misaligned or mismatched optical cavity, the eigenmode of the cavity allows

power to couple into higher order modes, $U_{01,10}$ and $U_{02} + U_{20}$, respectively. The signal measured at a single element photodiode would then be the superposed fields of the fundamental mode and misalignment/mode mismatch mode. Section 1.6.2, reveals what would happen if this interference term were then integrated over the entire plane. We would see a complete cancellation. Therefore, we use photodiodes with split geometries (i.e. bullseye and quadrant photodiodes) and take the difference of the segments to extract the relevant interference terms. Figure 20 depicts the two common resonant photodiode geometries used in LIGO.

The Cartesian symmetry of the quadrant detector makes it ideal for sensing the alignment modes $U_{01,10}$. The distinction between a quadrant photodetector (QPD) and quadrant wavefront sensors (WFS) is that quadrant wavefront sensors typically feature a RF resonant circuit, which is tuned to operate at the frequencies of sidebands in LIGO – 9 and 45 MHz. One key drawback to note is that each resonant circuit can only operate at a signal resonance frequency, this requires the installation of multiple resonant photodetectors to sense the sidebands and multiples of sidebands propagating throughout the interferometer. Additionally, two quadrant wavefront sensors must be positioned at the appropriate Gouy phase apart (90°) to be able to sense both position and displacement degrees of freedom.

Based on the same argument of symmetry discussed above, we know that the beat signal produced by the radially symmetric "donut" mode (LG_{01}) will completely cancel when integrated over the segments of a quadrant photodiode. In this case, the best way to recover the mismatch error signal is to use a bullseye photodetector (BPD) and subtract the inner radius from the outer radius (depicted in Figure 20). In theory, this sounds simple enough; however, in practice a few calibration steps are required to ensure sensitivity to the donut mode symmetry:

Beam size requirement on the BPD must be $\omega_0 = 2\sqrt{r_0}$ where r_0 is the radius of the LG_{01}. This is done so that the null point of the LG_{01} mode matches boundaries of the inner and outer radius of the BPD. The BPDs are built such that the null point is at 1 mm from the center, which can be used to determine the appropriate power ratio required between between the inner and outer segments [53].
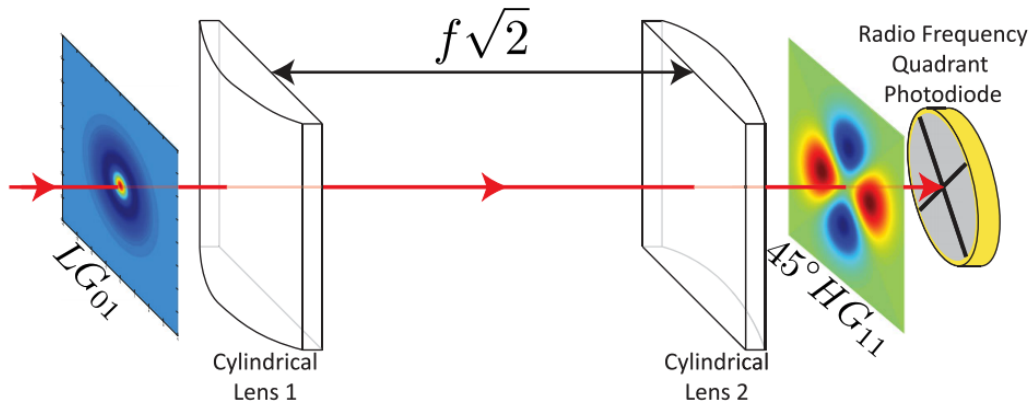
Figure 21: Illustration of an LG_{10} mode through a $\pi/2$ mode converter [52]. Mode mismatch in a well-aligned Fabry-Perot cavity will produce coupling into the LG_{01} mode. The LG_{01} mode is rotated to a $45°HG_{11}$ mode by a $\pi/2$ mode converter. The mode converter consists of two cylndrical lenses placed f$\sqrt{2}$ apart in distance, where f is the focal length [52].

Gouy phase separation between BPDs must be 45° or 135° to sense the orthogonal mode matching degrees of freedom – waist size and position.

Gouy phase mode converter with resonant quadrant photodiode

It was recently discovered by Magaña et. al. that the use of a mode converter can be applied to heterodyne beat sensing with a quadrant photodiode [52]. This removes the need for using resonant bullseye photodiodes, which have proved difficult to manufacture and calibrate *in-situ* during measurements. The scheme works by placing a pair of cylindrical lenses in front of a resonant quadrant photodiode, which converts the axially symmetric fields of the mode mismatch mode to allowing for sensing on the geometry of the quadrant photodiode. The lenses work by propagating the phase of one axis by $\pi/2$ relative to the other axis, which breaks the symmetry between the axially symmetric donut mode (shown on the left in Figure 21. In addition, because the mode converter does not change mode order, it preserves the angular and modal mismatch error signals completely. Thus, it has been shown that alignment error signals can still be recovered using this method [52].

Some drawbacks of using a mode converter are the additional cylindrical lenses that must be added in front of the wavefront sensors to achieve mode conversion. The addition of these lenses sets specific constraints on the beam waist size and on the alignment of the beam through the cylindrical lens axis, which if not configured properly, can result in a distortion of the measured error signal. Additionally, mode converters used with resonant quadrant photodiodes have the same functional limitations of the resonant quadrant photodiodes (i.e. "pixel" resolution and sensing noise added by external electronics).

2.3.3   Scanning-based phase cameras

The first generation of phase cameras introduced in LIGO were based on a scanning technique where the test beam; after propagating through the interferometer, is superposed with a separate reference beam [54]. In LIGO, typically the test beam would be the main interferometer beam, which picks up the higher order mode distortion from a mismatched cavity; however, for the initial tests of the scanning phase camera, a high-finesse cavity was tuned to allow higher order mismatch modes to transmit on the test laser (see Figure 22). A separate reference laser, offset in frequency from the carrier, is used to downstream to generate the beat note between the two beams. Two galvanometers are then used to spirally-scan the two beams over the surface of a photodetector. A pin-hole is used to ensure that the beams are only combined only for a single pixel. Each point is then used to spatially map the measured beat signal.

A few limitations to this method are:

- Discontinuities in the scanning pattern resulted in difficulties interpreting phase information (see Figure 23. This is observed by the phase map produced in

- Scan frequencies are limited to only about 5 Hz, which is a physical limit of the galvanometer inertia. For this reason, spiral patterns are used as this is the fastest scanning pattern *in situ*

- Sample resolution is limited to only about 1000 points per scan
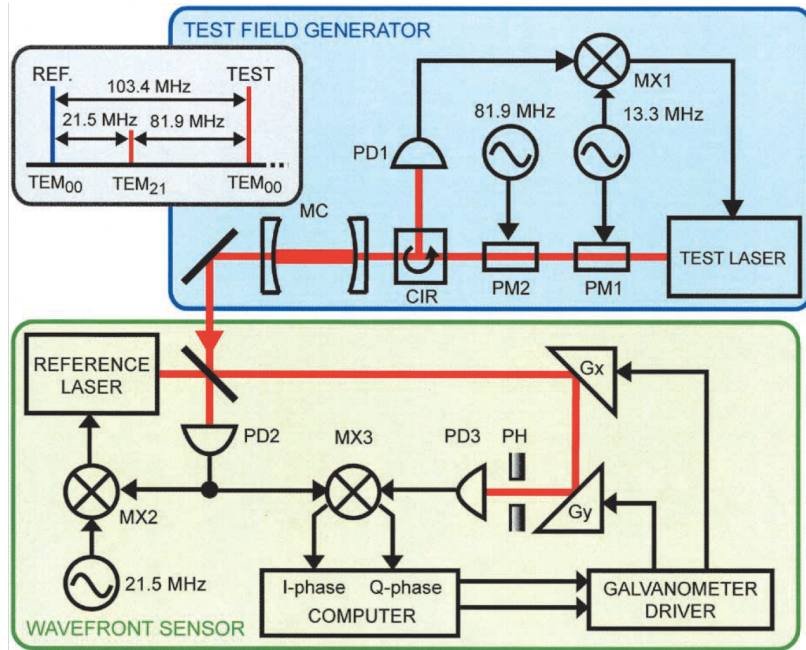
Figure 22: A schematic diagram of a scanning phase camera [54].
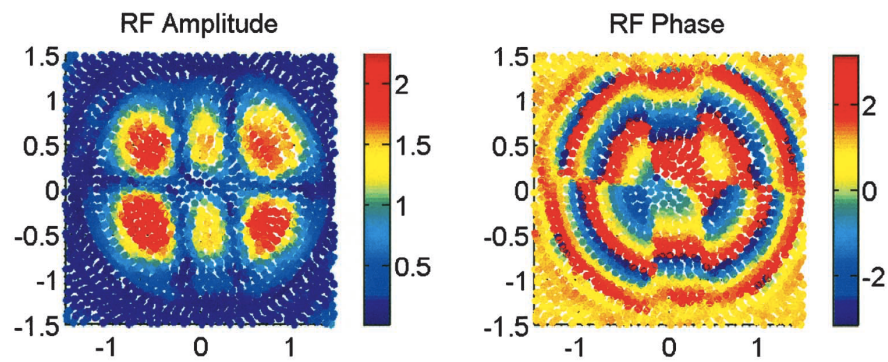
Figure 23: Beat map of TEM$_{21}$ on a scanning phase camera [54].

Figure 24: Camera image at AS AIR when LHO was locked in MICH DARK [55].

2.4   Image Sensors

In LIGO, image sensors are widely used for monitoring beam quality and position at each of the detector ports. Specifically, one use case is the imaging of the junk light that appears at the AS port due to WDs. Some exotic mode structures can appear at the anti-symmetric port due to this unwanted light. For example, a 9th-order transverse mode was observed on the OMC transmission at LHO during O2 [2].

Another example of this can be seen by the AS AIR image shown in Figure 24. In this measurement [55], the camera image were used to estimate the percentage of power coupled into mismatch and alignment modes.

2.5   Conclusion

Changes in the mode size and radii of curvature of the main arm cavities change the cavity mode and affect mode-matching. High power-induced thermal effects have been the main mechanism for wavefront distortion in aLIGO, which cause optical loss in the cavities by scattering power into higher order modes. Unless properly identified and mitigated, optical scattering into higher order modes will cause: loss of optical gain in the main arm cavities, reduction of mode matching in the main optical and auxiliary cavities, losses of sideband power, increased jitter noise, and degradation of squeezed light states. Therefore, wavefront diagnostic tools are imperative for ensuring that the LIGO detectors operate with increased duty cycle and at design

sensitivity.

This chapter reviewed several diagnostic sensors used for characterizing wavefront distortions both directly and indirectly. The Hartmann wavefront sensor, has demonstrated proficiency in mapping the spatial distortions in the optical wavefront produced by point absorbers on the test masses; however, it is limited to only a single frequency of the carrier and cannot describe how the sidebands are affected by thermal distortions. For this reason, bullseye and quadrant photodetectors have been implemented in a heterodyne scheme to measure the beat signal of anti-resonant sideband and higher order mode produced by the phase distortion. The main drawbacks of using resonant photodetectors are limited spatial resolution and cost to manufacture different detector geometries.

Image sensors have demonstrated the ability of generating high resolution images of beam intensity profiles at fast frame rates. Therefore, a new generation of wavefront sensors (*phase cameras*) based on CCD and CMOS cameras have been in recent development for use as diagnostic tools in aLIGO. The promise of these sensors is to offer high resolution spatial maps of the individual cavity modes. This will ultimately lead to a significant improvement of detector diagnostics.

Chapter 4 will present the work I have done in developing a phase camera based on a 3D time-of-flight CMOS camera wave.

Chapter 3

Time-of-Flight Cameras: Hardware Heritage

The intended use for most time-of-flight cameras involves the direct measurement of light travel time. However, in most cases of commercial time-of-flight cameras, the direct measurement of light travel time from a round trip bounce of an emitted light source is actually impractical. This is because classical electronics are far too slow to sample differences in the light travel time that are on the order of picoseconds. Instead, the relative phase difference is measured between an emitted and reflected intensity modulated light source. This development in 3D-ToF sensing provided a practical and robust solution in industrial applications involving environment awareness for machines. The implications of this sensing scheme are far-reaching and in this section I will motivate how this technology can be used to make phase-sensitive measurements in modern-day gravitational wave detectors.

3.1   Hardware Origins: The two-tap Lock-in Pixel

ToF cameras equipped with *in-pixel* (de)modulation, such as the OPT8241-CDK-EVM, consist of an array of pixels with control electronics capable of computational and signal processing capabilities. The demodulation pixels are based on the photonic mixer device technology, which was pioneered by Schwarte [4]. The architecture of a pixel based on the photonic mixer device (PMD), consists of one or more integration wells, known as *taps*. A schematic of a commonly-used two-tap pixel is shown in

Figure 25.

Typically, a modulation block internal to the time-of-flight camera is responsible for generating intensity modulated light and synchronously driving the charge separation within the pixels. After the intensity modulated light completes one round trip from the scene and back to the camera, it is absorbed in the photosensitive area, or *photo gate (PG)*, where photons are converted into charge carriers via the photoelectric effect. Electrodes in the substrate area below the oxide layer are driven by the reference oscillator and used to move charge carriers into the storage wells at Node A and B. The control electronics dictate which well is active during an integration cycle. As a result, the total integrated signal within the respective well is equal to the scalar product of reflected light signal and the reference modulation signal. During the readout process, the integrated signals between the two nodes are subtracted. For a modulating signal with a duty cycle of 50%, this ensures suppression of any DC signal offset from initial resetting of the capacitive nodes in the measured RF readout. This process is formally known as correlated balanced sampling (CBS) (See Section 3.3).

To see this consider the unmodulated, or *ambient*, signal in the presence of a modulated driving field in the demodulation pixel. For a reference signal with a 50% duty cycle, the DC signal will be present in Node A for half the integration cycle and Node B for the other half. When taking the difference, these values cancel. In the case of the modulated signal, the difference between the two nodes will be proportional to the amount of phase difference measured between the modulated signal and the reference signal.

In the next section we will explore the process of demodulation in a solid-state ToF camera and how phase and amplitude are retrieved from the optical signal.

3.2 Demodulation Theory: Measuring amplitude, phase and offset

Demodulation in a CW-ToF camera is based on a phase detection technique where the incident intensity-modulated light is synchronously sampled at discrete phase intervals φ_i, $i \in [1, N]$ in the camera. When the modulated light arrives at the ToF sensor it contains some unknown amount of phase delay ϕ. Therefore, in order to
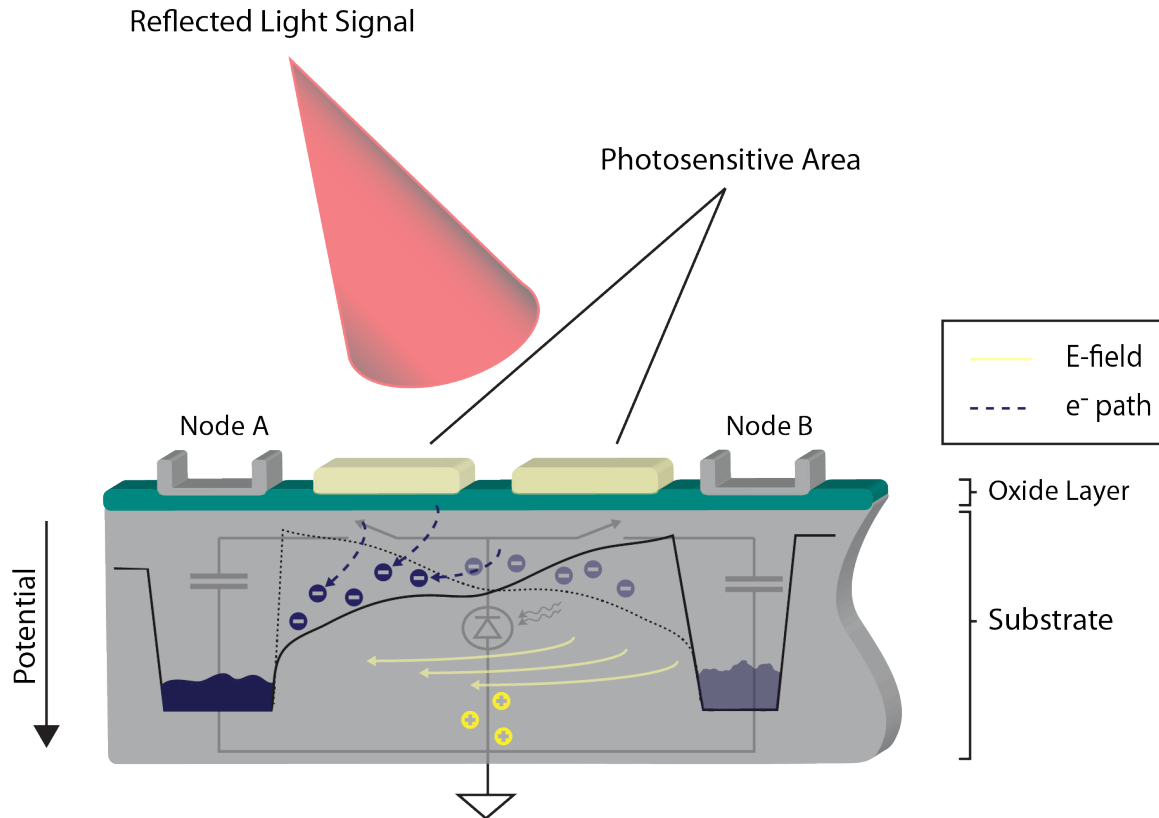
Figure 25: Illustration of a single demodulation pixel with two-tap architecture. This device can be thought of as two diodes connected by a common ground at the anodes. Incident light is collected in the photosensitive area of the pixel. The photosensitive area is separated from conductive MOS gates at Nodes A and B by a silicon oxide layer. When charge carriers are generated in the photo gates via the photoelectric effect, they are subject to the textitpush-pull voltages applied to the photo gates. The resulting electric field drives the charge to either Node A or B in a *dynamic see-saw motion* [4]. Continuing with the analogy to electronic circuits, this can be modeled as a fast switch that acts as an electro-optic shutter between two capacitors. The charge is then integrated on the capacitors of the respective nodes. During readout, the wells are discharged and the signal is given as difference between the two MOS gates.

recover information about ϕ and the modulated amplitude of the sinusoidal signal, a minimum of three sampling points, or *quads*, are required to interrogate the signal (for our application, four are used). This is referred to in literature as the *diagonal least-squares algorithm* [See [56] for more details], which dictates that resolution can be increased by sampling at equally-spaced intervals. In the case that at least one of the signals (reference or illumination) is sinusoidal then ϕ can be found by the measurement of the cross-correlation evaluated at the chosen phase step. The cross-correlation function $C(\tau)$ is defined as

$$C(\tau) = \lim_{T \to \infty} \frac{1}{T} \int_{-T/2}^{T/2} s(t) \cdot r(t + \tau) dt \qquad (3.1)$$

with the reflected modulated signal s(t) and reference oscillator signal r(t) defined as

$$s(t) = a_0 + a_m \cos(\Omega t - \phi) \quad \text{and} \quad r(t) = \cos(\Omega t) \qquad (3.2)$$

where a_0 represents the DC component of the signal and a_m and Ω are the modulation amplitude and frequency, respectively. In this simple case, we can exclude any phase offset due to electronics or propagation delay from transmission lines without loss of generality. Conversely, if it is desired to manually tune the phase readout, adjusting propagation delay by the addition or subtraction of cable length can prove to be a simple, yet effective technique for achieving this result[1]. Substituting for s(t) and r(t) in Equation 3.1, the cross-correlation is calculated as the following:

$$
\begin{aligned}
C(\tau) &= \lim_{T \to \infty} \frac{1}{T} \int_{-T/2}^{T/2} \left[a_0 + a_m \cos(\Omega t - \phi) \right] \cdot \left[\cos \Omega(t + \tau) \right] dt \qquad (3.3) \\
&= \lim_{T \to \infty} \frac{1}{T} \int_{-T/2}^{T/2} \left[\frac{a_m}{2} \cos(\Omega \tau - \phi) \right] dt \\
&= A_0 + A \cos(\varphi_i - \phi)
\end{aligned}
$$

A_0 comes out as an integration constant in Equation 3.3 and is the contribution from ambient light. Additionally, we have defined $A = a_m/2$ and $\Omega \tau_i = \varphi_i$. Calculating for four sampling points (i.e. $\varphi \in [0°, 90°, 180°, 270°]$), we arrive at a set of four equations with four unknowns, which describe the signal sampled at the various phase steps:

---

[1]For a detailed demonstration of this technique using the internal modulation system of the OPT8241-CDK-EVM refer to Section 4.1

$$C(\varphi_{0^\circ}) = A_0 + A\cos(\phi) \tag{3.4}$$

$$C(\varphi_{90^\circ}) = A_0 + A\sin(\phi) \tag{3.5}$$

$$C(\varphi_{180^\circ}) = A_0 - A\cos(\phi) \tag{3.6}$$

$$C(\varphi_{270^\circ}) = A_0 - A\sin(\phi) \tag{3.7}$$

The in-phase and quadrature components of the signal are found by evaluating the difference of Equations 3.4,3.6 and Equations 3.5,3.7. By taking the difference, we also see that the DC terms get subtracted out of the result, as shown here:

$$\mathrm{I} = C(\varphi_{0^\circ}) - C(\varphi_{180^\circ}) = 2A\cos(\phi) \tag{3.8}$$

and

$$\mathrm{Q} = C(\varphi_{90^\circ}) - C(\varphi_{270^\circ}) = 2A\sin(\phi) \tag{3.9}$$

The amplitude (A) can be found by calculating the magnitude of the measured RF signal in the complex plane. This is equivalent to evaluating the quadrature sum of the in-phase and quadrature components of the signal and normalizing by the square root of the number of samples (in this case four). Using similar complex analysis, the desired phase (ϕ) is calculated by evaluating the angle that the measured RF signal vector forms with the complex plane, or by calculating the inverse tangent of the quadrature and in-phase signal. This is a direct result of dividing Equation 3.9 by Equation 3.8, as shown here:

$$\mathrm{A} = \frac{\sqrt{I^2 + Q^2}}{2} \tag{3.10}$$

$$\phi = \angle[\mathrm{I} + i\mathrm{Q}] = \arctan\left(\frac{Q}{I}\right) \tag{3.11}$$

The DC signal contribution is simply the average over the measured quads. The importance of this result lie is the fact that information about DC and RF contributions of the incident light can determined in a single measurement by respectively adding or subtracting the measured pixel values.

$$A_0 = \frac{C(0) + C(\pi/2) + C(\pi) + C(3\pi/2)}{4} \tag{3.12}$$

The formalism above implies that the illumination signal and the sampling function are ideal sine waves. Typically, most commercially-available ToF cameras modulate the current to generate an amplitude modulated illumination signal (i.e. switch the laser source on and off at logic levels). In this case the harmonics of the square wave cannot be ignored, since around half of the total power is its harmonics. A complete analysis of how this effect is shown in [56]. In our setup, we avoid this by using an electro-optic modulator to generate a sinusoidal phase modulation on the incident light, which is converted into an intensity modulation by an external optical cavity.

This solves the problem of harmonic distortion; however, sampling with a square wave causes significant attenuation of the measured amplitude [57] assuming that sufficiently high demodulation frequencies aren't used (order of MHz). For high frequencies, the in-pixel demodulation becomes bandwidth limited and acts as a low pass filter for the reference signal.

3.3   The Practical Pixel: ToF Performance Characteristics

In the previous section I discussed the basic operating principles of ToF cameras and the innovation of how the PMD synchronously demodulates amplitude modulated light within the ToF camera. In the ideal pixel the conversion from measured photons to demodulated signal occurs without any significant attenuation or loss. Realistically, losses can vary depending on the wavelength of light used, choice of modulation frequency, and charge conversion efficiency. Additionally, non-linearity during demodulation can also produce signal distortion during readout, thus impacting camera performance. In this section, I will define these performance parameters within the context of ToF sensors, in particular the OPT8241-CDK-EVM.

3.3.1   Fill Factor

Because a CMOS sensor has control electronics built-in to the pixel, the subsequent light sensitive area is reduced. Additionally, electronics that allow for in-pixel demodulation in ToF cameras also contribute to the reduction of photosensitive area. The quantity known as the, pixel fill factor, represents this percentage of photosensitive pixel area ($A_{photosensitive}$) to total pixel area (A_{total}). This is given by the expression

$$F_p = \frac{A_{photosensitive}}{A_{total}} \tag{3.13}$$

This ratio also sets a limit on the amount of photons that can be accumulated in a single pixel during an integration period. ToF cameras with a *two-tap* pixel architecture, or two integration wells, typically have a fill factor of around 6.6% [57].

3.3.2 Quantum Efficiency and Responsivity

In addition to the fact that not all photons are capture by the pixel, during the charge generation process, not all photons are converted into charge carriers. The relationship which describes the fractional amount of total generated photoelectrons (n_e) from the number of incident photons (n_p) is known as the *quantum efficiency* $\eta(\lambda)$. The quantum efficiency depends on the wavelength of light used as well as the material parameters of the camera. Here we define the $\eta(\lambda)$ as

$$QE(\lambda) = \eta(\lambda) = \frac{n_e}{n_p} \tag{3.14}$$

For a silicon-based sensor, the QE is relatively low at wavelengths $> 1\mu m$. For the OPT8241-CDK-EVM we provide a rough order of magnitude estimate for the QE of 2% based on the measurements of [58] for a two-tap pixel. In ToF cameras the pixel architecture can also influence quantum efficiency. Studies show that placement of storage gates over the photosensitive area can lead to a reduction in quantum efficiency due to the absorption of light in silicon [59]. This issue is typically solved by positioning photogates on the sides of the photosensitive area as shown in Fig 25. The trade-off is that this architecture often results in a lower fill factor per pixel.

A similar quantity known as the responsivity R, which is related to η_λ, is sometimes more useful as it directly relates the input-output gain of the sensor in terms of light power to amount of photocurrent generated. The responsivity is given by

$$R = \eta \frac{q_e \lambda}{hc}, \tag{3.15}$$

where q_e is the electron charge, h is Planck's constant and c is the speed of light. A ROM estimate of the responsivity of silicon is around 0.3A/W for $1\mu m$ [60]. If we consider that the CMOS phase camera is uniformly illuminated by light source with an normalized intensity of 1W/m^2 and a pixel area of $225\mu m$ [61], then total

power per pixel is 225μW (this amount represents the ideal measured power per pixel without accounting for the optical fill factor). Using the responsivity for silicon, we can estimate that $67.5\ \mu$A of photocurrent is generated per pixel. This is a very small amount of current generated in each pixel; however, since our setup is not limited by low power surface emitting lasers , we are able to increase the amount of photocurrent generated, thereby improving SNR.

Additionally, this assumes that the illumination is uniform over the pixel array; however, in our design we utilize a beam with a Gaussian profile. In this case, we must determine a calibration target, which accounts for the integrated Gaussian beam over the sensor area – this is discussed in more detail in Section 4.3.2.

3.3.3 Demodulation Contrast

In interferometry, the contrast defines the ratio between the difference of the highest and lowest measurable signal and the the average of the highest and lowest measurable signal. The ideal contrast for an interferometer is 1, which means the highest and lowest signals are completely resolvable by the system. When discussing demodulation pixels, an analogous parameter known as the demodulation contrast can be used to characterize pixel performance.

The demodulation contrast is essentially a measure how well a demodulation pixel can distinguish between a modulated charge carrier and an unmodulated carrier. It is defined as the ratio of the measured RF amplitude to the ambient offset value

$$\text{Contrast} = \frac{A}{A_0} = 2 * \frac{\sqrt{\left[C(0) - C(\pi)\right]^2 + \left[C(\pi/2) - C(3\pi/2)\right]^2}}{C(0) + C(\pi/2) + C(\pi) + C(3\pi/2)} \tag{3.16}$$

One thing to note is that the demodulation contrast scales inversely with the modulating frequency. This is explained because the pixel is bandwidth limited at high frequencies, causing some photoelectrons to be omitted from one of the wells during the integration cycle. This leads to a reduction of the demodulated amplitude, thus reducing the contrast.

There are other material and functional parameters that can also influence the demodulation contrast, those include: *fringing fields, gate length, and wavelength.* Longer wavelengths can lead to longer diffusion times for the incident light, which

reduce the demodulation contrast. Conversely, higher fringe fields and shorter gate length between photogates contribute to an increase of charge separation between the nodes, thus increasing the contrast. For our experiment we keep the wavelength fixed to 1μm and the fringe fields and gate length are fixed parameters of the OPT8241-CDK-EVM.

3.3.4 Dynamic Range and Signal-to-Noise

A discussion on performance parameters for a ToF camera would not be complete without discussing the signal-to-noise (SNR) and dynamic range (D/R). These quantities, much like the contrast are useful for characterizing camera performance over the range of measurable values and at the shot-noise limited sensitivity. For a traditional ToF camera, the SNR is calculated as the ratio of the measured demodulated amplitude to the rms noise under illuminated conditions. In this case, the rms noise includes both dark and photon shot noise sources, since the integration is held active for the measurement. Because our measurements use a Gaussian laser source, the demodulated output is integrated and spatially-averaged and over the Gaussian profile.

$$SNR = \frac{\bar{A}}{\sigma_A} \tag{3.17}$$

Here, $\bar{A}$ denotes the spatial average over the demodulated amplitude and σ_A is the measured rms noise under illuminated conditions. The D/R delineates the range of signal levels that the camera can resolve. Quantifying the D/R is critical because a sufficiently high carrier field intensity can saturate the pixels of the ToF camera. Therefore, the D/R provides the user with the practical operating range of the camera. Here we define the dynamic range as the ratio of the saturation point (A_{sat}) to the noise floor (σ_{dark})

$$D/R = 20\,\log_{10}\left(\frac{A_{sat}}{\sigma_{dark}}\right) \tag{3.18}$$

The dynamic range for conventional two-tap demodulation pixels has been measured to be up to 71 dB for pixels not limited by significant amounts of dark noise [57, 56]. We report the measured dynamic range for the CMOS phase camera in Table 11. A discussion on the implications of these values is given in Section ??.

3.3.5 Influence of non-linearities in demodulation

Nonlinear effects from demodulation electronics can produce distortions in the readout. In this section we examine the influence of these linear and quadratic distortions on the phase and amplitude readout of the 4-phase demodulation scheme. To zeroth order, the amplitude and phase are calculated using Equations 3.10,3.11, respectively. To model the effects on phase and amplitude caused by control electronics (i.e. amplifier gain and nonlinear demodulation), we include first and second order correction terms to the measured RF readout. To second order, series expansion is as follows:

$$C(\varphi_i) = C_i + \alpha C_i + \beta C_i^2, \tag{3.19}$$

where α and β are the first and second order coefficients of the expansion. Substituting this into Equation 3.11, and solving for the measured phase ϕ results in:

$$\phi = \arctan\left[\frac{(C_0 - C_2) + \alpha\,(C_0 - C_2) + \beta\,(C_0^2 - C_2^2)}{(C_1 - C_3) + \alpha\,(C_1 - C_3) + \beta\,(C_1^2 - C_3^2)}\right]$$

$$= \arctan\left[\frac{(C_0 - C_2) + \alpha\,(C_0 - C_2) + \beta\,(C_0 - C_2)\,(C_0 + C_2)}{(C_1 - C_3) + \alpha\,(C_1 - C_3) + \beta\,(C_1 - C_3)\,(C_1 + C_3)}\right] \tag{3.20}$$

Using Equations 3.4,3.5,3.6, and 3.7 we can solve for the sum in the quadratic term, which simplifies to twice the DC value (A_0). Factoring constants in the expression gives

$$\phi = \arctan\left[\frac{(1 + \alpha + 2A_0\beta)\,(C_0 - C_2)}{(1 + \alpha + 2A_0\beta)\,(C_1 - C_3)}\right] = \arctan\left(\frac{C_0 - C_2}{C_1 - C_3}\right) \tag{3.21}$$

We see that both the linear and quadratic terms cancel out and the measured phase gives the same result as if there were no irregularities in the readout. The significance of this result illustrates the importance of using a two-tap demodulation pixel, as in the OPT8241-CDK-EVM. This result shows us that the phase readout will be insensitive to most disturbances caused by electronic sources (More information on noise sources will be discussed in Section 3.4). In most cases this means the phase readout will have higher sensitivity than the amplitude. By substituting Equation 3.19 in the expression for demodulated amplitude (Equation 3.10), one can see that these linear and quadratic effects do not cancel out. The result is shown here:

$$A = \frac{1 + \alpha + 2A_0\beta}{2}\sqrt{(C_0 - C_2)^2 - (C_1 - C_3)^2} \tag{3.22}$$

Another important point comes up by examining the result of Equation 3.22. We see that the quadratic dependence scales with the DC signal. The physical significance of this term, is that it accounts for uneven sampling intervals, where the unmodulated signal is not completely canceled by CBS. Techniques for mitigating these effects will be discussed in Section **??**.

3.4 Noise Sources in the CMOS phase camera

Since the CMOS phase camera is based on the OPT8241 ToF sensor, the readout is subject to noise related to both ToF imagers as well as CMOS sensors. There are four main noise sources worth mentioning when discussing limiting sources of noise in these sensors which include: (1) photon shot noise, (2) electronic noise, (3) fixed pattern noise and (4) quantization noise. In this section I will give a brief overview of these noise sources which limit sensing in the phase camera.

3.4.1 Electronic (Read) Noise

Electronic noise includes all noise sources involved in charge conversion and signal processing within the image sensor. In the time-of-flight camera, the charge transport characteristics of the demodulation pixel, such as the Johnson noise associated with the resetting of charge storage capacitors (*pixel reset noise*), contributes largely to the electronic noise floor[62]. Consider the demodulation pixel architecture shown in Fig.25, where each demodulation pixel can be modeled as have two charge storage nodes A and B with two switches moving charges between two capacitive wells. The behavior of an ideal capacitor is expected to be lossless, but in reality, we consider an equivalent series resistance (ESR), where a capacitor behaves like capacitor and resistor in series. Often, capacitors are used in series with resistors, so we consider the noise across two series resistors. The voltage variance, or single-sided power spectral density is given by:

$$\overline{v_{therm}(t)^2} = 4k_B TRB, \tag{3.23}$$

where B is the bandwidth of the circuit. The noise described by Eqn.3.23, known as the Johnson-Nyquist noise, is a limiting source of noise above the shot noise for most circuits. The RMS voltage noise can be found by substituting for the effective noise bandwidth of the circuit, 1/4RC, and by taking the square root of Eqn.3.23. To express this in terms of the RMS noise charge we use the relationship between charge and voltage for a capacitor, $N_{therm} = Cv_{therm}$.

$$N_{therm} = \sqrt{k_b TC} \tag{3.24}$$

Furthermore, we can express Eqn.3.24 by the number of electrons generated due to thermal fluctuations by dividing by the electron charge.

$$n_{therm} = \frac{\sqrt{k_b TC}}{q_e} \tag{3.25}$$

Eqn.3.25 reveals that even in the zero bandwidth limit, where the switch is open and resistance is infinite, there is still thermal noise due to charge left on the capacitor. In this sense, the thermal noise is due to the thermodynamic fluctuation of charge on the capacitor averaged over many reset events. Other types of noise included in the category of read noise include flicker and amplifier noise. These noise sources also depend on temperature and are as a result of the noise within the MOSFET device in each pixel. Because these noise sources are associated with the electronics of the camera, they can be estimated from image dark frames. Methods for estimating read noise are presented in Section 4.3

Other sources of electronic noise may be systematic in nature. Additionally, non-linear demodulation can manifest as a sinusoidal pattern in the demodulated output of the sensor [60]. Various techniques in signal processing [63, 64] have shown efficacy in correcting for these non-uniformities in the readout.

3.4.2 Quantization Noise

Quantization noise noise is the result when a continuous signal is sampled into discrete values. This occurs in either a dedicated quantizer or an analog-to-digital/digital-to-analog converter (ADC/DAC). In the case of the OPT8241-CDK-EVM, the ADC is responsible for sampling and digitization of the input signal. During sampling, the

time-varying analog signal is converted into a discrete-time signal, which is represented by a sequence of real numbers. These numbers are then assigned a particular signal level based on the bit depth of the converter. Modeling of quantization noise for an ideal N-bit converter was first proposed by W.R. Bennett in [65]. This simplified model assumes that the quantization steps Δ are relatively small compared to the signal fluctuations, such that the error due to quantization noise is relatively uniform over the sampling interval. In this case, the quantization error signal $q(t)$ is modeled as a sawtooth function with a slope of s:

$$q(t) = st, \quad -\frac{\Delta}{2s} < t < \frac{\Delta}{2s} \tag{3.26}$$

The root-mean-square quantization noise is then

$$\sigma_{quan} = \sqrt{\frac{s}{\Delta} \int_{-\frac{\Delta}{2s}}^{\frac{\Delta}{2s}} (st)^2 dt}$$

$$= \frac{\Delta^2}{\sqrt{12}} \tag{3.27}$$

One thing to notice about the result of Equation 3.27, is that the quantization noise is independent of the measured signal. Additionally, since $\Delta \sim 2^{-N}$ [66], where N is number of bits used in the ADC, the noise is reduced by a factor of 2^{2N} for each added bit. As noted, this model only applies when Δ is small compared to the signal amplitude, however, in the case where the signal is much smaller than the step size, then this model no longer applies and the quantization noise becomes signal dependent. The effects of quantization noise are apparent in the 4-bit, ambient readout channel of OPT8241-CDK-EVM we use in our system of which the implications will be discussed in Section 4.3.2.

3.4.3 Fixed Pattern Noise

Fixed pattern noise (FPN) describes the spatial noise associated with non-homogeneity between neighboring pixels on the sensor. Two sources of FPN commonly cited in CMOS image sensors are[63]:

1. *Dark current*: The current generated in the sensor when no photons are incident on the pixels. Typically dark current varies with both integration time and

temperature; therefore, for a given integration time and temperature, the dark current contributes a "fixed" offset term to the FPN. Removing FPN associated with the dark current, usually involves subtraction of the mean dark current from each of the measured image frames.

2. *Responsivity variations between pixels*: Differences in doping between pixels can lead to variations in photoelectron generation between pixels, which results in a signal-dependent gain term of the FPN.

FPN can be modeled as the signal-dependent noise in each frame [64]

$$\sigma_{FPN} = \alpha \, \tilde{C} + \beta, \tag{3.28}$$

where α is the gain and β is the column or row offset in the images. $\tilde{C}$ represents the true DC signal with additive Gaussian noise, which represents the temporal fluctuations of the signal contributing to the fixed pattern noise due to the gain. The FPN can be estimated by taking the spatial standard deviation of the uniformly illuminated image frames. Another method for estimating the pattern noise is taking the spatial standard deviation of a relatively constant signal region in an image frame, which is the method we use for our analysis. With the appropriate calibration factor (refer to section 4.3.2), the FPN can be expressed in terms of the number of electrons, which is necessary for providing a noise budget estimate.

It is worth noting that since σ_{FPN} varies as a function of the signal intensity, trivial background frame subtraction will not work to improve the SNR. Spatial averaging of frames can reduce the noise at the cost of signal resolution. It is also possible to use spatial filter images using fourier techniques to reduce the gain component of the FPN [64].

3.4.4   Modeling Shot Noise in the CMOS Phase Camera

Traditionally, signal shot noise is defined by the statistical uncertainty in the arrival time of incident photons on a detector. The distribution of these photons can be modeled using a Poisson distribution, which sets the uncertainty in photon detection equal to the square root of the DC photon flux (n_{DC} multiplied by the DC integration time (t_{DC}). Because we are concerned with the mean number of photoelectrons generated per unit time in the camera, we convert this value using the quantum efficiency. In

the case of the CMOS phase camera, the demodulation is also considering during the integration. To begin this analysis, we consider that the incident light is amplitude modulated at the frequency $\Omega = 2\pi f$. Therefore, we can describe a signal model for the measured signal which contains both the measured AC and DC photoelectron flux:

$$n(t) = n_{dc} + n_{ac} \cdot \cos(\Omega t) \tag{3.29}$$

where n_{ac} is the AC photoelectron flux. Demodulation is carried out as the integrated average over the measurement interval, T. By definition we find that the time-averaged photoelectron flux is given by:

$$< n_{AC} >_t \equiv \frac{1}{T} \int_{-\frac{T}{2}}^{\frac{T}{2}} n(t) \cdot (e^{i\Omega t} + e^{-i\Omega t}) \, dt \; = \; < n(t) \cdot 2\cos(\Omega t) >_t \tag{3.30}$$

where $< \quad >_t$ indicates the time-average. Here, we denote demodulation of the upper and lower sideband by the cosine term in the time-average. Similarly, the average DC photoelectron flux is given by:

$$< n_{DC} >_t \equiv \frac{1}{T} \int_{-\frac{T}{2}}^{\frac{T}{2}} n(t) \, dt \; = \; < n(t) >_t \tag{3.31}$$

The mean number of photoelectrons generated for given time interval is simply determined by evaluating the integration in Equations 3.30 and 3.31 for the AC and DC time interval, t_{AC} and t_{DC}, respectively:

$$< N_{AC} >_{t_{AC}} \equiv \int_{-\frac{t_{AC}}{2}}^{\frac{t_{AC}}{2}} < n(t) \cdot 2\cos(\Omega t) > \, dt \tag{3.32}$$

$$= n_{AC} \int_{-\frac{t_{AC}}{2}}^{\frac{t_{AC}}{2}} \left(\frac{1 + \cos(2\Omega t)}{2} \right) \, dt \tag{3.33}$$

$$= \frac{n_{AC} t_{AC}}{2} \quad (= 0 \text{ for noise}) \tag{3.34}$$

and,

$$< N_{DC} >_{t_{DC}} \equiv \int_{-\frac{t_{DC}}{2}}^{\frac{t_{DC}}{2}} < n(t) > dt \tag{3.35}$$

$$= \int_{-\frac{t_{DC}}{2}}^{\frac{t_{DC}}{2}} n_{DC} \, dt \tag{3.36}$$

$$= n_{DC} t_{DC} \quad (= 0 \text{ for noise}) \tag{3.37}$$

As we see from Equation 3.32, the unmodulated signal and higher frequency terms go to zero during the AC integration time. Similarly, in Equation 3.35, the modulated signal and higher frequency terms go to zero during the DC integration time. A factor of $1/2$ in Equation 3.32 accounts for the demodulation of the upper and lower sidebands. In both cases we have assumed that the only source of Gaussian noise comes from the statistical fluctuations of the generated charge carriers (modulated and unmodulated); therefore, the noise in each of these cases averages to zero. We can then calculate the variance of $< N_{AC} >$ and $< N_{DC} >$ using the following property of variances:

$$\sigma_X^2 \equiv < (X - \mu)^2 > = < X^2 > - < X >^2 , \tag{3.38}$$

where X represents a continuous random variable with a mean of μ. Substituting Equation 3.32 into Equation 3.38, we can determine the variance in the modulated number of photoelectrons:

$$\sigma_{N_{AC}}^2 =< N_{AC}^2 > - < N_{AC} >^2 \tag{3.39}$$

$$= \int_{-\frac{t_{AC}}{2}}^{\frac{t_{AC}}{2}} \int_{-\frac{t_{AC}}{2}}^{\frac{t_{AC}}{2}} < n(t)\, n(\tilde{t}) > \cdot \left(e^{i\Omega t} + e^{-i\Omega t} \right) \left(e^{i\Omega \tilde{t}} + e^{-i\Omega \tilde{t}} \right)\, dt\, d\tilde{t} \tag{3.40}$$

$$= \int_{-\frac{t_{AC}}{2}}^{\frac{t_{AC}}{2}} n(t) \left(e^{i\Omega t} + e^{-i\Omega t} \right) \delta(t - \tilde{t})\, dt \int_{-\frac{t_{AC}}{2}}^{\frac{t_{AC}}{2}} \left(e^{i\Omega \tilde{t}} + e^{-i\Omega \tilde{t}} \right)\, d\tilde{t} \tag{3.41}$$

$$= \int_{-\frac{t_{AC}}{2}}^{\frac{t_{AC}}{2}} n(\tilde{t}) \left(e^{i\Omega \tilde{t}} + e^{-i\Omega \tilde{t}} \right)^2\, d\tilde{t} \tag{3.42}$$

$$= \int_{-\frac{t_{AC}}{2}}^{\frac{t_{AC}}{2}} n(\tilde{t}) \left[2 + 2\cos\left(2\Omega \tilde{t} \right) \right]\, d\tilde{t} \tag{3.43}$$

$$= 2 \int_{-\frac{t_{AC}}{2}}^{\frac{t_{AC}}{2}} n(\tilde{t})\, d\tilde{t} = 2 n_{DC} t_{AC} \tag{3.44}$$

We can use the same method to determine the variance for the unmodulated signal component.

$$\sigma_{N_{DC}}^2 =< N_{DC}^2 > - < N_{DC} >^2 \tag{3.45}$$

$$= \int_{-\frac{t_{DC}}{2}}^{\frac{t_{DC}}{2}} \int_{-\frac{t_{DC}}{2}}^{\frac{t_{DC}}{2}} < n(t)\, n(\tilde{t}) >\, dt\, d\tilde{t} \tag{3.46}$$

$$= \int_{-\frac{t_{DC}}{2}}^{\frac{t_{DC}}{2}} \int_{-\frac{t_{DC}}{2}}^{\frac{t_{DC}}{2}} n(t)\, \delta(t - \tilde{t})\, dt\, d\tilde{t} \tag{3.47}$$

$$= \int_{-\frac{t_{DC}}{2}}^{\frac{t_{DC}}{2}} n(\tilde{t})\, d\tilde{t} = n_{DC} t_{DC} \tag{3.48}$$

The result of Equations 3.39 and 3.45 is as we would expect for statistical fluctuations of the input signal. We see that the variations in the DC signal are given by the square root of the photoelectron flux evaluated over the DC integration time, which agrees with the traditional definition for the shot noise limit. Interestingly, the measured fluctuations in the modulated light do not depend on the AC signal, but rather on the DC photoelectron flux over the AC integration time. The factor of two arises from the demodulation of both sidebands.

Ideally, the limiting noise sources for the CMOS phase camera have a Gaussian distribution [67, 68]. Under this assumption, the variance of each of the quadrature measurements is constant (σ^2). In this case, the total noise in the amplitude (σ_A) can be estimated as the quadrature sum over individual noise sources. The total phase noise (σ_ϕ) is estimated as the ratio of the total noise in amplitude to the mean amplitude of the signal, as phase and amplitude noise should be uncorrelated.

In this section I have discussed some of the limiting noise sources in the CMOS phase camera. Although shot noise is a limiting source of noise for most CMOS cameras, we find that this is not the case for our camera. The quantitative analysis of the noise in the CMOS phase camera will be discussed in Section **??**. The next section discusses the measurement procedure of the modulated sidebands used to estimate noise and modulation depth sensitivity thresholds.

Chapter 4

Demonstration of the Solid State Phase Camera

This chapter presents the work done toward developing a novel solid-state phase camera for use in the advanced LIGO detectors. This CMOS phase camera is based on a compact, commercially-available time-of-flight camera, the OPT8241 Camera Development Kit Evaluation Board (OPT8241-CDK-EVM), repurposed to function as an active wavefront sensor in a heterodyne sensing scheme. The first half of this chapter begins by covering the initial tests done with the base design of the camera. This includes measurement of the phase sensitivity of the camera by measuring the heterodyne beat produced by the misalignment TEM_{10} mode.

Section 4.3 discusses the performance characterization of our prototype CMOS phase camera design at Syracuse. This includes discussion of our experimental setup for measuring the sideband beat signal and calibration methods. Finally, section 4.3.4 presents the measurements to determine the phase sensing limit of our camera[1].

---

[1]Note that most of the information presented in Sections 4.3, such as figures and calculations are replicated from Muniz et al. (2021).

4.1 Initial Test using the OPT8241-CDK-EVM (Active Internal Modulation)

Here I report a quantitative study done to assess the phase sensing capabilities of the OPT8241-CDK-EVM in a heterodyne detection scheme. Here, the internal modulation of the OPT8241-CDK-EVM is used as the reference oscillator for phase modulating the incident light. Additionally, I demonstrate that OPT8241-CDK-EVM may be used for phase detection without the on-board illumination source, in an externally-illuminated configuration. For this measurement, the phase and amplitude (RF) and ambient (DC) readout of the OPT8241-CDK-EVM is measured as the demodulation phase is shifted via coaxial cable delay line.

4.1.1 Setup for Measuring Phase-Shifted Alignment Signal
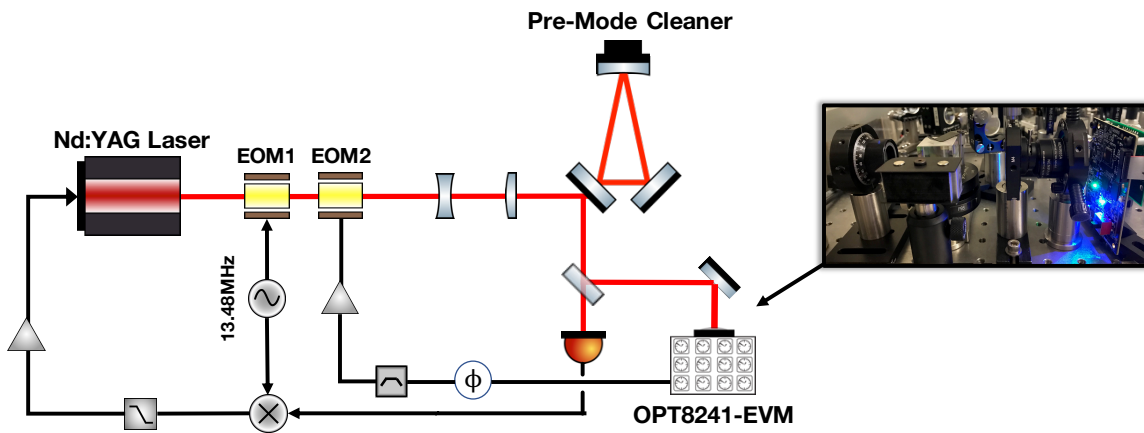
Figure 26: Optical setup for measuring the heterodyne beat in reflection of a PMC cavity.

An overview of the optical layout is shown in Figure 26. Here, the 1064 nm Nd:YAG laser is phase modulated by two separate EOMs–EOM1 and EOM2–generating sidebands at both 13.48 MHz and 25 MHz, respectively. A monolithic, triangular cavity–pre-mode cleaner (PMC) cavity–is used as a reference cavity for the measurement. The PMC is made to follow the laser frequency using a PDH locking method. In this scheme a broadband RF photodiode positioned in reflection of the cavity is used to measure the heterodyne beat between the 13.48 MHz sideband and the

carrier. The corresponding signal is demodulated to baseband frequencies and low pass filtered to remove high frequency terms. The actuation signal responds to relative phase changes between the carrier and sideband to produce an equivalent, but opposite change in the laser cavity length.

The modulated illumination drive signal, normally used to modulate the on-board illumination source, is routed out to drive EOM2. The square wave drive signal is then passed through a 2-30 MHz mini-circuits bandpass filter, to remove harmonics and ensure that the signal going to the EOM2 is completely sinsuoidal. Additionally, the output RF power of the signal taken after filter was measured at -2.8 dB (~ 0.52 mW), which was too low to drive EOM2. For this reason, a RF power amplifier was used to increase the drive signal to a range sufficient for generating phase modulated sidebands on EOM2 (20-26.99 dB, or 0.1-0.5 mW) [48].

To induce the appropriate phase delay ϕ for these measurements, varying lengths of coaxial cable were used. Electromagnetic theory tells us that the phase delay of an electromagnetic wave propagating through a non-dispersive medium depends solely on the frequency of the wave. This is theory is encompassed by the following relation [69]:

$$\phi(f) = 360° \cdot f \cdot \tau, \tag{4.1}$$

where f is the frequency of light and τ represents the delay time. Similar to the analog with optical cavities, the travel time of the signal depends on the physical length the cable, L, in this case. The permittivity ϵ, of the dielectric material is included as multiplicative constant which increases the effective length L_{eff} the signal propagates in the material.

$$\tau = \frac{L_{eff}}{c} \tag{4.2}$$

In the formula above, $L_{\text{eff}} = L\sqrt{\epsilon}$. Equation 4.2 can be substituted into Equation 4.1 to solve for the amount of cable length needed to produce a quadrature phase shift of the demodulated signal. For a signal at a frequency of 25 MHz and considering the dielectric constant of the material inside the coaxial cable ($\epsilon = 2.1$ [69]), the required length is calculated to be ≈ 2 m (6.6 ft) of cable length for a $\pi/2$ phase shift. The measurement was performed by adjusting the demodulation phase using

equally-spaced increments of coaxial cable–individually measured at 0.65 m ($\approx$ 2.1 ft)–for a total of 1.92 m or 83° in delay.

Capture Settings		
Parameter	Value	Comments
Frame Rate (fps)	50 fps	
Demodulation Frequency (MHz)	25 MHz	
Pixel Resolution (um)	15	This defines the average size of each pixel on the sensor array.
Quad Integration time (ms)	1.2	
Quads	4	Four quad readout is measured with $\pi/2$ phase-stepped demodulation; Six quad readout is measured with $\pi/3$ phase-stepped demodulation.
Sub-frames	4	The camera allows the capture of 1-4 sub-frames to construct a single frame. Each sub-frame is constructed with the readout of all the quads above.
Pixel Resolution (μm)	15	This defines the average size of each pixel on the sensor array.
DC Power (μW) [sensor; for incident beam of size $w_0 \approx$ 0.50 mm]	3.2	Incident power measured after 1.5 neutral density filtering.
DC Power (μW) [per pixel], estimated with beam size $w_0 \approx$ 0.50 mm	7.4 $\times 10^{-3}$	The incident power on each pixel in the sensor array

Table 6: The table summarizes the range of camera capture setting and the absolute rating for the illuminated signals.

The PMC cavity was locked to the carrier, TEM00 mode, and a slight cavity misalignment is induced to allow coupling of a higher order TEM10 into the sideband field. The beat between the carrier field and sideband field is measured in reflection of the PMC reference. A total of 100 illuminated and non-illuminated image frames were captured for each measurement. Image frames were acquired for DC, phase and amplitude read outs of the camera. The capture parameters for the measurements are summarized in Table 7

4.1.2   Results of Qualitative Analysis

The TEM00 mode is imaged on the ambient (DC) channel of the OPT8241-CDK-EVM, as shown in Figure 27. The TEM00 mode is unchanged in the DC image because the carrier power saturates the camera sensor (i.e. $P_0 >> P_{sb}$. Additionally, the DC component of the beam is insensitive to the changes demodulation phase produced by changing cable length. The native ambient data value is scaled such that a larger signal value is given by a lower digital number (DN) value (This is typically done because the DC value is uninteresting for many ToF camera applications). However, we scale the ambient data to represent a pixel saturation close to the highest digital number value of 15 for a 4-bit resolution. We find that the low resolution of the ADC results in significant quantization noise due to rounding error.

We also determine a rough estimate of the DC saturation per pixel. This is an important performance parameter because a high DC signal value can saturate the RF readout. For a 0.50 mm, beam the total incident power recorded after a 3% transmission filter was 3.2μW. The DC power per-pixel can then be calculated by integrating the total incident power over the area of the pixel:

$$P_{pix} = \int_{A_{pix}} I \cdot dA = I(0)d_{pix}^2 \tag{4.3}$$

We find that the total power per pixel is $7.4 \times 10^{-3}\mu$W.

The phase and amplitude, along with calculated I and Q images are shown for varying cable lengths in Figure 28. The ADC outputs phase and amplitude as a 12-bit DN value, at a 1.5 mrad/bit phase resolution (i.e. $2\pi/4096$). The I and Q image frames are calculated using Equations 3.8 and 3.9 and represent the signal after mixing. PDH theory tells us in the regime where the modulation frequency is
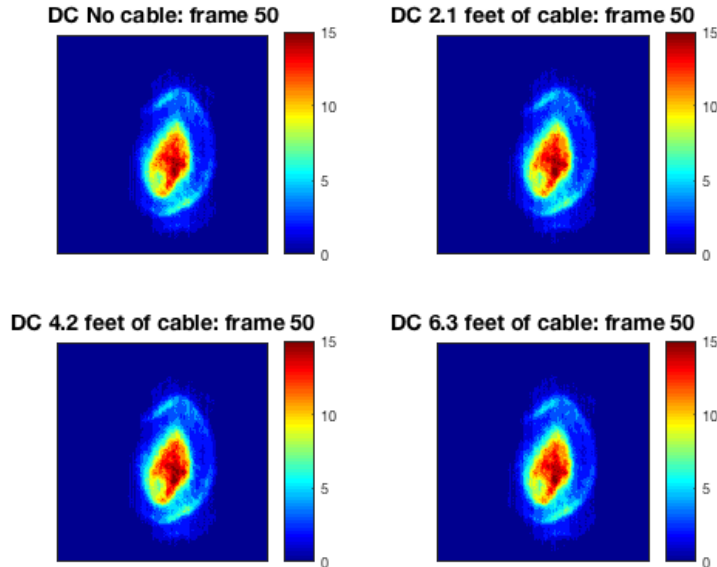
Figure 27: Single frame capture of the TEM00 mode measured in reflection of the PMC cavity. The image is captured in 4-bit resolution of the ambient (DC) readout channel.

high compared to the cavity response ($\Omega >> \Delta\nu_{\mathrm{fsr}}/\mathcal{F}$) the sidebands are completely reflected and only the imaginary, or sine term, remains in the error signal. As a result, the phase frames are more sensitive to quadrature phase shifts, as shown in Figure 28. However, we observe that the misalignment of our cavity results in an additional phase delay of the optical beat signal, which contributes a cosine term. This is shown in the calculated in-phase (I) component of the signal shown in Figure 28.

The TEM10 imaged in Figure 28 confirms the input beam is misaligned along the y-axis of the cavity. It should be noted that the slight tilt apparent in the images is associated with the global shuttering of the camera and not a result of the misalignment. We also see that the amplitude (magnitude) of the TEM10 mode remains constant between each measurement of phase. This is expected since the modulation depth ($\Gamma_{\mathrm{in}} = 0.147$) is held constant for these measurements. To determine if the measured phase shift is consistent with the theoretical estimate, we plot the phase of a single pixel value for each constant region of phase (Region A and B in Figure 29. The plot in Figure 29 shows the 2π wrapped phase as the length of the coaxial cable
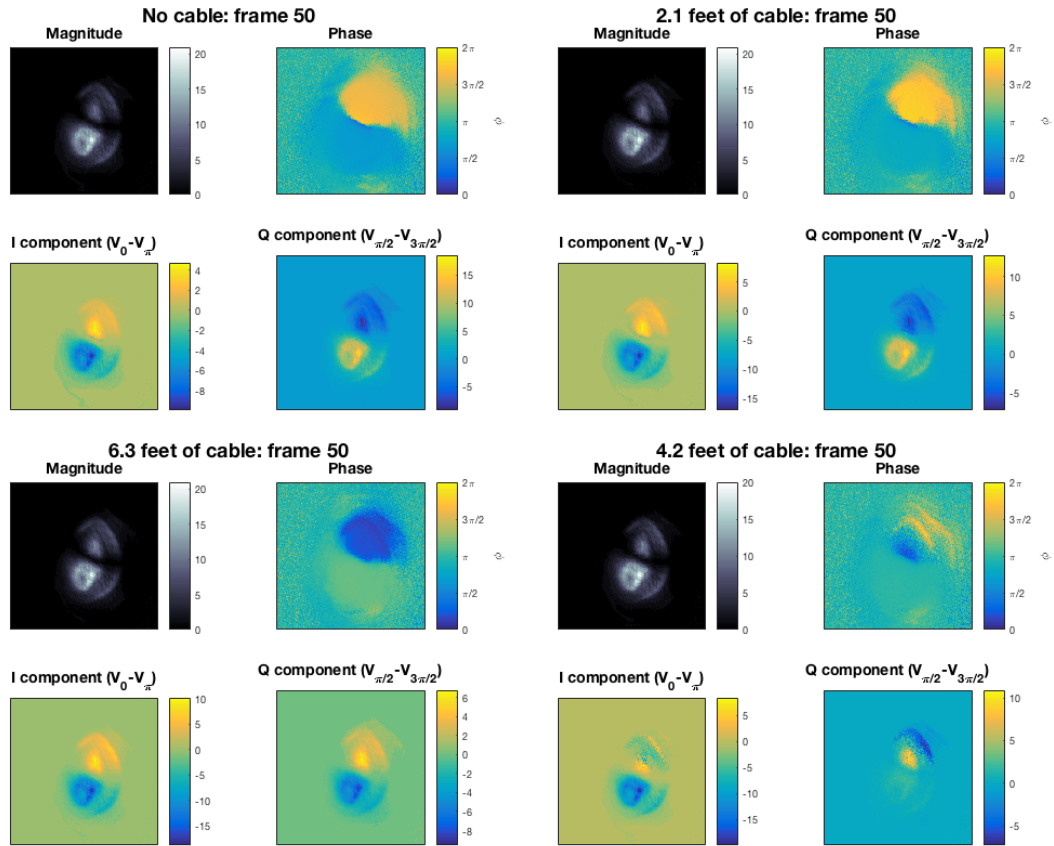
Figure 28: These images show phase and amplitude and the calculated I and Q as cable length is varied.
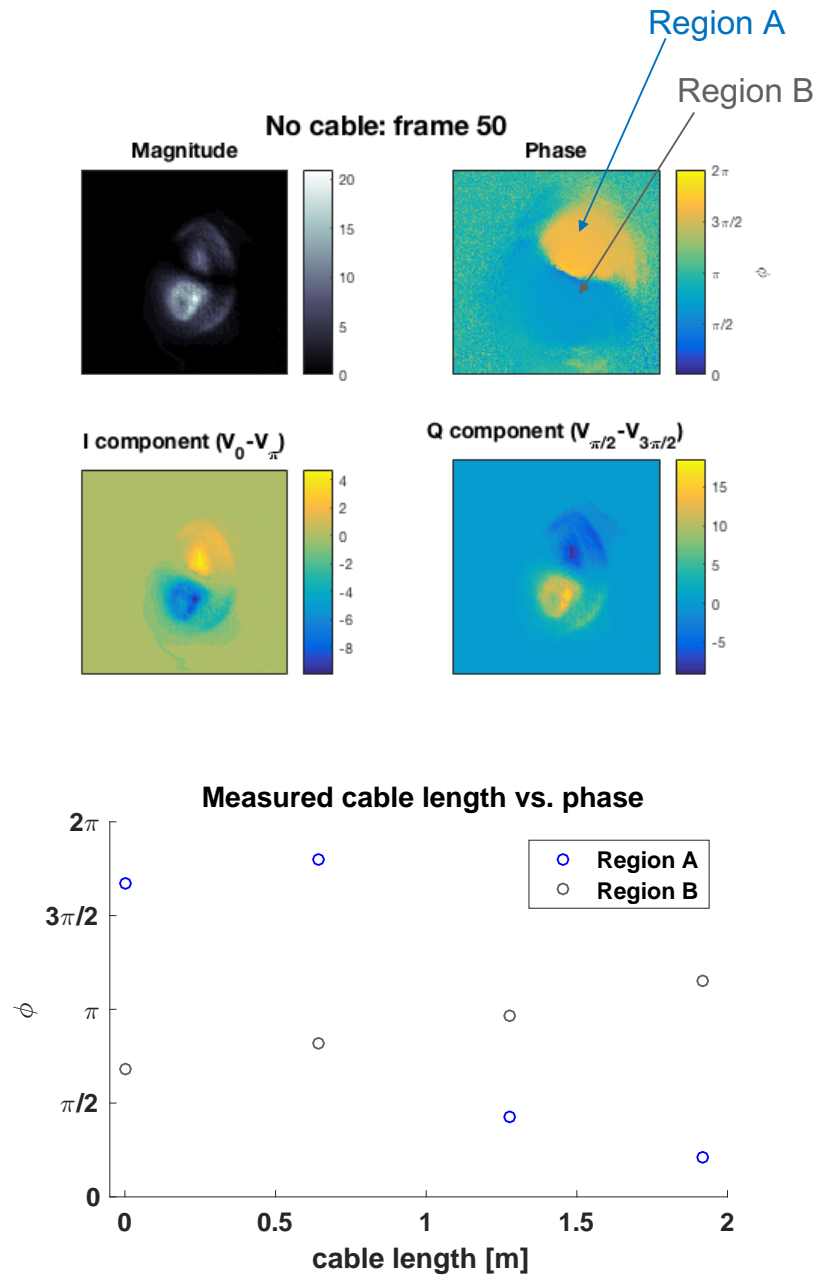
Figure 29: Plot of cable length vs. 2π-wrapped phase shift in radians.

is increased. It is clear to see that in Region A, the phase is shifted by $\approx \pi/2$ after a total of 1.92 m of cable length. Although less apparent from the plot in Figure 29, the phase in Region B also experiences a total phase shift of $\pi/2$.

In summary, this initial study demonstrates that the OPT8241-CDK-EVM is capable of sensing alignment modes and making phase sensitive measurements of amplitude modulated light from an external optical setup. The next steps to realizing this camera as a high-resolution wavefront sensor, is to modify the hardware to allow for user control of demodulation signals and frame timing. The next section details the hardware and software implementation in the CMOS phase camera to allow for this desired level of user control.

4.2   Design Architecture

Our design offers several advantages, one being that the electronic parts are commercially available and allow for rapid prototype, which we demonstrate. In this section, we cover the hardware and software changes necessary to realize external modulation and frame control using the OPT8241-CDK-EVM. First, I will highlight the required electronic components and how they are used in our design, then I will explain how we develop software to integrate each of these components and provide the demodulation signal to the camera during each integration period.

4.2.1   Hardware

This section presents the design architecture for the CMOS phase camera. The various electronic components, along with their functionality, are listed below and illustrated in Fig. 30.

Microcontroller

We use the STM32F407VGT6-Discovery Board (shown in Fig. 31) to control waveform generation and frame synchronization in our camera. The discovery board features the ARM Cortex-M4 32-bit microcontroller in a 100-pin LQFP package. The low power operation (requiring only a 3 V and 5 V line) and general purpose I/O pin logic, make this discovery board ideal for our integrated electronics setup. Firmware is transferred to the microcontroller from the host CPU via a high-speed mini-USB
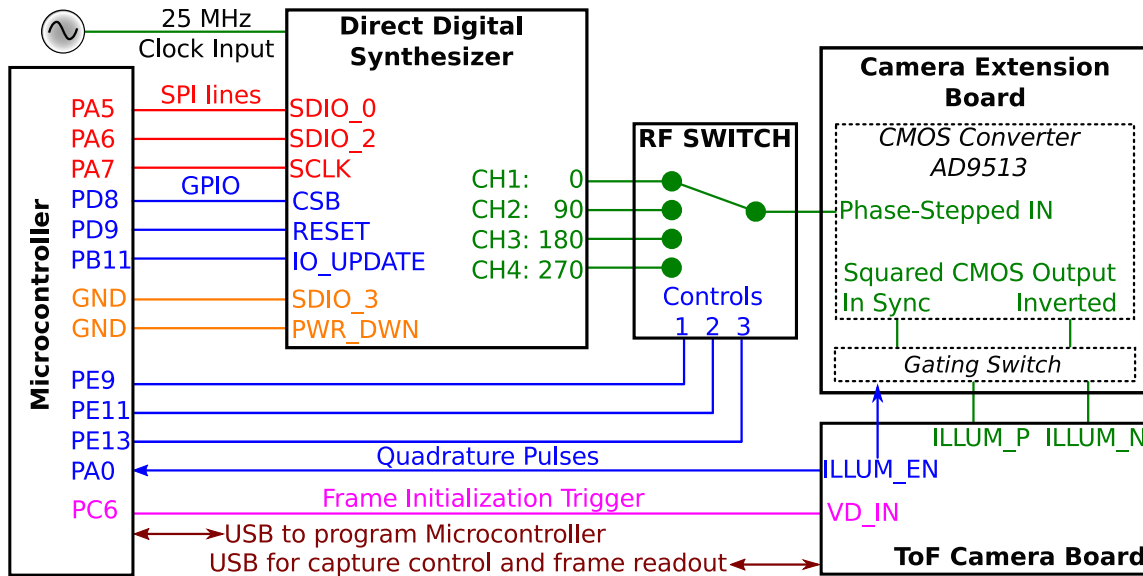
Figure 30: The image above shows the system's overview of the phase camera signal chain and design components. The microcontroller acts as the host device controlling waveform generation and image frame capture. This process begins with the microcontroller initializing a Direct Digital Synthesizer (DDS) board driven at the clock frequency input. During initialization, quadrature phase-stepped signals are generated on the four analog output channels of the DDS. The signals are then sent to a RF switch, which waits for the frame capture sequence before allowing the signals to pass to the camera. During frame capture, a frame initialization trigger is sent out by the microcontroller to the ToF camera board. The camera responds sending a series of quadrature pulses back to the microcontroller, which are used in an interrupt sequence as control signals for the RF switch logic. This ensures that the output waveform is synchronized with the clock input (i.e. phase-locked) before going to the camera. After the signal passes through the RF switch, it is conditioned by the electronics in the Camera Extension Board. A CMOS converter, squares the analog modulation signal from the DDS and provides an additional inverted output that is only used to for driving the camera system clock. These signals are then passed through a gating switch, which removes transient noise from the squared input to the camera.
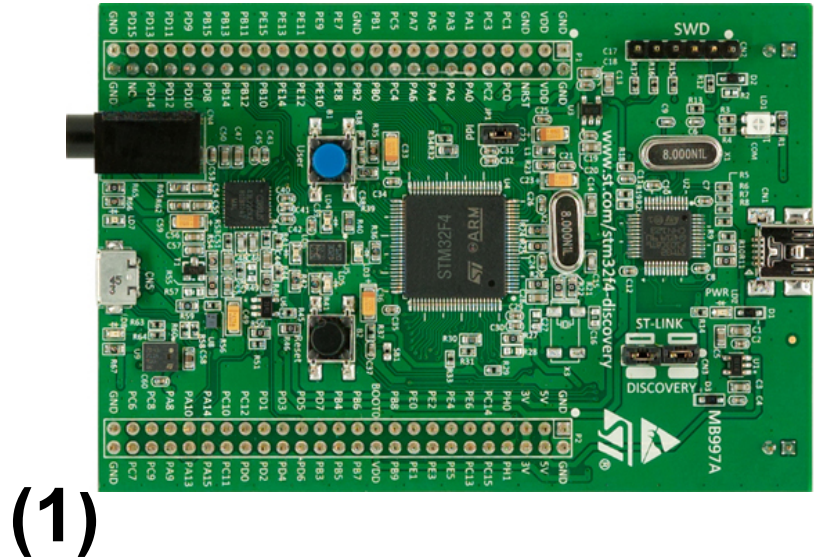
(1)

Figure 31: An image of the STM32F407VGT6-Discovery Board.

interface. Software integration and programming flow for the CMOS phase camera is delineated in Section 4.2.2.

The microcontroller interfaces with a Direct Digital Synthesizer (DDS) board to begin the waveform generation process. This process begins when SPI lines on the microcontroller transmits a data sequence to initialize each of the individual channels on the DDS board. The microcontroller controls when the frame capture sequence on the camera begins by sending out a frame initialization pulse, which is also used to set the camera frame rate. ToF camera board responds by sending a series of pulses (typically 4) within the span of the frame initialization pulse. Each of these pulses are used in an interrupt sequence to determine when the DDS outputs each of the phase-stepped demodulation (quad) signals. In the version of the board represented in Fig. 30, the control logic is passed to a RF switch, which is used to switch between the four analog output channels of the DDS during each quad integration period.

Direct Digital Synthesizer (DDS)

The CMOS phase camera electronic design uses the AD9959 Direct Digital Synthesizer (DDS) evaluation board for the demodulation signal generation. The DDS board features a 32-bit frequency, 14-bit phase, and 10-bit amplitude tuning resolution for
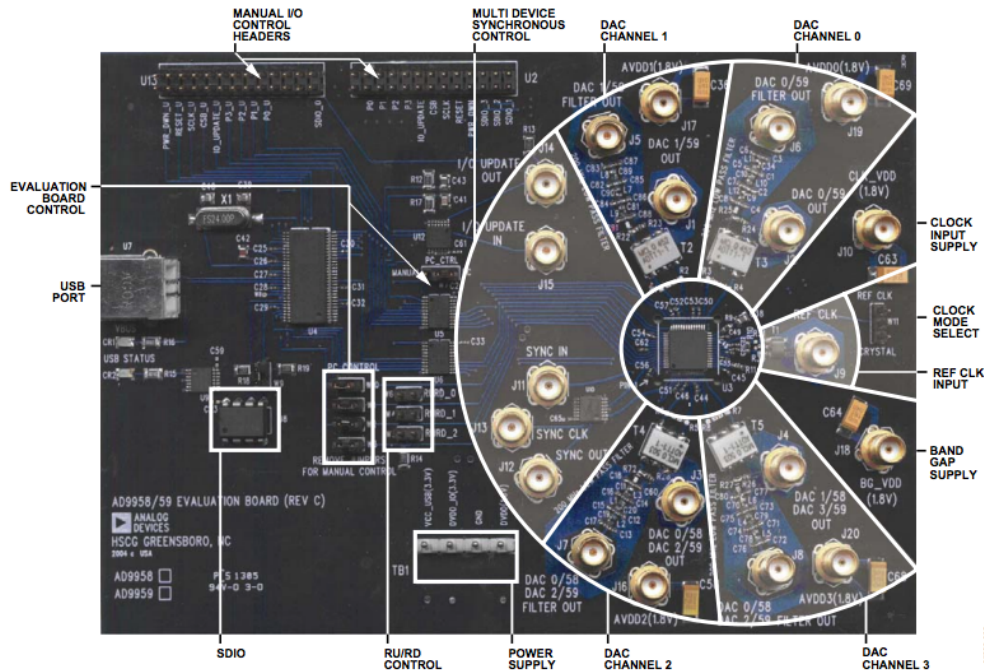
Figure 32: The AD9959 Direct Digital Synthesizer Evaluation Board [5].

high-precision signal generation. The I/O circuitry, USB and digital and analog outputs are all powered on a 3.3V and 5V, supply for low power operation. The board also features four analog outputs, which are synchronized analog output, which are all synchronized to the reference clock signal. The AD9959 has four internal DDS cores consisting of a 32-bit phase accumulator and phase-to-amplitude converter, which sample the input clock signal to generate a digital sine wave on each of the four output channels. Each of the channels can be independently tuned in frequency (up to 500 MHz), phase, and amplitude by providing the appropriate tuning word via SPI data transfer. The frequency tuning word is calculated using the following equation:

$$FTW = \frac{(2^{32})(f_{OUT})}{f_{CLK}}, \tag{4.4}$$

where f_{CLK} is the system clock frequency of the DDS (400 MHz), f_{OUT} is the desired output frequency of the DDS channel, and 2^{32} represents the resolution of the phase accumulator. The FTW is represented as a decimal value ($0 \leq$ FTW $\leq 2^{31}$), but is transferred as a binary value from the microcontroller to the DDS. Additionally the phase of each of the channels can be independently tuned using a phase offset word

(POW), which allows for a programmable offset in phase with respect to each of the channels. The phase offset word can be calculated using the following equation:

$$PTW = \frac{(\Phi)(2^{14})}{360},\tag{4.5}$$

where 2^{14} is the resolution of the register that stores the phase value, Φ is the desired phase output and 360 represents the total phase value.

In our setup we operate the DDS in a *single-tone mode* by first initializing the DDS with a master reset signal upon boot up [5]. This occurs when the microcontroller sends an active low signal to RESET pin of the DDS. Operation in this mode allows for the DAC channels to be independently programmed in frequency and phase, which we utilize in the next step. More details on software used to program the DDS and single-tone mode operation are provided in section 4.2.2 and in the Appendix.

We use the external reference local oscillator (LO) as input for the reference clock (REF_CLK) on the DDS. The frequency range for this input is between 1 MHz and 500 MHz and the input voltage range is between 200 mV to 1000 mV. In our setup the 25 MHz signal from the oscillator outputs at a voltage of 3.3 V, so we attenuate the signal before sending it to the DDS board. As mentioned, all channels are internally synchronized to the reference clock signal. During initialization and frame capture, instructions are passed from the microcontroller to the DDS via SPI lines. In order to update the registers on the DDS the microcontroller must enable the address register bits through a data update sequence on the "IO update" pin of the DDS. This is discussed in further detail in section 4.2.2. We program the DDS to offset each of the four channels by the respective phase delays of: $\Phi = $ 0º, 90º, 180º, 270º, with respect to the reference clock signal set at the user-defined demodulation frequency f_{demod}.

It is important to note that there is an inherent delay ($\approx 1ms$) between phase steps imposed by the IO update sequence. Because of this, we use either an RF switch or synchronization flip-flop to ensure that the phase-stepped outputs remain synchronized with the reference LO. Next, I will discuss the use of the RF switch and flip-flop in our CMOS phase camera design.

RF Switch

We use a single-pole four throw (SP4T) from Mini-Circuits (JSW4-272DR+) to switch between the four phase-stepped outputs of the DDS board, viz. $\Phi = 0°, 90°, 180°, 270°$. The switching time for this RF switch is 1.9 μs to turn to the "ON" state and 1.4 μs to turn to the "OFF" state, which is suitable for the frame timing requirements of our camera. The microcontroller controls the RF switch through three logic control inputs, which can each be set to either a "HIGH (H)" or "LOW (L)" input state. Setting all the control inputs to a low state, results in continuity between the RF common port and the RF input port 1. Conversely, setting all the control inputs to a high state, puts the RF switch in a quiescent state. Additionally, combination of high and low states are used to switch between the other three inputs on the switch.

In our electronics design, we assign three microcontroller pins (PE9, PE10, PE11) to control logic input 1,2, and 3, respectively. An interrupt sequence, triggered by the quadrature pulses from the camera, is used to control the output logic from the microcontroller. This ensures that the RF switch only switches between the four input ports during the appropriate phase step. During the low period of a quadrature pulse, the microcontroller switches off to allow for readout of the phase-stepped signal. This ensures any noise from the high frequency demodulation signal is gated during the readout sequence. One advantage of using the RF switch is that the frequency bandwidth of the switch (5 MHz to 2700 MHz) is within the operating range required for imaging the 9 MHz and 45 MHz sidebands we are interested in for application in LIGO.

Synchronization Flip-Flop

A common issue encountered when updating the phase offset on the DDS board is ensuring that the latency is fixed between phase-stepping when using SPI data transfer. Otherwise, uncertainty in timing can result when the synchronization clock (one-fourth of the system clock) oversamples the update pulse (I/O update) used to update the phase offset register value [5]. We find this issue often appears during a master reset of the microcontroller, where the initial "zero" phase jumps between different offset values. We resolve this issue by using an asynchronous J-K flip-flop (CD54ACT109). The flip-flop ensures the same relative phase on every camera startup by updating

the phase registers synchronously with the rising edge of the external LO clock input (we define this as a *phase-locked* system). The update sequence is also programmed to last greater than one period of the synchronization clock of the DDS (>10 ns) in order to meet the DDS timing requirements for the I/O update pulse.

We operate the flip-flop on a 5 V supply to allow for a maximum clock frequency input up to 68 MHz. The microcontroller output, normally used to update the registers on the DDS, is passed to the J input of the flip-flop. Additionally, a second logic signal from the microcontroller is assigned to the $\overline{\text{CLR}}$ input on the flip-flop. The logic table for application is provided below:

Inputs					Outputs		Function
$\overline{CLR}$	$\overline{PR}$	J	K	CLK	Q	$\overline{Q}$	
H	H	H	L	Rising Edge	H	L	
L	H	–	–	–	L	H	Clear

Table 7: Logic used for programming the flip-flop.

In our design, we have established two use cases for the flip-flop: 1) in conjunction with the RF switch and 2) standalone. The first approach is similar to that mentioned in Section 4.2.1, with the exception that the demodulation phase is always fixed upon reset events. We find the first method of operation to be more robust as the it does not rely on a synchronized register update for every phase step, but is limited to four demodulation steps and supports only a single frequency input. The second approach uses the flip-flop to actively update the registers *and* phase-step the output of one of the DDS channels in accordance with the quadrature pulses from the camera. This would allow for more than four phase steps to be used for greater phase resolution and only a single output port of the DDS is needed.

One might also imagine that a secondary RF switch can be used at the input to allow for the imaging of different modulation frequencies in real-time. This scheme can also be performed with the two use cases mentioned above. Although, we have yet to realize this scheme in our current design, we present this as a future work in Section **??**.
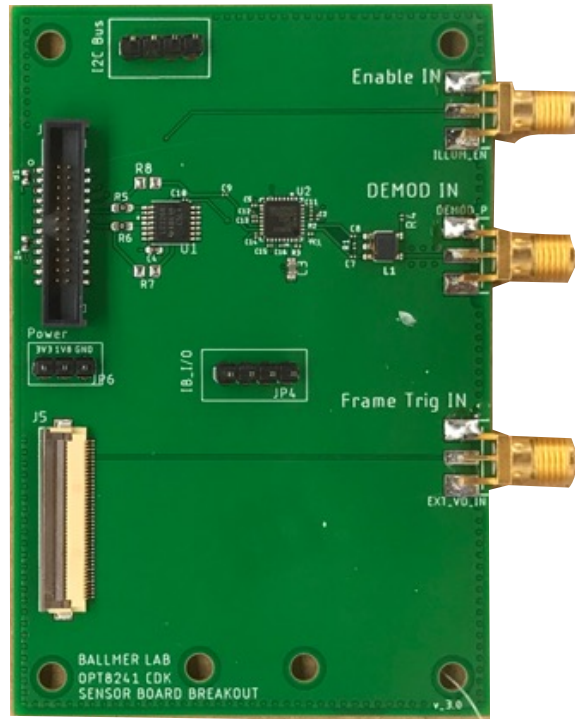
Figure 33: In-house camera extension board designed for signal conditioning and interfacing with the camera board.

Camera Extension Board

A custom extension board (shown in Fig. 33) was built for signal conditioning and to interface with the camera board. The functionality of the board is to receive the analog, phase-stepped output from the DDS, convert that signal to CMOS logic levels and gate the output signal during quadrature pulse integration periods. The board also routes the quadrature pulses from the camera board to the microcontroller and the frame initialization triggers to the camera using RF-shielded connections. To convert the sinusoidal reference signal to a CMOS logic level clock, i.e. 'squaring the clock', we use a high-speed clock distribution integrated circuit (Analog Devices AD9513). Also on the extension board is an additional high-speed buffer chip (Texas Instrument's SN74LVC126A), used to gate the output demodulation waveform during each quad exposure. During the off state of the buffer, the output goes to high impedance, which eliminates transient noise between quads.

All firmware is developed within the Keil μVision IDE and flashed to the MC
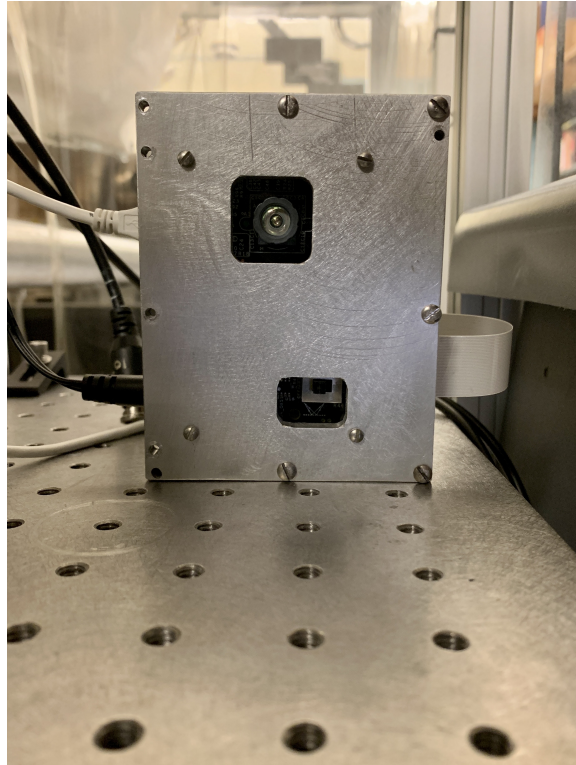
Figure 34: Custom-built enclosure for the CMOS phase camera sensor board and extension board.

via a USB interface. This allows the MC to run as the master device after an initial reset event. Firmware and capture and control operation will be discussed in the next section.

Camera Housing Unit

We have also designed an enclosure to house the OPT8241-CDK-EVM and extension board. This is done to ensure that any noise on the demodulation channels due to external RF signal coupling is mitigated. The metallic enclosure design is shown in Figure 34.

4.2.2 Software

Software implementation in our prototype CMOS phase camera is realized in simple three steps: initialization, response, and capture/readout. The flow chart shown in Fig. 35 gives a general overview of the control and capture process of our camera. In
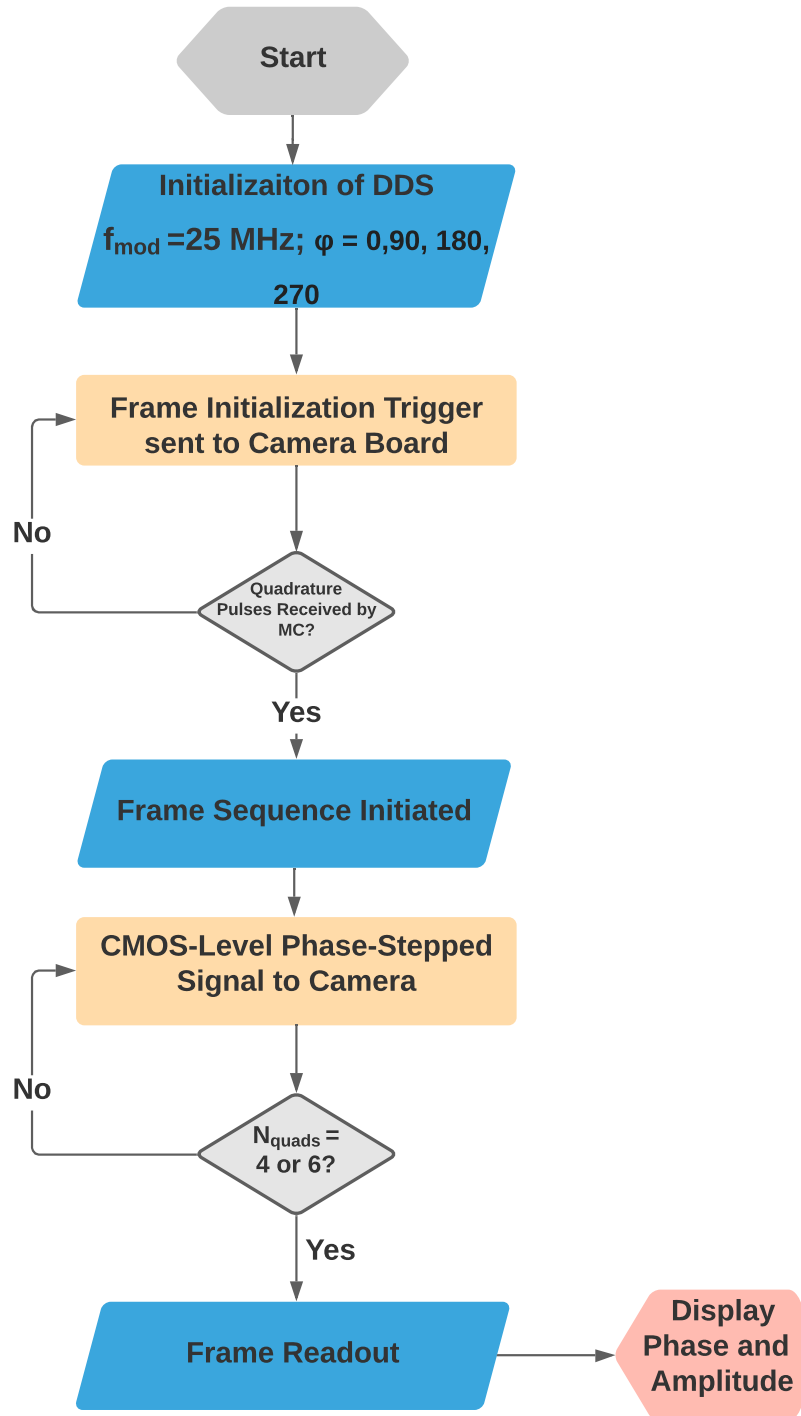
Figure 35: Dataflow in our CMOS phase camera design.

this section, I will discuss the details of each of these processes as well as describe how we use the microcontroller to interface the DDS board and control frame sequencing on the camera board. Finally, I will provide a complete description of the frame capture timing. We utilize the STM32CubeMX graphical tool to initialize the relevant hardware abstraction layer (HAL) drivers and set the clock frequency of the microcontroller (168 MHz). Programming development is done within μVision IDE.

Initialization

Initialization of the CMOS phase camera, is the process during which the microcontroller prepares the DDS for waveform generation. This begins when the GPIO line (PD9) pulls down the active high reset pin of the DDS and issues a master reset of active registers on the DDS. After issuing a master reset, frequency, phase and amplitude can be controlled independently for each output channel of the DDS (i.e. *single-tone mode*).

Before tuning frequency and phase, the boot-up parameters of the DDS are set by enabling and assigning value to the appropriate register functions. During every data transfer sequence, the chip select (CSB) pin on the DDS must be held low. For this task, we assign the GPIO pin (PD8) on the microcontroller. This process enables the user to write a sequence of data to the registers, starting with the least significant bit (LSB)[2]. We operate the DDS in a single-bit serial mode using a 2-wire connection for SPI communication. In this mode, two lines are used for master-input-slave-output (MISO) and master-output-slave-input (MOSI) communication, which is essentially SPI protocol for reading/writing operations between the microcontroller and DDS. In our system, we assign GPIO pins–PA6 and PA5, respectively– for SPI communication. An additional line for controlling the serial clock (SCLK), is assigned to the GPIO pin (PA7). During communication, 8-bit data sequences are written to the assigned function register. A description of the most significant register functions we use, as well as what we use them for is provided here:

---

[2]Note:For operation where the DDS is not synchronized with the input clock signal, the I/O update pulse (<20 ms) (PB11) is directly passed to the DDS to update the registers after data transfer. When the DDS is synchronized with the input clock, the I/O update pulse is instead passed as an input to a synchronization flip-flop. The flip-flop then waits (<240 ms) for a rising edge of the input clock before triggering an I/O update sequence on the DDS.

- *Channel Select Register (CSR) [Address – 0x00]*: The channel select register is used for enabling the individual channels of the DDS. It also assigns the order in which data is read by the DDS–we program this register such that the LSB is read first.

- *Function Register 1 (FR1) [Address – 0x01]*: This register is primarily used for setting the system clock (SCLK) of the DDS. The multiplier of the phase-locked loop (PLL) is set to multiply the input reference clock by a factor 16 which sets the DDS system clock to the maximum frequency of 400 MHz. This register is also programmed to allow the microcontroller to externally power down all functions on the DDS board.

- *Function Register 2 (FR2) [Address – 0x02]*: This register is used to "zero" the phase and frequency accumulators of the DDS.

- *Channel Function Register 3 (CFR3) [Address – 0x03]*: This register sets the phase accumulator to automatically and synchronously clear every time an I/O update signal is received by the DDS. This ensures no initial offset in phase between the channels of the DDS. This register is also responsible for setting the output waveform of the DDS– in our case, a sine wave.

- *Channel Frequency Tuning Word 0 (CFTW0) [Address – 0x04]*: 32-bit register used to set the output frequency on each of the DDS channels. First, the desired output channel is addressed, then the frequency tuning word is written to the register value. The register values do not update until an I/O update sequence is initiated.

- *Channel Phase Offset Word 0 (CPOW0) [Address – 0x05]*: 16-bit register used to set the output phase on each of the DDS channels. First, the desired output channel is addressed, then the phase offset word is written to the register value. The register values do not update until an I/O update sequence is initiated.

After initialization is complete, the DDS generates four, quadrature phase-stepped sine signals on each of the respective output channels. At this stage, the RF switch remains inactive so the modulation signal is prevented from reaching the camera. It

is only when the microcontroller receives a response from the camera board, that the phase-stepped signals are sent to the camera.

Response

In the response phase, the microcontroller begins by sending a frame initialization trigger (PC6) to the camera board. The frequency of the pulsed signal is set to match the desired frame rate of the camera and the pulse duration is set to be greater than the minimum required for normal camera operation ($>$ 2 system clock cycles of the OPT8241-CDK-EVM). The system clock of the camera board is set at 24 MHz by default [61], so for our measurements we set the frame rate at 7.1 Hz with a pulse duration of 19.50 ms.

This trigger pulse puts the camera board in a slave mode operation and initiates the frame capture process. During this process, the camera board produces four quadrature pulses which are sent to the microcontroller on an external interrupt line (PA0). Each of the pulses trigger a separate interrupt event. The interrupt sequence starts an internal counter (TIM3) in the microcontroller which is used for exposure timing of the quadrature captures. The active input port of the RF switch is left on during this period ($\approx$ 1 ms for each quad), and then turned off after integration. If the flip-flop is used instead, then the quadrature pulses are used to step the phase on a single channel of the DDS.

Additional GPIO pins are assigned to control logic 1,2, and 3 of the RF switch – PE9,PE11,and PE13, respectively. The truth table for controlling the RF switch is given below:

Capture/Readout

The timing diagram for a single frame capture and readout is shown in Fig. 36. To begin frame capture, we run a custom Python script which connects to the host camera/cameras and sets the parameters for frame capture (e.g. integration time, quad count and subframe count). The register settings are set according to [70] to allow for the use of externally modulated signals to be sent to the camera. It is important to note that the internal clock of the camera must be disabled (''tg_dis'') before changing the camera parameters. The measurement type is also designated

Inputs			Outputs			
Control 1	Control 2	Control 3	RF1	RF2	RF3	RF4
L	L	L	ON	–	–	–
L	L	H	–	ON	–	–
H	L	L	–	–	ON	–
H	L	H	–	–	–	ON
H	H	H	–	–	–	–

Table 8: Logic used for controlling the RF switch.

(i.e. depth—amplitude and phase, or IQ) and the output data is rescaled to the QVGA format of the camera. As mentioned, the frame capture sequence begins with an initialization trigger, which sets the frame rate. The quadrature pulse period then sets the integration time for the demodulated signal in the camera. After the conclusion of each integration period, the signals are converted via the ADC within in each pixel and assigned a digital number value based on the bit resolution of the ADC.

The camera calculates the in-phase and quadrature information from the raw data stream and processes this in terms of the phase and amplitude of the signal. We use the Voxel Viewer software, to record the phase and amplitude image frames for subsequent analysis. More on the analysis process will be discussed in the next sections.

4.3 Performance Characterization of the Solid State Phase Camera

4.3.1 Experimental Design

The experimental setup shown in Fig 37 was used for the measurement and calibration of the CMOS phase camera. In this setup, a reference, triangular cavity Fig 37 is used to stabilize the frequency of a 1064 nm Nd:YAG laser via Pound-Drever-Hall (PDH) locking. The PMC has a finesse of 165 and features a piezoelectric-actuated (PZT) mirror at the apex which allows for tuning of the cavity resonance. The carrier field,
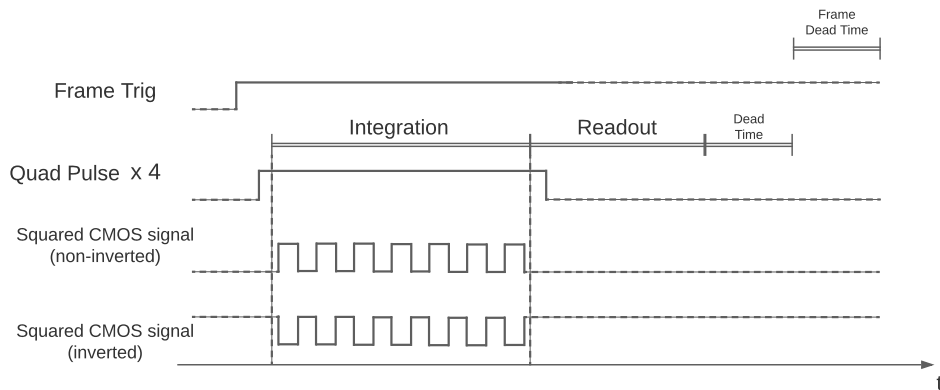
Figure 36: Timing diagram for a single frame capture of the CMOS phase camera. The nominal integration period for a single quad is ≈ 1.1 ms for a frame rate of 7 Hz. The readout and dead time in this case are ≈ 2.9 ms. These values are multiplied by a factor of 4 for a four quad measurement capture.

$E_c = E_0 e^{i\omega_c t}$, is phase-modulated using a resonant electro-optic modulator (EOM) referenced to a 25-MHz local oscillator. This process adds sidebands to the optical carrier field which are offset at the modulation frequency $\Omega/2\pi$. The peak-to-peak drive voltage of the LO determines the amount of phase modulation, or the phase modulation index Γ, the field incident on the PMC is given by

$$E_{in} = E_c e^{i\Gamma cos\Omega t} \tag{4.6}$$

Since $\Gamma << 1$, we can apply a Taylor expansion to the exponential term and using the simple identity for cosine,

$$E_{in} \approx E_c \left(1 + i\Gamma cos\Omega t\right) \tag{4.7}$$

$$= E_c \left(1 + \frac{i\Gamma}{2}e^{i\Omega t} + \frac{i\Gamma}{2}e^{-i\Omega t}\right) \tag{4.8}$$

We see that the frequency response of the cavity produces a separate phase and amplitude change in the carrier and sidebands, respectively. This change is described by the complex response function of the cavity:
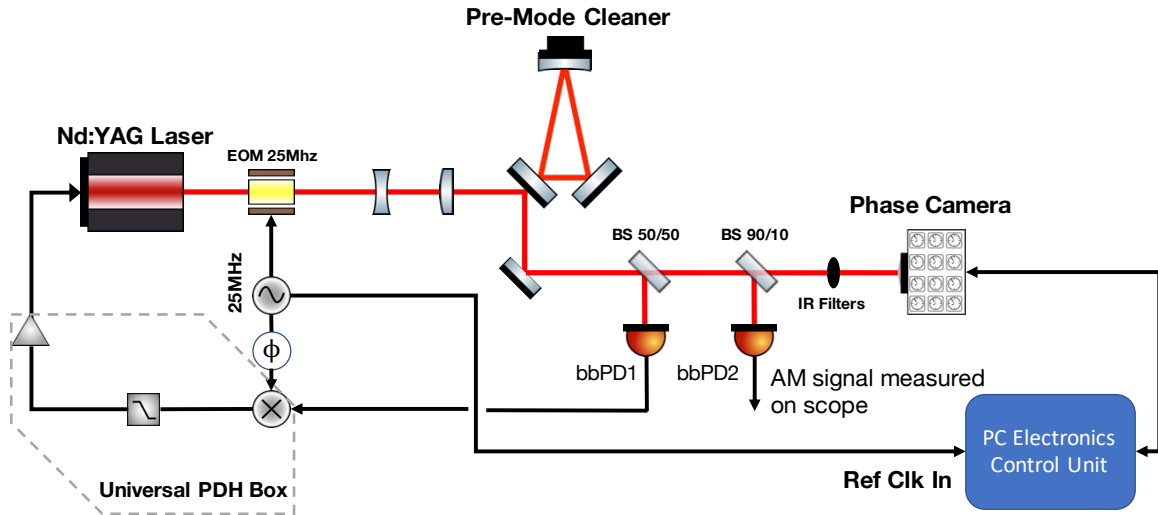
Figure 37: The experimental layout used for testing and quantifying the noise levels of the phase camera. The laser is stabilized by locking to the pre-mode cleaner cavity using the PDH technique. The amplitude-modulated beat signal is generated in the reflection of the cavity when it is locked to one of the 25 MHz sidebands. The bbPD1 is the photodiode sensor used for PDH locking. The bbPD2 is used in calibration and measures the power modulation index of the beam incident on the camera. The total power incident on the camera is attenuated to $\sim 10~\mu$W [1].

$$R(\omega) = \frac{E_{ref}}{E_{in}} = \left[\frac{-r_1 + r_2 r_3 e^{i\varphi}}{1 - r_1 r_2 r_3 e^{i\varphi}} \right], \tag{4.9}$$

where $r_{1,2,3}$ are the reflection coefficients of the mirrors and φ is the round trip phase accumulation. φ is given by $3\omega/\Delta\nu_{fsr}$ where ω is the carrier frequency and $\Delta\nu_{fsr}$ is the cavity free spectral range. To produce a significant amount of amplitude beat signal between carrier and sideband, the PMC cavity length was tuned to resonate on a single sideband. Under the simplifying assumption that one sideband passes the PMC 100%, while the other light gets reflected 100%, the reflected field becomes to first order

$$E_{ref} \approx E_c \left(R(\omega) + R(\omega - \Omega) \frac{i\Gamma}{2} e^{-i\Omega t} \right), \tag{4.10}$$

which is then passed through a 50/50 beam splitter where half of the laser light is reflected onto a single-element broadband rf phototdiode (bbPD1) for PDH locking and the other half is directed to the camera. From here, the beam power is split again

with 90% of the light going to the camera and 10% incident on a second photodiode (bbPD2) used for calibration – discussed more in Section 4.3.2. The power incident on the camera is thus amplitude modulated with amplitude modulation index Γ:

$$
\begin{aligned}
I_{PC} &= |E_{ref}|^2 \\
&= |E_c|^2 \left[R(\omega) + iR(\omega - \Omega) \left(\frac{\Gamma}{2} e^{-i\Omega t} \right) \right] \left[R(\omega) + iR(\omega - \Omega) \left(\frac{\Gamma}{2} e^{-i\Omega t} \right) \right]^* \quad (4.11) \\
&= |E_c|^2 \left(|R(\omega)|^2 + \frac{\Gamma^2}{4} |R(\omega - \Omega)|^2 - iR(\omega)R(\omega - \Omega) \left[i\Gamma sin\Omega t \right] \right) \quad (4.12) \\
&\approx |\tilde{E}_c|^2 \left(1 + \frac{R(\omega - \Omega)}{R(\omega)} \Gamma sin\Omega t \right) \quad (4.13)
\end{aligned}
$$

The sideband contributes a negligible amount of DC power since the beam in reflection is entirely dominated by carrier light; therefore, we only consider the power in the carrier in DC. We denote the frequency-dependent carrier field amplitude by

$$
\tilde{E}_c = R(\omega) \ E_c. \quad (4.14)
$$

The amplitude modulated optical signal directed onto the camera generates proportional photocurrent i_{PC} which is related to Equation 4.11 by the quantum efficiency η such that

$$
i_{PC} \approx \eta \ I_{PC}. \quad (4.15)
$$

During demodulation, the photocurrent is integrated for a time T, and subsequently converted into a voltage. Frequency terms greater than the modulation frequency are filtered by the bandwidth of the camera. We express the demodulation as a linear combination of the in phase and quadrature phase signals by taking the product of the incident photocurrent and the reference signal $cos(\Omega t)$ and evaluating at the respective demodulation phases ($\theta_m = 0, 90, 180, 270$)

$$V_{PC} = \frac{g_{PC}}{T} \int_{-T/2}^{T/2} i_{PC} \, cos(\Omega t + \theta_m) \, dt \tag{4.16}$$

$$= \frac{g_{PC}}{T} \left[\int_{-T/2}^{T/2} i_{PC} \, cos(\Omega t) cos(\theta_m) \, dt - \int_{-T/2}^{T/2} i_{PC} \, sin(\Omega t) sin(\theta_m) \, dt \right] \tag{4.17}$$

$$= g_{PC} \left(\Re[i_{PC}] cos\theta_m - \Im[i_{PC}] sin\theta_m \right) \tag{4.18}$$

$$= g_{PC}\eta \left(\Im \left[\Gamma |\tilde{E}_c|^2 \frac{R(\omega - \Omega)}{R(\omega)} \right] sin\theta_m \right), \tag{4.19}$$

where $g_{PC}(V/e-)$ is the gain of the ADC. Here we see that the demodulated output extracts the real and imaginary components of the signal. Since the upper sideband is allowed to transmit through the triangular cavity, only the lower sideband is measured in reflection. This is observed as the demodulated output being purely imaginary. The phase and amplitude can be found by substituting the results of Equation 4.16 into Equations 3.10 and 3.11. In this single-sideband scenario power modulation index Γ is also related to the sideband-to-carrier ratio SCR via

$$\text{SCR} \, [\text{dBc}] = 20 \log_{10} \left(\frac{\Gamma}{2} \right), \tag{4.20}$$

where we use the IEEE's definition [71]. Unlike typical photodetectors, the measured photocurrent is demodulated at Ω in each pixel on the sensor array. The corresponding amplitude and phase maps are then constructed using the measured values of I and Q for each frame. The CMOS phase camera in our experiment was set to capture at a frame rate of 7 Hz with total exposure time of 32 ms, although frame rates of up to 60 Hz are supported by the camera. Additional capture settings for our measurements are referenced in Table ??. The lowest achievable demodulation frequency for our current electronics setup is 5 MHz. This is primarily due to the RF switch bandwidth. This limitation is improved with the use of the CD54ACT109 flip-flop, which allows for synchronized demodulation output down to kilohertz frequencies. The AC integration time is internally set to never exceed 30% of the DC integration time[3], this allows for sufficient readout and dead time after frame readout.
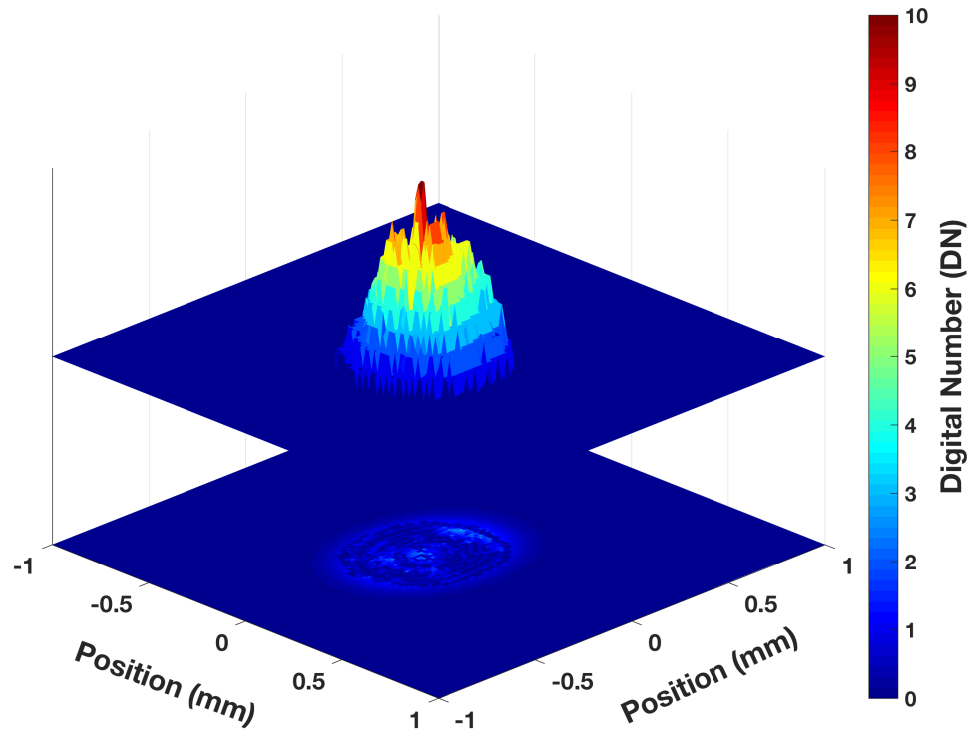
Figure 38: The DC intensity profile, which is used in calibration, is plotted as a function of sensor position. The residual of the Gaussian fit to the DC profile is shown in the plane on the bottom. The dominant 4-bit digitization noise in the DC output is noticeable. In contrast, the RF output is digitized with 12-bit resolution [1].

4.3.2 Calibration Methods

For each frame of the 320×240-pixel array, the respective amplitude, phase, and ambient readout channels of the camera are expressed in terms of counts of the analog-to-digital converter or digital numbers (DN). We perform a calibration procedure to extract a calibration factor, κ, which relates the total number of generated photoelectrons in an image to the corresponding DN value. The calibration procedure is as follows:

1. We use the broadband photodiode (bbPD2, see Fig. 37), to obtain a calibrated measurement of the modulation index of the beam incident on the camera. We measured its DC transimpedance Z_{dc} to be 1975 Ω and its RF transimpedance Z_{rf} at 25 MHz, the frequency of the local oscillator, to be 4750 Ω. Then, the power modulation index (Γ_m) of an arbitrary beam incident on *bbPD2* can be calculated via

$$\Gamma_m = \frac{1}{2} \cdot \frac{V_{pp}^{rf} \cdot Z_{dc}}{Z_{rf} \cdot V_{dc}}, \tag{4.21}$$

where the peak-to-peak RF signal (V_{pp}^{rf}) and the mean DC signal (V_{dc}) measured by *bbPD2* are read on an oscilloscope. The factor of $1/2$ is used to convert peak-to-peak voltage to amplitude. Using Ohm's law, we can solve for Γ_m in terms of the photoelectron flux for both the DC and AC signal.

$$\Gamma_m = \frac{1}{2} \cdot \frac{I_{pp}^{rf}}{I_{dc}} \tag{4.22}$$

$$= \frac{1}{2} \cdot \frac{qN_{rf}/t_{rf}}{qN_{dc}/t_{dc}} \tag{4.23}$$

$$= \frac{1}{2} \cdot \frac{n_{ac}}{n_{dc}} = \frac{1}{2}\Gamma \tag{4.24}$$

In Equation 4.22, q is the charge of an electron and both N_{rf}/N_{dc} describe the total number of charge carriers over the respective integration times t_{rf}/t_{dc}. The double-sideband modulation index is given by Γ. Now that we have established a relationship between the DC and AC signal, we can use this to determine the relationship between the calibration values.

---

[3]The DC integration time makes up about 3/4ths of the frame initialization trigger and the rest is a dead period which includes frame readout and processing of DC frames

2. To quantify the number of photons incident on the camera we measure the incident power (P_{in}) using a calibrated Thorlabs power meter. Since the NIR filter on the camera has a 5% transmission at 1064 nm at normal incidence [61], the total power incident on the camera after the filter (P_{in}^{sensor}) can be calculated. The range of DC power up to saturation is provided in Table **??** for a beam size of 0.25 mm used in this measurement. The DC power per pixel can then be calculated by dividing the measured intensity profile I(x,y) by the pixel area A_{pix}, refer to Table **??**. We find that that the minimum DC power detectable in each pixel from a Gaussian beam is of the order of a few nW and the maximum power of each pixel at saturation is ≈ 14.6nW. Using the ambient channel of the camera, we can measure the profile of the incident beam. We fit a Gaussian profile normalized to the P_{in}^{sensor} to get the Gaussian beam parameters and calculate the power density of the beam incident on the sensor, $p_{in}^{sensor}(x, y)$, see Fig. 38. The number of photons per area incident on the sensor during the exposure time T_{exp} can then be estimated by

$$n_p(x, y) = \frac{p_{in}^{sensor}(x, y) \cdot T_{exp}}{h\nu} \qquad (4.25)$$

The exposure time is the sum of each of the quadrature exposure time during which the signal is integrated.

3. The number of photoelectrons generated in each pixel is related to the number of photons via the quantum efficiency η, which for the OPT8241 sensor is approximately 2% for 1064 nm light [58]. Thus we have

$$N_e = \int_{A_{pixel}} n_e(x, y) \, dxdy = \int_{A_{pixel}} \eta \cdot n_p(x, y) \, dxdy \qquad (4.26)$$

4. Finally, the calibration factor κ is given by the ratio of the total number of photoelectrons generated to the sum of digital numbers reported in a region of interest (ROI):

$$\kappa_{DC}(e^-/DN) = \frac{\Sigma_{ROI}(N_e)}{\Sigma_{ROI}(DN_{DC})} \qquad (4.27)$$

Similarly, the AC calibration is given by

$$\kappa_{AC}(e^-/DN) = \Gamma_m \frac{\Sigma_{ROI}(N_e)}{\Sigma_{ROI}(DN_{AC})}, \qquad (4.28)$$

where Γ_m is the modulation index from Eq. 4.21 and we divide by the camera output in the AC readout, DN_{AC}. We estimate a calibration factor of κ_{DC} of $1.9 \cdot 10^5 \ e^-/DN$ and κ_{AC} of $1.0 \cdot 10^3 \ e^-/DN$.

4.3.3 Quantitative Noise Analysis

Here we quantify the temporal and spatial noise of the CMOS phase camera. The noise performance is characterized using the experimental layout described in Section 4.3.1. To characterize the DC power saturation levels, we vary the intensity of the 1064 nm laser beam incident on the CMOS sensor. We observe pixel saturation at 6μW of incident power with beam radius of 0.25 mm. Additional camera performance parameters are summarized in Table 10.

To determine the RF sensing capabilities and noise limitations of the phase camera the DC intensity of the beam incident on the sensor is held constant while the power modulation index is varied by sweeping the cavity, as illustrated in Fig. 37. Using this method, we report performance measurements for power modulation index values from zero to 0.046. The AC calibration factor, calculated in Section refsec:calibration, is used to convert the measured noise into equivalent number of photoelectrons. The total noise in an individual pixel in a single frame is estimated by adding in quadrature photon shot noise, fixed pattern noise, and electronics noise, all of which are measured with an integration time of 32 ms. The total amplitude and phase noise are measured as the standard deviation of the corresponding image obtained by subtracting two independent illuminated frames and dividing the result by $\sqrt{2}$[4]. The result in Fig. 39 show a close agreement between measured and estimated noise. We find that the shot noise limit is a factor of 8 below the total measured noise and the camera sensitivity is limited by background electronic noise and fixed pattern noise.

The demodulation pixels suppress the DC contribution of the illuminating beam using correlated balance sampling [58, 56]. However, a sufficiently high carrier field intensity will saturate the pixel of the sensor. The dynamic range is the ratio of the saturation point to the noise floor defined as [58]

$$D/R = 20 \log_{10}\left(\frac{A_{sat}}{\sigma_{dark}}\right), \tag{4.29}$$

---

[4]The details of this calculation are provided in Appendix D.
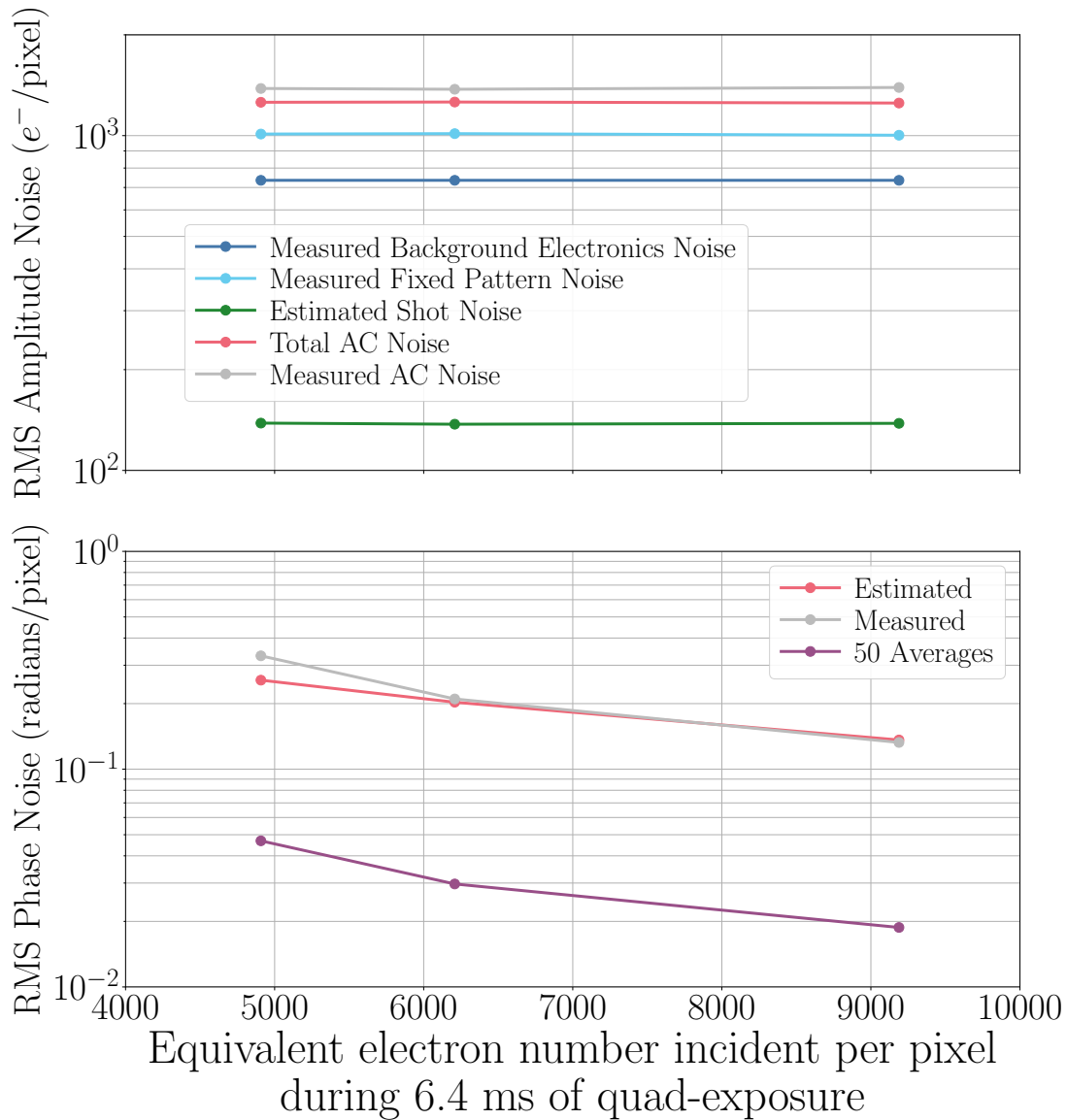
Figure 39: The figure above shows the phase camera noise as the power modulation index of the incident beam is varied at constant beam intensity. The root-mean-square amplitude noise (top) and phase noise (bottom) per pixel of the camera are calculated from a single image captured (no averaging). As the beam profile is the same across these measurements, the sensor area considered is the same. The shot noise and fixed pattern noise remain constant under these illumination conditions. We find that the total measured per pixel noise in phase and amplitude agrees closely with the sum of the budgeted noise sources. The current prototype of the phase camera is predominantly limited by the electronic noise and the shot noise is a factor of 8 below the total noise. The phase noise improves with higher power modulation index and with averaging of frames. The bottom plot also shows the measured per pixel phase noise with 50 frame averages in purple [1].

where A_{sat} is the pixel saturation value, i.e. maximum digital number and σ_{dark} is the dark noise of the pixels. We estimate an operating dynamic range of 75 dB for the phase camera. However, due to the low modulation index of the illuminating beam in our test setup, the camera saturates in DC before reaching the full dynamic range of the amplitude and the phase readouts.

4.3.4   Sensitivity to Power Modulation Index

Camera performance for each measurement can also be quantified by calculating the signal-to-noise ratio (SNR). We define the SNR as the ratio of the demodulated amplitude A (estimated using spatial averaging) to the measured amplitude noise σ_A.

$$SNR = \frac{A}{\sigma_A} \approx \frac{<N_{AC}>}{\sigma_{AC}} \tag{4.30}$$

As shown in Equation 4.30, SNR can also be expressed as the ratio of the modulated number of photoelectrons incident on the camera to the measured amplitude noise. Using this standard, we can define a measurement criteria for evaluating significant detection of power modulation index as having an SNR equal to or above the "σ_0" level.

$$SNR = \frac{<N_{AC}>}{\sigma_{AC}} \geq \sigma_0 \tag{4.31}$$

Substituting the results from Equations 3.30 and 4.22 into Equation 4.31, we see that

$$\frac{n_{AC}t_{AC}}{2\sigma_{AC}} \geq \sigma_0 \tag{4.32}$$

$$\Gamma\frac{n_{DC}t_{AC}}{2\sigma_{AC}} \geq \sigma_0 \tag{4.33}$$

rearranging,

$$\Gamma \geq \sigma_0 \frac{2\sigma_{AC}}{n_{DC}t_{AC}} \tag{4.34}$$

We define Equation 4.34 as the detectability of a modulation index, where the expression to the right side of the inequality sets the threshold for significant detection. In the case that the camera is shot noise limited, we can substitute the result from

Equation 3.39 into the expression on the right of the inequality. Therefore, in the double-sideband case we get,

$$\Gamma \geq \frac{4\sigma_0}{\sigma_{AC}} \tag{4.35}$$

and for a single sideband,

$$\Gamma_m \geq \frac{2\sigma_0}{\sigma_{AC}} = \frac{2\sigma_0}{\sqrt{2n_{DC}t_{AC}}}. \tag{4.36}$$

Since frames and pixels are independent and equally-distributed, averaging can be used to improve the signal-to-noise ratio. It is well-known that the signal-to-noise improves as the square root of the averaged frames $\sqrt{N_{frame}}$ and, similarly for pixels, $\sqrt{N_{pix}}$. Calculations showing how signal-to-noise improves with averaging is shown in Appendix C. Because image frames and pixels can be averaged independently, both contribute a factor of square root of number of averages to the measured noise.

$$\Gamma_m \geq \frac{2\sigma_0}{\sqrt{N_{frames}\ N_{pix} \cdot 2n_{DC}t_{AC}}} \tag{4.37}$$

We define the SNR for individual pixels on a single frame, as well as after spatial and/or temporal averaging. We observe that for averaging up to 50 independent frames, the SNR improves as $\sqrt{N_{frame}}$, Fig. 40. The figure shows the SNR as a function of the power modulation index Γ_m for up to 50 averaged frames. The y-axis is scaled by $1/\sqrt{N_{\text{frames}}}$, such that the data points line up if the noise in the frames are independent. We find the SNR scales linearly with the modulation index of the illuminating beam at constant beam intensity. By fitting a linear model to the data, we find that our camera is capable of detecting a modulation depth of 0.0063 with a significance of greater than σ. The fit also shows for 50 frame averages that the phase camera can detect signals above a modulation index of 0.0009 without any spatial averaging, see Fig. 40.

Using equation 4.20 and substituting the power modulation index of 0.0063 (SNR = 1), we can also find the camera's sensitivity limit for resolving the sideband-to-carrier ratio SCR in dBc per frame per pixel:

$$\text{SCR}_{\text{LIM}} = 20\log_{10}\left(\frac{\Gamma_{\text{SNR}=1}^{\text{1fr,1pix}}}{2}\right) = -50\,\text{dBc}_{/\text{fr}/\text{pix}}. \tag{4.38}$$
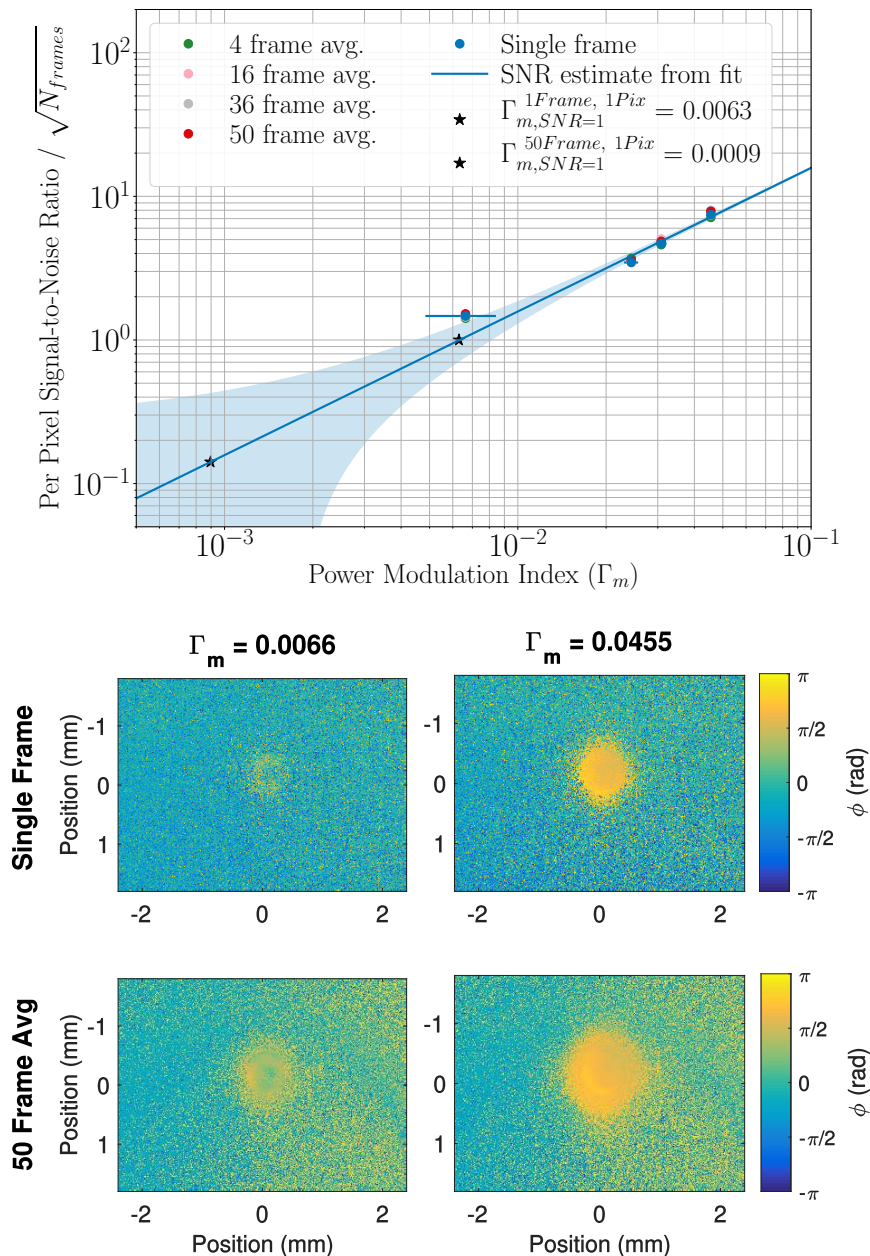
Figure 40: Top plot: Single-frame-SNR as a function of Γ_m. The y-axis shows the single-frame-SNR, defined as $\mathrm{SNR}/\sqrt{N_{frames}}$. The horizontal error bars show the experimental errors in the estimation of the Γ_m using the calibrated *bbPD2* photo detector. We find the SNR improves with the square root of the number of frames and number of pixels, consistent with temporally and spatially independent pixel noise. Pixel averaging can be implemented to improve the SNR at the cost of spatial resolution. The blue line represents a linear fit through the data. Using the fit, we estimate with 50 averages, the CMOS phase camera is capable of sensing RF signals in each pixel with Γ_m as low as 0.0009. Bottom figures: Phase images – single frame (top row) and with 50 averages (bottom row), for incident beams with low (left) and high (right) power modulation index. The phase resolution improves linearly with SNR [1].

Since the frame rate for the test data was 7 Hz, and we only used about 50% of the maximum quad integration time per frame (see Table 9) we find approximately

$$\mathrm{SCR_{LIM}} = -62\,\mathrm{dBc}_{/\mathrm{sec}/\mathrm{pix}}.\tag{4.39}$$

	CAPTURE SETTINGS			
Camera Parameters	Minimum	Typical	Maximum	Comments
Frame Rate (fps)	-	7	60 (150)	Performance characterization was done at 7 fps. We tested the camera up to 60 fps (live-streaming limit). The camera supports up to 150 fps.
Quads	4	4	6	Four quad readout is measured with $\pi/2$ phase-stepped demodulation; Six quad readout is measured with $\pi/3$ phase-stepped demodulation.
Sub-frames	1	1	4	The camera allows the capture of 1-4 sub-frames to construct a single frame. Each sub-frame is constructed with the readout of all the quads above.
Quad Integration time (ms)	1% DC_{Exp}	6.4 (15%)	30% DC_{Exp}	Dependent on the frame rate, number of sub-quads and sub-frame and the readout time. The quad integration time cannot exceed 30% of the DC exposure due to the readout and dead time of the CMOS phase camera.
Pixel Resolution (μm)		15		This defines the average size of each pixel on the sensor array.
Sensing Area (mm)		4.8×3.6		The total sensing area of the CMOS sensor.

Table 9: The table summarizes the range of camera capture settings [1].

ILLUMINATION CHARACTERISTICS				
DC Power (nW) [per pixel], estimated with beam size $w_0 = 0.25$ mm	1.5	-	14.6	The minimum input power for the pixels to sense the input beam and the maximum power before the pixels saturate.
DC Power (μW) [sensor; for incident beam of size $w_0 = 0.25$ mm]	0.6	-	6.4	As the spot size of the incident beam increases, both the minimum and maximum DC power can be re-scaled in accordance with per pixel DC power limits above. We caution that this parameter is exposure time dependent.
Demodulation Frequency (MHz)	5	25	100	The performance characterization was done at 25 MHz. The camera supports demodulation frequency up to 100 MHz. The 5 MHz lower limit is due to the RF switch.

Table 10: The table summarizes the absolute rating for the illumination signals [1].

Frame Characterization (at 7 Hz frame rate and 15% quad integration time)				
Dynamic Range (dB)			75	The dynamic range of the camera as estimated from the dark noise level of the camera.
Γ_m: Single Frame	$6.3^{+2.2}_{-2.2} \cdot 10^{-3}$	-	1	The CMOS phase camera can typically sense as low as 0.0063.
SCR: Single frame	-50^{+3}_{-3} dBc/pixel	-	0 dBc/pixel	SCR down to -50 dBc/pixel can be resolved in a single frame.
Γ_m: 50 frames averaged	$0.9^{+0.3}_{-0.3} \cdot 10^{-3}$	-	1	With 50 frames averaged, the camera can sense incident RF beams as low as 0.0009.
SCR: 50 frames averaged	-67^{+3}_{-3} dBc/pixel	-	0 dBc/pixel	With 50 frames averaged we can resolve SCR down to -67 dBc/pixel.
Mean AC Noise (e^-)			10^3	

Table 11: The table summarizes the noise levels and sensitivity of the captured frames [1].

Chapter 5

Application to LIGO: Signal Modeling for Point Absorbers on CMOS phase camera

Note that the information presented in this chapter (i.e. figures and calculations) are taken from Muniz et al. (2021). Details involving point absorber calculations are presented in Appendix E for reference.

5.1   Signal Modeling for Point Absorbers

One of the critical issues limiting the sensitivity of Advanced LIGO is the presence of small (few tens of μm diameter) absorptive defects on the test masses, referred to as *point absorbers*. Exposed to the laser field in the interferometer arms, these test mass defects cause local heating and result in local optical path length distortions for the laser field. These optical distortions excite higher-order modes in LIGO's coupled cavities, leading to excess optical loss and limiting the sensitivity of the detectors. Furthermore, the path distortions affect the carrier and sideband phase fronts differently, thus deteriorating the alignment and angular control error signals. A phase camera is capable of mapping these phase front distortions. Error signals can be extracted from the camera output and can be used to control corrective actuators. Unlike conventional quadrant photodiodes, the phase cameras offer a high spatial resolution to resolve the phase front changes due to the point absorbers.
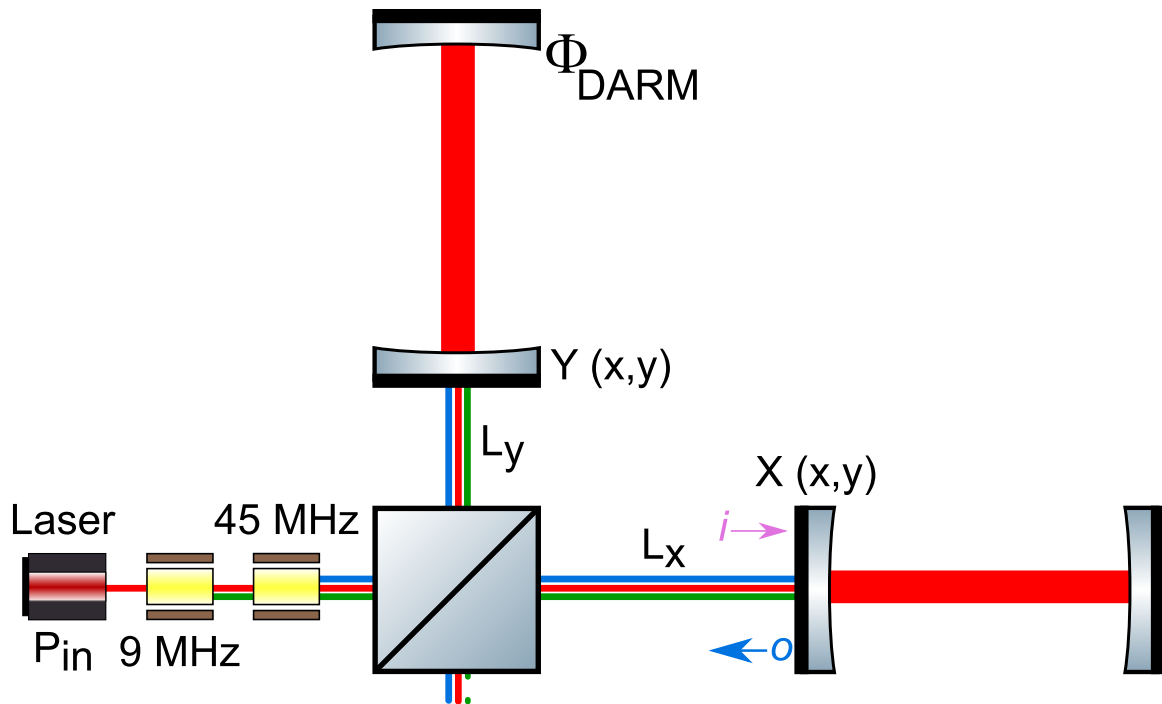
Figure 41: The simplified Advanced LIGO setup for point absorber modeling. To simplify the simulation we do not include the effects of the power and the signal recycling cavities. Instead, we model the input power to be equal to the power at the beamsplitter during the Advanced LIGO O3 run [2]. The other parameters of the interferometer are summarized in the table 12. The optical path distortions due to the point absorbers is modeled with a Lorentzian profile for each of the input test masses. The carrier and the sideband fields are calculated under plane beam/paraxial approximation and the corresponding beat signals are calculated at the anti-symmetric port of the beamsplitter [1].

Simulation Parameters	
Differential arm offset	10 pm
Arm cavity finesse	446
P_{Homodyne} ref. Beam	50 mW
$P_{\text{in}}^{\text{BS}}$	1500 W
w_0^{BS}	6 cm
L_{Schnupp}	8 cm
Carrier recycling gain	40
45 MHz recycling gain	2
45 MHz phase mod. index	
at input	0.18
at beamsplitter	0.04

Table 12: Simulation Parameters of the interferometer shown in Fig. 41. They approximately correspond to the Advanced LIGO parameters [2].

To get an approximate estimate of the phase camera's ability to sense the effect of point absorbers LIGO's input test masses, we present a simplified model without considering the coupled cavity layout of LIGO, shown in Fig. 41. We initially also ignore Gouy phase shifts because beamsplitter and input test masses are essentially in the same Gouy phase. We will get back to the effect of the output beam Gouy phase shift. While these are oversimplifications, they still allow us the estimate the required sensitivity to pick up the point absorber phase distortions in a phase camera image taken at the interferometer anti-symmetric port. We consider two scenarios, the current Advanced LIGO, which uses DC readout, and the A+ upgrade, which uses homodyne readout without differential arm DC offset. We choose the model parameters in accordance with the existing Advanced LIGO facilities. We assume the carrier and the 9 MHz and 45 MHz sidebands (with modulation index Γ) are incident at the 50/50 beamsplitter. Considering the approximate power-recycling gain of 40 for the carrier and 2 for the 45MHz sidebands we can estimate the power modulation index of the beam incident on the beamsplitter [2, 40]. The beam then propagates from the beamsplitter to the input test mass in each of the arm cavities.

We model the response of the point absorbers to first-order, which affects the phase of the sidebands, but leaves the carrier unperturbed. The carrier experiences only a phase shift due to the DARM offset between the two arm cavities:

$$r_x^{car} = +1 \cdot e^{i\Phi_{DARM}/2} \qquad\qquad r_y^{car} = +1 \cdot e^{-i\Phi_{DARM}/2} \tag{5.1}$$

$$r_x^{sb} = -1 \cdot e^{i2k\mathrm{X}(\vec{x},\vec{y})} \qquad\qquad r_y^{sb} = -1 \cdot e^{i2k\mathrm{Y}(\vec{x},\vec{y})} \tag{5.2}$$

where $\mathrm{X}(\vec{x},\vec{y})$ and $\mathrm{Y}(\vec{x},\vec{y})$ are the one-way transmission maps encoding the optical path distortions. Under these simplified assumptions one can calculate the fields of the carrier and sidebands at the anti-symmetric port of the beamsplitter. The beat map between the carrier or the reference beam with the sideband in $\mathcal{I}$ and $\mathcal{Q}$ is given by

$$\mathcal{I}(x,y) = \mathbb{R}e(sb_+^* c + c^* sb_-) \tag{5.3}$$

$$\mathcal{Q}(x,y) = \mathbb{I}m(sb_+^* c + c^* sb_-) \tag{5.4}$$

One can analytically show that in the Gouy phase of the beamsplitter ($\phi = 0$) the beat in $\mathcal{I}(x,y)$ and $\mathcal{Q}(x,y)$ between the carrier and the sidebands at the AS port is first-order independent of the optical path distortions due to the point absorber. We recover the usual DC readout terms:

$$\mathcal{I}(\vec{x},\vec{y}) = 0 \tag{5.5}$$

$$-\mathcal{Q}(\vec{x},\vec{y}) = \Gamma p_{in}(\vec{x},\vec{y}) \sin(\frac{\Phi_{DC}}{2}) \sin(\frac{\omega_s L_s}{c}) \tag{5.6}$$

However, this does not remain true at every Gouy phase in the readout beam. The small point absorber distortion evolves differently with Gouy phase. For simplicity, we can assume that the distortion fields $\mathrm{X}(\vec{x},\vec{y})$ and $\mathrm{Y}(\vec{x},\vec{y})$ contains only one higher-order mode of order $N = l + m$. (l and k are for example the Hermite-Gauss mode orders.) Then the $\mathcal{I}$ readout quadrature become

$$\mathcal{I}^\phi = k\Gamma p_{in} \sin(\frac{\Phi_{DC}}{2}) \cos(\frac{\omega_s L_s}{c}) \sin(N\phi)(\mathrm{X} - \mathrm{Y}) \tag{5.7}$$

where the spatial shape is given by the beat of the fundamental and the N-th order mode, $\Psi_N(\vec{x},\vec{y}) \cdot \Psi_0(\vec{x},\vec{y})$. Equation 5.7 can be generalized by expanding $\mathrm{X}(\vec{x},\vec{y})$ and $\mathrm{Y}(\vec{x},\vec{y})$ in terms of higher order Gaussian modes, which is straight forward, a little
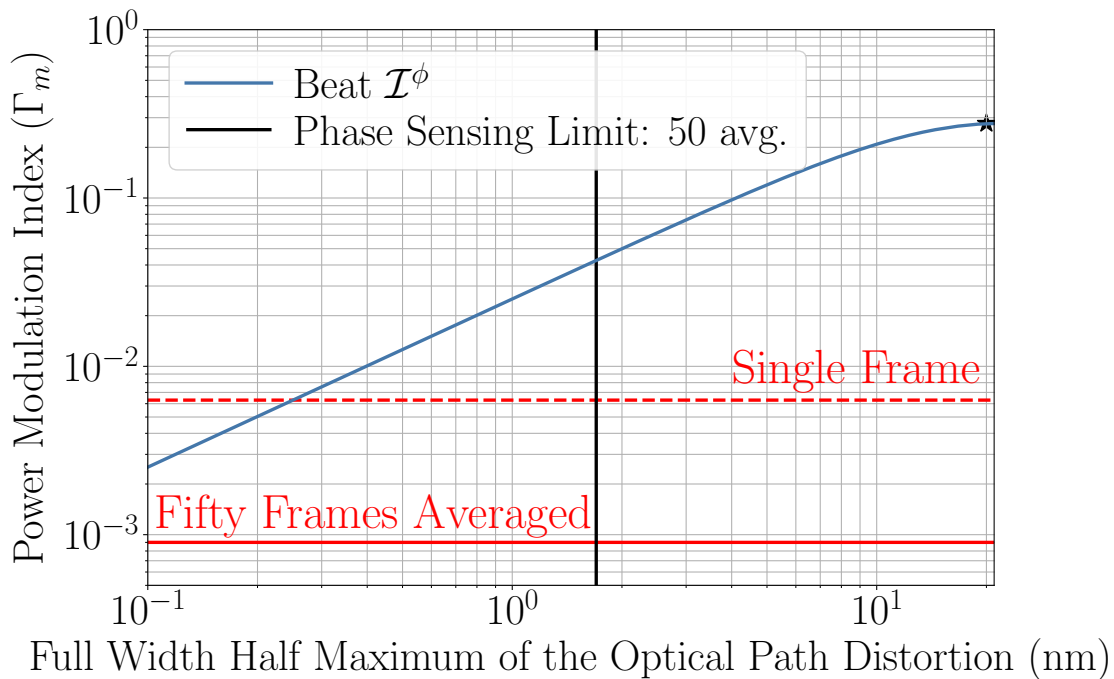
Figure 42: Size of the expected power modulation index in the interferometer anti-symmetric port $\mathcal{I}$-quadrature, as a function of the optical path distortions (OPD) due to a point absorber on an input test mass. The power modulation index scales linearly with the OPD before it plateaus to a constant, which is caused due to the sidebands, 9 MHz and 45 MHz, leaking through the AS port. The dashed red line shows the minimum power modulation index that the CMOS phase camera can sense using only a single frame. The solid red line shows the minimum power modulation index that the CMOS phase camera can sense after 50 averaged frames. In homodyne readout, where there is no large orthogonal $\mathcal{Q}$-quadrature signal to compete with, we can sense distortions greater than 0.1 nm using 50 averaged frame. In the current DC readout there is a large $\mathcal{Q}$-quadrature signal due to the differential arm DC offset. The phase resolution of the CMOS phase camera will thus limit sensing capabilities. The solid black line represents the per pixel phase resolution limit after 50 frame averages (see Fig. 39). Assume the camera is place in the appropriate Gouy phase, we can resolve optical path distortions greater than 2 nm in the DC readout scheme of current Advanced LIGO detectors. Typical optical path distortions due to these point absorbers in Advanced LIGO ranges from few nanometers to a few hundreds of nanometer [6, 2]. The parameters of the simulation are summarized in Table 12.

complicated, and not necessary if we are only interested in the camera sensitivity limitation.

The presence of a large beat signal in the $\mathcal{Q}$ quadrature from the DC readout scheme means that we also have to worry about the camera phase resolution. The beat map phase rotation is given by

$$\frac{\mathcal{I}}{\mathcal{Q}}^{\phi} = k \cot(\frac{\omega_s L_s}{c}) \sin(N\phi)(\mathrm{X} - \mathrm{Y}) \tag{5.8}$$

During the A+ upgrade Advanced LIGO will switch to a homodyne readout scheme, reducing the DC offset to zero, and instead using a separate carrier reference beam as local oscillator. We assume that the reference beam has about the same amplitude as the current carrier due to the DC offset, as this permits using the same sensing and readout electronics. Thus, the expression 5.7 for sensing the effect from the point absorbers remains essentially the same, with one difference: For diagnostic purposes we now have control over the phase α_{Hom} of the reference beam. The $\mathcal{I}$ quadrature thus becomes

$$\mathcal{I}^{\phi} = k\Gamma\sqrt{p_{ref}p_{in}} \cos(\frac{\omega_s L_s}{c}) \sin(N\phi - \alpha_{\mathrm{Hom}})(\mathrm{X} - \mathrm{Y}) \tag{5.9}$$

Thus we can pick the beamsplitter Gouy phase $\phi = 0$, a 90 deg rotated reference beam, $\alpha_{\mathrm{Hom}} = \pi/2$, removing the large beat signal in the $\mathcal{Q}$ quadrature and avoiding the phase resolution limitation of the phase camera.

The power modulation index of the beat signal is given by

$$\Gamma_{\mathcal{I}} = \frac{2\mathcal{I}}{DC}; \quad \Gamma_{\mathcal{Q}} = \frac{2\mathcal{Q}}{DC} \tag{5.10}$$

Figure Eq. 42 shows the size of the expected power modulation index signal as a function of the optical path distortion (OPD). The red horizontal dashed line represents the approximate power modulation index sensitivity limit of the phase camera for each pixel. The vertical black dashed lime corresponds to the phase resolution limit of the camera, and is relevant in the presence of a large signal in the orthogonal quadrature due to the interferometer differential arm fringe offset. We expect the phase camera to be sensitive enough to pickup optical path distortions greater than about $\sim 2\ nm$ where the readout is limited by phase resolution of the phase camera. Otherwise, the phase camera is capable of sensing OPD due to point absorbers as low as $\sim 0.1\ nm$. Typically, the OPD caused due to point absorbers ranges between tens

up to a few hundreds of nanometers [6, 2]. Currently Hartmann wavefront sensors are used to image point absorbers in aLIGO directly. These sensors map the point absorbers onto the surface of the test masses [6], but do not measure their impact on the interferometer. The CMOS phase camera does not directly image the point distortions, but instead measures the change in the interferometer phase front at the AS port caused due to these point defects. Using the model discussed above, we simulate an example case for a typical point absorber [6] with 20 nm of optical path distortion at full width half maximum, see Fig. 43.

5.1.1   Implications for Gravitational Wave Detectors

The simple interferometer model presented above leads us to conclude that the CMOS phase camera developed in our group is capable of diagnosing the effect of point absorbers on the LIGO input test masses when installed at the interferometer anti-symmetric port. The exact Gouy phase of the camera will matter though, as there is no signal in the beamsplitter Gouy phase. Having a separate local oscillator reference beam, either as part of the homodyne readout or as a separate local oscillator for the phase camera, will simplify the image analysis. Lastly, we note that the model presented above does not include the signal recycling cavity and the power recycling cavity of the Advanced LIGO detector. While the power recycling cavity only filters the beam incident on the beamsplitter, the signal recycling cavity will spatially filter the effect of the point absorber, cleaning up the mode. However, with a signal recycling mirror transmission around 32%, the signal recycling cavity has an extremely low finesse, preserving the distortion signal, but also making modeling rather complicated.
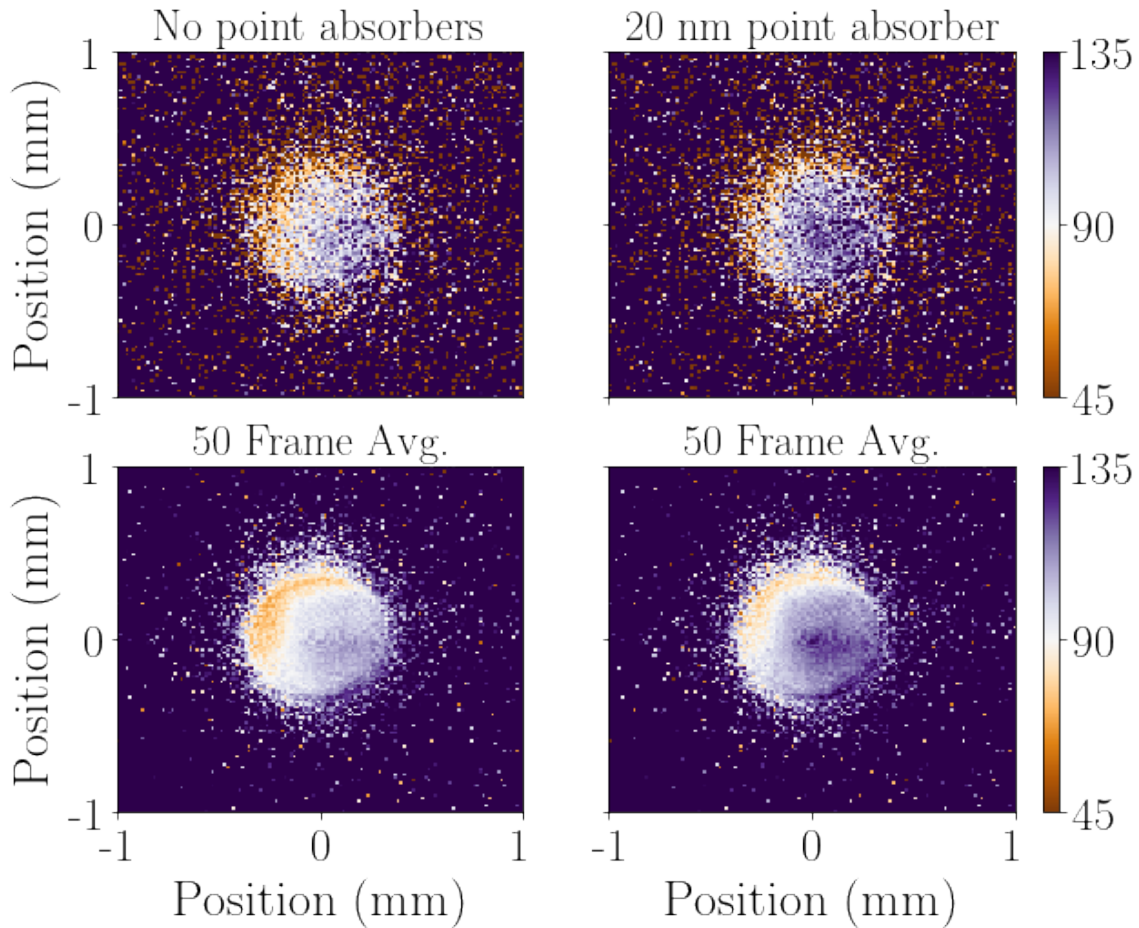
Figure 43: Simulated signal for a point absorber with 20 nm optical path distortion as seen at the anti-symmetric port (no recycling cavity, zero Guoy phase; see text). The 6 cm beam at the beamsplitter in our simulation, Fig 41, is rescaled to match the beam in our test setup (see Section 4.3.4), using the test images as reference for the point absorber free data including camera noise. The phase readout is not meaningful outside the illuminated region. The phase maps highlight the phase around $\pi/2\pm\pi/4$ to illustrate the phase distortions due to the point absorber. Top left: Reference test image for a single frame without any point absorbers. The non-Gaussian features arise from the distorted laser beam in reflection in the experimental setup. Top right: The relative phase distortion due to the point absorber is added to the test image for a single frame. Bottom left and bottom right: Same as top left and top right respectively, but with an average of 50 frames. We measure $\sim$28 degrees of accumulated phase in the presence of the 20 nm point absorber. This estimate is consistent with the analytical calculation in Section 5.1.

Chapter 6

Conclusions

6.1 Summary

At the time of writing, the LIGO detectors are currently preparing for the fourth observing run, O4. One of the primary objectives for LIGO in the next observing run is moving to higher input power, which will help to improve shot-noise limited sensitivity. In Chapter 2 I outlined some of the challenges with transitioning to higher power during the span of O2 and O3. In particular, the presence of point-absorbers on the test mass surfaces contributed to optical losses via distortion of the optical wavefront which scatter power out of the fundamental mode. This was determined to reduce the operational duty cycle of LIGO and lead to lock losses by disturbing the optical signals used for controlling alignment and mode matching in the interferometer. The current diagnostic methods used in the active wavefront sensing system of LIGO provided limited information about the higher order spatial modes that propagate in the interferometer due to these distortions. Therefore, the proposal is for next generation detectors to have sensors with multiple RF-sensitive segments (*pixels*) capable of distinguishing frequency-dependent spatial modes (i.e. a *phase camera*).

In Chapter 4, we demonstrate a CMOS phase camera that is capable of imaging externally modulated RF beat signals incident on the sensor with high spatial resolution. Despite being limited by fixed pattern noise, the noise levels of the camera allow sensing of RF beat signals with a power modulation index as low as 0.0009 with 50 frame averages. The phase camera also has the capability to measure the

beat signals at different frequencies and is sensitive to very low incident beam power levels. Lastly, the low latency image acquisition, design compactness, and relatively low cost of the phase camera make it suitable for numerous applications in wavefront diagnostics and sensing.

In Chapter 5, we model the behavior of a point absorber induced phase distortion on the beat signal at the AS port. Considering the sensitivity limits of the camera, due to the large beat signal in the $\mathcal{Q}$ quadrature, we determine that the phase camera is sensitive enough to resolve optical path distortions ~ 2 nm. Using a reference beam, as will be used in A+, we see that measurements of the optical path distortion as low as ~ 0.1 nm are achievable.

The primary application of a phase camera in gravitational wave detectors is for diagnostic purpose, imaging any unexpected phase front distortions, such as for example those induced by point absorbers on test masses (see section 5.1). However the phase camera can also be useful for controlling alignment and mode-matching in an interferometer. In particular, the 320×240 pixel resolution of the CMOS phase camera provides the sensing capabilities to operate and control interferometers with higher-order Laguerre-Gauss or Hermite-Gauss modes as the operating resonant mode, a scheme that was proposed to reduce the coupling of thermal noise to the gravitational readout [72, 73]. Additionally, it has been shown that these cameras can be operated synchronously [70], which allows for multiple cameras to simultaneously record the beam in separate Gouy phases.

In summary, we expect that the CMOS phase camera will be an excellent tool for commissioning Advanced LIGO, A+, and future gravitational wave detectors such as Cosmic Explorer [74] or Einstein Telescope [75], and might also have control applications.

6.2 Future Work

6.2.1 Integrated Design Solution

Currently, we are working on an integrated design chassis (see Figure 44) to house the electronic components mentioned in Section 4.2. The design features an all-in-one adapter board for the microcontroller, RF signal routing, and power supply. The idea for this enclosure is to provide a user-ready device for easy diagnostic measuring and
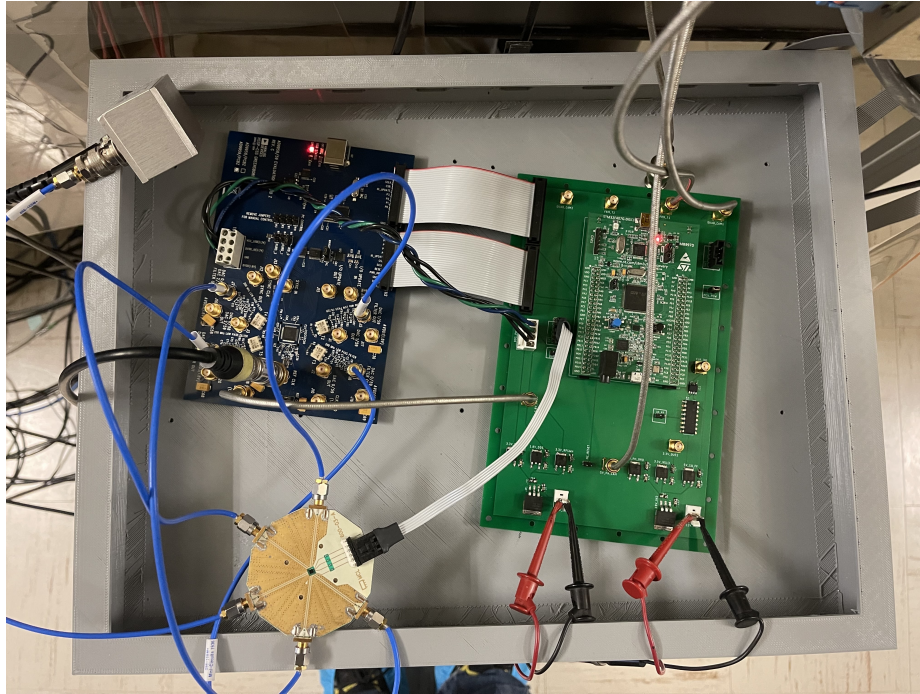
Figure 44: Custom-built enclosure unit.

testing at LHO.

6.2.2 Plan for O4 Commissioning

Initial discussions for how the phase camera will be used in A+ mainly revolve around developing a use case as a diagnostic tool. The first step of this plan involves modeling the phase camera response to distortions on the AS carrier field, due to the effects of point absorbers. In the simple case, this has been demonstrated in Chapter 5; however, a higher level analysis of the Gouy phase propagation in the arm cavities should also be considered.

Discussions on a specific use case for a phase camera mainly revolve around monitoring the mode matching into the filter cavity (FC) and OMC. A potential location for the CMOS phase camera would be somewhere in AS_AIR to monitor the 45 MHz sideband at the AS port; however, this remains an ongoing discussion.

Appendix A

Gaussian Beam Optics

To begin, we consider the propagation of an electromagnetic wave through an isotropic charge and current-free medium. In this case we can write Maxwell's equations as:

$$\nabla \times \mathbf{E} = -\frac{\partial \mathbf{B}}{\partial t}$$

$$\nabla \cdot \mathbf{E} = 0$$

$$\nabla \times \mathbf{B} = \mu_0 \varepsilon_0 \frac{\partial \mathbf{E}}{\partial t}$$

$$\nabla \cdot \mathbf{B} = 0$$

Considering only the spatial dependence of the wave, the scalar fields must satisfy the Helmoltz wave equation:

$$(\nabla^2 + k)E = 0, \tag{A.1}$$

where k $= \frac{2\pi}{\lambda}$ is the wave number. Here, we want to assume a solution to the Helmholtz equation that would best describe the propagation of our laser. The most trivial solution we can guess is plane wave; however, we must consider that the transverse profile of our laser changes as we propagate through space. Therefore, we can assume an *ansatz* solution of the form:

$$E(x, y, z) = \psi\ (x, y, z)e^{-ikz} \tag{A.2}$$

Equation A.2 describes the propagation of the monochromatic wave along the z-axis and describes the evolution of the wave front in the complex function $\psi\ (x, y, z)$. Plugging equation A.1 back into the Helmholtz equation, we get the reduced wave equation

$$\frac{\partial^2 \psi}{\partial x^2} + \frac{\partial^2 \psi}{\partial y^2} + \frac{\partial^2 \psi}{\partial z^2} - 2ik\frac{\partial \psi}{\partial z} = 0$$

The *paraxial* approximation assumes a change in the profile of the beam, but also that the beam does not diverge too far from the z-axis, or

$$\left|\frac{\partial^2 \psi}{\partial z^2}\right| \ll \left|2k\frac{\partial \psi}{\partial z}\right|,$$
$$\left|\frac{\partial^2 \psi}{\partial z^2}\right| \ll \left|\frac{\partial^2 \psi}{\partial x^2}\right|,$$
$$\left|\frac{\partial^2 \psi}{\partial z^2}\right| \ll \left|\frac{\partial^2 \psi}{\partial y^2}\right|.$$

Using the paraxial approximation, the Helmholtz wave equation reduces to the form

$$\left(\frac{\partial^2}{\partial x^2} + \frac{\partial^2}{\partial y^2} - 2ik\frac{\partial}{\partial z}\right) \psi\ (x, y, z) = 0$$

Equation A is also known as the paraxial wave equation and can also be represented in cylindrical coordinates as:

$$\left(\frac{\partial^2}{\partial r^2} + \frac{1}{r}\frac{\partial}{\partial r} - 2ik\frac{\partial}{\partial z}\right) \psi\ (r, z) = 0 \tag{A.3}$$

where we have dropped the angular dependence φ by considering the cylindrical symmetry of our beam about the z-axis.

A.1 Fundamental Beam Mode

In order to find a solution for the fundamental Gaussian mode, we must take into account the propagating beam will have the form of a Gaussian and that the Gaussian diverges slightly as it propagates along the z-axis. This effect is encapsulated by defining a parameter q(z). Additionally, we also would like to allow for additional phase,

which is accounted for by a P(z). Therefore, an *ansatz* solution of the fundamental Gaussian mode is [31]

$$\psi = \exp\left\{-i\left[P(z) + \frac{k}{2q(z)}\right]\right\} \tag{A.4}$$

where here we have defined ψ as representing the form of fundamental Gaussian mode. Substituting this solution into Equation A.3, gives

$$\left\{\left[\frac{k^2}{q^2(z)}\left(q'(z) - 1\right)\right]r^2 - 2k\left[P'(z) + \frac{i}{q(z)}\right]\right\}\psi = 0 \tag{A.5}$$

To be true for all r, each of the coefficients of r must be zero. Therefore, we get two first order differential equations in terms of q(z) and P(z)

$$\frac{dq(z)}{dz} = 1 \tag{A.6}$$

$$\frac{dP(z)}{dz} = -\frac{i}{q(z)}. \tag{A.7}$$

Solving Equation A.6, we arrive at an expression for our parameter q

$$q(z) = q_0 + z \tag{A.8}$$

The quantity q_0 is a constant of the integration, which, when taken to be complex returns the form of the Gaussian. This also represents our q parameter at the value $z = 0$. It is convenient to redefine q_0 in terms of the beam waist ω_0 and the wavelength λ as:

$$q_0 = i\frac{\pi\omega_0^2 n}{\lambda} = iz_0 \tag{A.9}$$

The complex parameter q_0 is re-expressed in terms of the Rayleigh range, z_0, or the distance where the mode area is effectively doubled. In Equation A.9 we also take n = 1. Now, solving Equation A.7 for P(z) we get

$$P(z) = -i\ln\left(1 + \frac{z}{q_0}\right)$$

substituting back into Equation A.4 gives

$$\psi = \exp\left\{-i\left[-i\ln\left(1 + \frac{z}{q_0}\right) + \frac{k}{2(q_0 + z)}r^2\right]\right\} \tag{A.10}$$
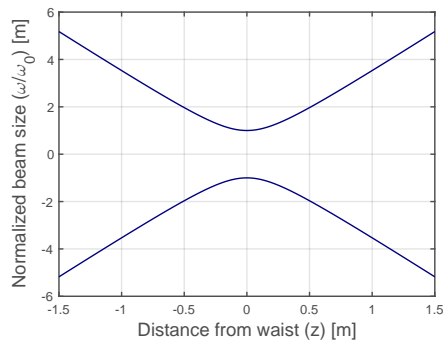
(a) Normalized Beam Size
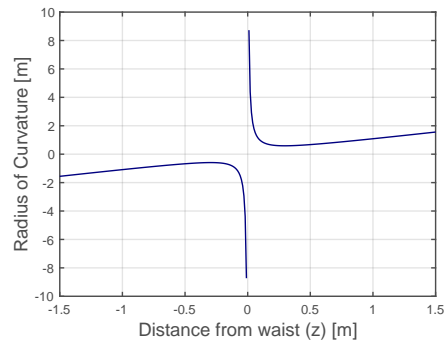
(b) Radius of Curvature
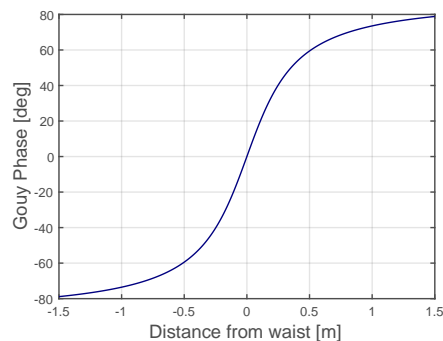
(c) Gouy Phase
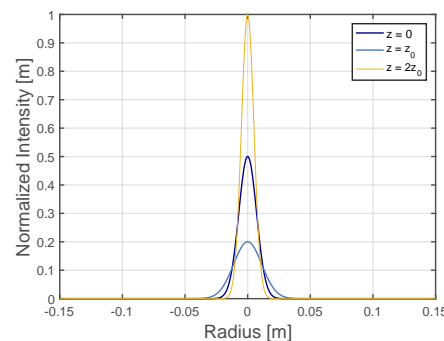
(d) Intensity

Figure 45: The plot above shows the Gaussian beam parameters evaluated for $\lambda = 1064$ nm and $\omega_0 = 1$ cm. (a) Beam size $\omega(z)$ as a function of distance from the waist. (b) Radius of curvature R(z) as a function of distance from the waist. (c) Gouy phase as a function of distance from the waist. (d) Normalized intensity as a function of beam radius.

it then follows that the beam size w(z) and radius of curvature R(z) can both be expressed as a function of the position of the beam along the propagation direction and in terms of z_0.

$$\omega^2(z) = \omega_0^2\left[1 + \left(\frac{\lambda z}{\pi \omega_0^2 n}\right)^2\right] = \omega_0^2\left(1 + \left(\frac{z}{z_0}\right)^2\right) \tag{A.11}$$

$$R(z) = z \left[1 + \left(\frac{\pi \omega_0^2 n}{\lambda z} \right)^2 \right] = z \left(1 + \left(\frac{z_0}{z} \right)^2 \right) \tag{A.12}$$

Notice that the beam size when z = 0 is simply the beam waist ω_0 and the radius of curvature goes to infinity as we would expect for a plane wave. At the Rayleigh range (z = z_0), the beam size is a factor of $\sqrt{2}$ larger than the waist size and the radius of curvature is double the Rayleigh range. We can also define an additional phase parameter, known as the Gouy phase $\zeta(z)$, which describes the phase accumulation of the Gaussian wavefront as it propagates

$$\zeta(z) = tan^{-1} \left(\frac{z}{z_0} \right) \tag{A.13}$$

Plots of the radius of curvature, beam size, and Gouy phase are shown in Fig. 45 for a beam of wavelength 1064 nm and a ω_0 = 1cm. Finally, substituting Equations A.10, A.11 and A.2 we finally arrive at the equation for the fundamental beam mode

$$E(r, z) = E_0 \frac{\omega_0}{\omega(z)} exp \left\{ -i[kz - \zeta(z)] - r^2 \left(\frac{1}{\omega^2(z)} + \frac{ik}{2R(z)} \right) \right\} \tag{A.14}$$

The intensity of the Gaussian beam is given by taking the square magnitude of Equation A.14

$$I(r, z) = |E(r, z)|^2 = I_0 \left[\frac{\omega_0}{\omega} \right]^2 \exp \left[\frac{-2r^2}{\omega^2(z)} \right], \tag{A.15}$$

where $I_0 = |E_0|^2$ and the peak intensity occurs when z = 0 and r = 0. The plot in Fig. 45d shows the intensity of a Gaussian beam plot for increasing distance from the waist, varying as a factor of the Rayleigh range. We can see from the plot that when the distance from the waist is equal to one Rayleigh range in length, the effective area of the beam is doubled, resulting in a decrease in intensity by a factor of 1/2.

A.2 Higher Order Modes

A.2.1 Hermite-Gauss Modes

If we relax the constraints of cylindrical symmetry, an infinite number of solutions to the paraxial wave can be found. These solutions are described as higher order modes
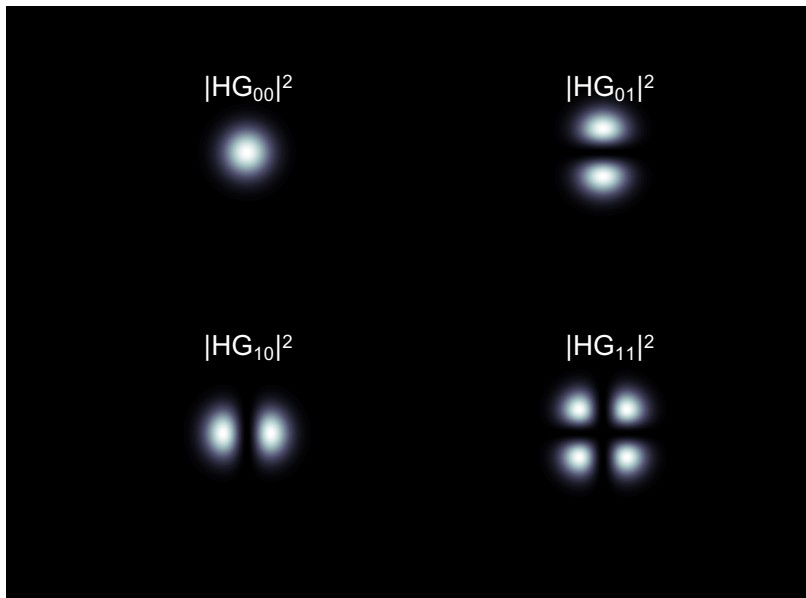
Figure 46: Intensity profiles of Hermite-Gauss modes for m = 0,1 and n = 0,1.

to the fundamental Gaussian mode. If we consider Cartesian symmetry, the solution for the paraxial wave equation is given by

$$HG(x, y, z)_{m,n} = E_0 \frac{\omega_0}{\omega(z)} H_m \left(\frac{\sqrt{2}x}{\omega(z)} \right) H_n \left(\frac{\sqrt{2}y}{\omega(z)} \right) \tag{A.16}$$
$$\cdot exp \left(i(m + n + 1)\zeta(z) - ikz - \frac{ik(x^2 + y^2)}{2R(z)} - \frac{x^2 + y^2}{\omega^2} \right),$$

where H(s) are the familiar Hermite polynomials $(1, 2s, 4s^2 - 2, 8s^3 - 12s, ...)$. The HG modes are illustrated in Figure 46 up to first order. Notice that if we set m = n = 0, we return to our original solution for the fundamental Gaussian beam. Additionally, since the HG modes form a complete and orthogonal basis set, we can decompose any solution of the paraxial wave equation into a linear combination of HG modes. The Cartesian symmetry of the HG basis is particularly useful in describing beam propagation as a result of misalignment in optical cavities due to translation or rotation. Another thing to consider is that the Gouy phase depends on the mode order by the term (m+n+1), where m is the horizontal index and n is the vertical index. This means that Gouy phase advances differently along the horizontal and vertical axis, which proves useful for general applications in wavefront sensing.
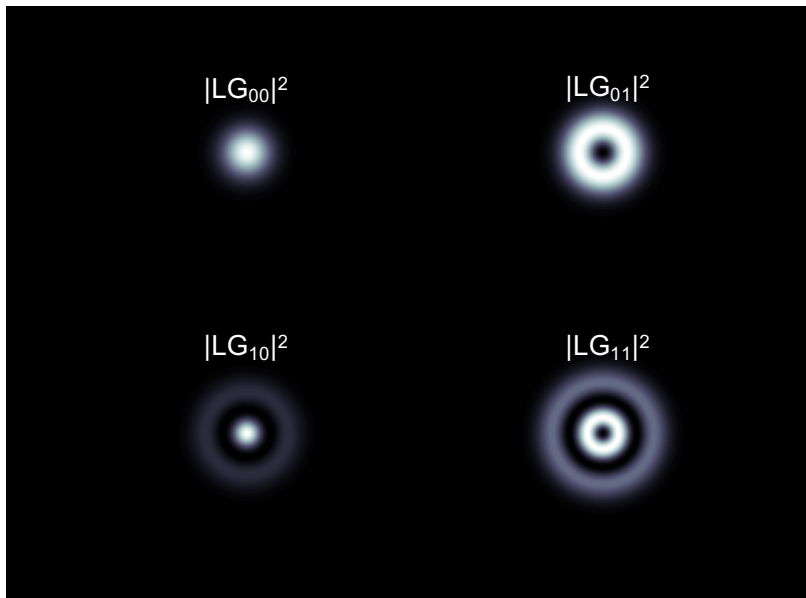
Figure 47: Intensity profiles of Laguerre-Gauss modes for p = 0,1 and l = 0,1.

A.2.2 Laguerre-Gauss Modes

Applying cylindrical symmetry, we get the Laguerre-Gauss (LG) Modes, which also form a complete and orthogonal set of solutions to the paraxial wave equation. The general form of the LG modes is given by:

$$LG(r, \phi, z)_{p,l} = E_0 \frac{\omega_0}{\omega(z)} \left(\frac{\sqrt{2}r}{\omega^2(z)} \right) L_p^l \left(\frac{2r^2}{\omega^2(z)} \right) \tag{A.17}$$
$$\cdot exp \left(i(2p + l + 1)\zeta(z) - ikz + il\phi - \frac{ikr^2}{2q(z)} \right),$$

where L_p^l are the Laguerre polynomials. The azimuthal index is represented by l and the radial index is represented by p. We can see from intensity distribution of the first few mode orders (Figure 47), that for when p = l = 0, we return to the solution for the fundamental Gaussian. When l = 0, the azimuthal dependence on phase $il\phi$ disappears and the intensity is nonzero at the center. When l $\neq$ 0 the power at the center is zero and the phase front of the beam varies with $il\phi$.

Appendix B

Gouy Phase

Gouy phase as defined in A.13, is the deviation of the optical phase front as a function of the Gaussian beam propagation along the $\hat{z}$-axis, which has a range of $\zeta = \pm\pi/2$ for $z = \pm\inf$. This can physically be interpreted as the Gaussian beam behaving like a plane wave in the near field ($z \approx 0$) and behaving like a spherical wave when in the far field ($z \approx \pm\inf$). To see how this translates to how Gouy phase is used in LIGO consider that the alignment of a laser beam can be described by the two degrees of freedom: position and angle from the optical axis. By placing a sensor at the origin or at the beam waist, we expect our measurement to have higher sensitivity to rotation of the beam angle compared to placing our sensor at the far field where we expect higher sensitivity to the displacement of the laser. Therefore, in order to sample both alignment degrees of freedom, we must have two sensors separated by 90 degrees of Gouy phase.

In practice the near field is not always the ideal location for placing a sensor, as putting a sensor inside a Fabry-Perot cavity to measure changes in waist size would be impossible. Typically, the way to measure such a degree of freedom would be to sample a pick-off beam either in transmission or reflection of the optical cavity and using a telescope (series of lenses) to ensure the sensors are placed at the appropriate Gouy phase [1]. Then by rotating to the eigenbasis of the optical cavity, or optical system, create a matrix that describes the sensitivity to particular degree of freedom. This is known as constructing a *sensing matrix*. Actually, sensors are seldomly placed

---

[1]Note a direct way of measuring the Gouy phase of the beam does not yet exist so typically one must model the propagation of the beam and fit the beam waist.

in the near field and far field for this reason and, in most cases, it is typically easier to place sensors at $\pm$ 45 degrees Gouy phase.

In LIGO, the discussion of Gouy phase is often presented in the context of discussing the round trip phase accumulation in an optical cavity. As I will show, this is important because Gouy phase is proportional to the spacing between spatial modes, or *transverse mode spacing*, in an optical cavity. The relationship between the Gouy phase and transverse mode spacing of an optical cavity is given by the relation:

$$\nu_{TMS} = \frac{\zeta}{2\pi} \nu_{FSR} \tag{B.1}$$

The discussion I present here is only brief; however, I encourage the reader to review the LIGO technical note by Koji Arai for a detailed overview on the topic [76]. Recall that the free spectral range $\nu_{FSR} = c/2L$ defines the spacing between the fundamental mode resonance peaks in the cavity. Additionally, the Gouy phase propagation for higher order modes in a cavity is much different than the fundamental (i.e. $\zeta_{nm} = (m + n + 1)\zeta(z)$), such that higher order modes *see* a much different cavity than the fundamental. It can be shown that the round trip accumulated Gouy phase shift can be computed from the round trip ABCD matrix of the optical cavity such that:

$$\zeta = sgnB \; cos^{-1} \left(\frac{A + D}{2} \right), \tag{B.2}$$

where A,B,C, and D are the matrix elements of the optical system of interest.

Appendix C

Improving SNR with Signal Averaging

Consider the noisy signal with a signal component $n_s(t)$ and added Gaussian noise $\tilde{n}_s(t)$:

$$n(t) = n_s(t) + \tilde{n}_s(t) \tag{C.1}$$

Assuming that the signal measurements are independent and samples are equally-spaced, then the noiseless signal is simply the sum over each repetition of the measurement N.

$$\sum_{i=1}^{N} n_s(t) = N n_s(t) \tag{C.2}$$

For completely random noise, with zero mean and variance σ_n, after N repetitions of the measurement, the average noise is simply the average over the variances.

$$\sum_{i=1}^{N} \tilde{n}_s(t) = \sqrt{N \sigma_n^2} = \sqrt{N} \sigma_n \tag{C.3}$$

Therefore, the averaged signal-to-noise ratio (SNR_N) is given by:

$$SNR_N = \frac{N n_s}{\sqrt{N} \sigma_n} = \sqrt{N} \, SNR \tag{C.4}$$

Considering only the signal, we see that it is improved by a factor of $1/\sqrt{N}$.

Appendix D

Image Analysis Code

Parameters

```matlab
1  function p=paramsPCsensdata()
2
3  % defines directory information for data retrieval
4  p.dir.meas_name = '062420data';  % Measurement name and date
       (user defined)
5  p.dir.data_folder = ['/Volumes/MUNIZERIK/
       ModulationDepth_variation_062420/',p.dir.meas_name,'/']; %
        Directory where measurement data is stored (user defined)
6  p.dir.meas_type = {'Amplitude','Phase','Ambient'}; %
       Measurement type designator (changes depend on measurement
       )
7  p.dir.p_inc_str = {'0.007','0.024','0.031','0.046'}; %
       Measured modulation depth for labeling purposes %'0.031',
8
9  % parameters of phase camera
10 p.camera.pix_size = 0.015; % Physical pixel size [mm]
11 p.camera.pixelarea = p.camera.pix_size^2; % Individual pixel
       area
12 p.camera.filtertrans = 0.05; % Attenuation factor of IR band-
       pass filter coating (transmission)
```

```matlab
13  p.camera.QE = 0.02; % quantum efficiency of standard cmos
       camera @1064 [e-/s/photon/s] [cite:https://www.thorlabs.
       com/newgrouppage9.cfm?objectgroup_id=4024]
14  p.camera.imgSizeX = 320;
15  p.camera.imgSizeY = 240;
16  p.camera.t_exp = 32e-3; % Exposure time for quad measurements
        [s]
17  p.camera.t_exp_ac = 6.4e-3; % Exposure time for quad
       measurements [s] [dead_time_factor*(t_dc/total_quad_number
       )]
18
19  % measurement parameters
20
21  p.data.P_inc = 7.24e-6; % Incident power on camera [W]
22  p.data.dc_volt = [232e-3 232e-3 232e-3 232e-3]; % DC voltage
       measured on PD [Volts]   %232e-3
23  p.data.rf_volt = [7.4e-3 27.2e-3 34.4e-3 50.8e-3]; % RF
       voltage measured on PD [Volts] %34.4e-3
24  p.data.rf_volt_err = [2e-3 2e-3 2e-3 2e-3]; %Uncertainty in
       RF voltage measured on PD [Volts]
25  p.data.dc_volt_err = [1e-3 1e-3 1e-3 1e-3]; %Uncertainty in
       RF voltage measured on PD [Volts]
26  p.data.dc_ohm = 1975; % Transimpedance of DC channel [Volts/
       Amp]
27  p.data.rf_ohm = 4750; % Transimpedance of RF channel [Volts/
       Amp]
28
29  % physical and measurement constants
30  p.constant.q_e = 1.6e-19; % charge of an electron [C]
31  p.constant.h = 6.626e-34; % Planck's constant [Joules*s]
32  p.constant.c = 3e8; % Speed of light [m/s]
33  p.constant.wavelength = 1064e-9; % Wavelength of incident
       light [m]
```

```matlab
34  p.constant.R_pd = 0.08; % Responsivity of bbRF photodiode [A/
        W] [cite:https://dcc.ligo.org/DocDB/0025/D1002969/008/
        BroadbandPD.pdf]
35  p.constant.E_photon = (p.constant.h*p.constant.c)/p.constant.
        wavelength; % Energy per photon @ 1064nm [J/photon]
36  p.constant.QE_pd = (p.constant.R_pd/p.constant.wavelength)...
         % quantum efficiency of bb photodiode @1064 [e-/s/photon/
        s]
37                           *((p.constant.h*p.constant.c)/p.constant.
                             q_e);
38
39  % Create a grid and boundary conditions for circular ROI and
        fitting
40  [p.grid.column,p.grid.row] = meshgrid(1:p.camera.imgSizeX,1:p
        .camera.imgSizeY); % Creates 240x320 grid of row and
        column to define image size
41  p.grid.xpos = -((p.camera.imgSizeX-1)*p.camera.pix_size)...
                       % Rescales grid to physical dimensions of
        camera in x-direction
42                    /2:p.camera.pix_size:((p.camera.imgSizeX-1)
                        ...
43                    *p.camera.pix_size)/2;
44  p.grid.ypos = -((p.camera.imgSizeY-1)*p.camera.pix_size)...
                       % Rescales grid to physical dimensions of
        camera in x-direction
45                    /2:p.camera.pix_size:((p.camera.imgSizeY-1)
                        ...
46                    *p.camera.pix_size)/2;
47
48  % Creating regions of interest(ROI) for analysis
49  p.ROI1.label = 'circular';
50  p.ROI1.centerX = 167;
51  p.ROI1.centerY = 110;
```

```
52  p.ROI1.radius = 25;
53  p.ROI1.cmask = (p.grid.row − p.ROI1.centerY).^2 ...
54                     + (p.grid.column − p.ROI1.centerX).^2 <= p.
                         ROI1.radius.^2;
55
56  p.ROI2.label = 'large square';
57  p.ROI2.width = 40;
58  p.ROI2.height = 40;
59  p.ROI2.centerX = 167;
60  p.ROI2.centerY = 110;
61  p.ROI2.x1 = p.ROI2.centerX−p.ROI2.width/2;
62  p.ROI2.x2 = p.ROI2.centerX+p.ROI2.width/2;
63  p.ROI2.y1 = p.ROI2.centerY−p.ROI2.height/2;
64  p.ROI2.y2 = p.ROI2.centerY+p.ROI2.height/2;
65
66  p.ROI3.label = 'small square';
67  p.ROI3.width = 2;
68  p.ROI3.height = 2;
69  p.ROI3.centerX = 163;
70  p.ROI3.centerY = 112;
71  p.ROI3.x1 = p.ROI3.centerX−p.ROI3.width/2;
72  p.ROI3.x2 = p.ROI3.centerX+p.ROI3.width/2;
73  p.ROI3.y1 = p.ROI3.centerY−p.ROI3.height/2;
74  p.ROI3.y2 = p.ROI3.centerY+p.ROI3.height/2;
75
76  % Calculate parameters of incident light signal
77  p.signal.dc_current = p.data.dc_volt./p.data.dc_ohm; % DC
        current generated in bbPD from carrier signal
78  p.signal.rf_current = p.data.rf_volt./p.data.rf_ohm; % RF
        current generated in bbPD from modulated signal
79  p.signal.delrf = 0.5*(p.data.dc_ohm./(p.data.dc_volt.*p.data.
        rf_ohm));
```

```
80  p.signal.deldc = -0.5*((p.data.rf_volt.*p.data.dc_ohm)./(p.
        data.dc_volt.^2.*p.data.dc_ohm));
81  % p.signal.dc_current_relative_err = (p.data.dc_volt_err./p.
        data.dc_volt)./p.data.dc_ohm;
82  % p.signal.rf_current_relative_err = (p.data.rf_volt_err./p.
        data.rf_volt)./p.data.rf_ohm;
83  p.signal.gamma = (p.signal.rf_current./p.signal.dc_current)
        /2; % Modulation depth calculated as: I_rfpeak/I_dc
84  % p.signal.gamma_err = (p.signal.rf_current_relative_err./p.
        signal.dc_current_relative_err)/2;
85  p.signal.gamma_err = sqrt((p.signal.delrf).^2.*(p.data.
        rf_volt_err).^2 + (p.signal.deldc).^2.*(p.data.dc_volt_err
        ).^2);
86  p.signal.Psensor = p.data.P_inc*p.camera.filtertrans; % Power
         incident on camera
87
88  p.signal.E_beam = p.signal.Psensor*p.camera.t_exp; % photons
        per watt in DC signal
89  p.signal.Np_dc = p.signal.E_beam/p.constant.E_photon; %
        Calculated photons per pixel in dc [# photons]
90  p.signal.Ne_dc = p.camera.QE*p.signal.Np_dc; % Calculated
        photoelectrons per pixel in dc [# e-]
91  p.signal.Ne_ac = p.signal.gamma.*p.signal.Ne_dc; % Calculated
         photoelectrons per pixel in rf [# e-]
92
93
94
95
96  % p.signal.E_beam = p.data.P_inc*p.camera.t_exp*p.camera.
        filtertrans; % photons per watt in DC signal
97  % p.signal.Np_dc = p.signal.E_beam/p.constant.E_photon; %
        Calculated photons per pixel in dc [# photons]
```

```matlab
98  % p.signal.Ne_dc = p.camera.QE*p.signal.Np_dc; % Calculated
        photoelectrons per pixel in dc [# e-]
99
100
101
102  % Parameters for signal model used in calibration
103  p.signalmodel.coordsys = 'Cartesian'; %Coordinate system
104  [p.signalmodel.xgrid,p.signalmodel.ygrid] = meshgrid(p.grid.
        xpos,...  % Creates 240x320 grid of row and column to
        scaled to physical sensor size
105                                                    p.grid.
                                                        ypos)
                                                          ;
106  p.signalmodel.Z(:,:,1) = p.signalmodel.xgrid;
107  p.signalmodel.Z(:,:,2) = p.signalmodel.ygrid;
108  p.signalmodel.initialguess = [4,0,.5,0,.5,0];
109  p.signalmodel.lb = [0,-p.camera.imgSizeX*p.camera.pix_size
        /2,0,...
110                          -p.camera.imgSizeX*p.camera.pix_size
                                /2,0,0];
111  p.signalmodel.ub = [realmax('double'),(p.camera.imgSizeX*p.
        camera.pix_size)/2,...
112                          ((p.camera.imgSizeX*p.camera.pix_size)/2)
                                ^2,...
113                          (p.camera.imgSizeX*p.camera.pix_size)
                                /2,...
114                          ((p.camera.imgSizeX*p.camera.pix_size)/2)
                                ^2,pi/4];
115
116  p.signalmodel.gauss =  @(A,Z) A(1)*exp( -2*((Z(:,:,1)-A(2))
        .^2/(A(3)^2)... % Numerical model of 2D gaussian
117                                   + (Z(:,:,2)-A(4)).^2/(A(5)^2))
                                        );
```

```
118  %p.signalmodel.gauss =  @(A,Z) A(1)*exp( −((Z(:,:,1)−A(2))
         .^2/(2*A(3)^2)... % Numerical model of 2D gaussian
119                                      %+ (Z(:,:,2)−A(4)).^2/(2*A(5)
                                            ^2)) );
```

Camera Calibration

```
1  %
2  %
   _____

3  % function [g, gauss_coeff] = CalibrateData(p,measurement,
      imgFiles)
4  %
5  %
6  % Inputs: input parameters, measurement data, and image file
      data
7  % Outputs: calibration factor "g" and gaussian fit
         coefficients
8  %
9  %
10 %
11 % Erik Muniz 07.01.2020
12 %
   _____

13 %
14
15 function [g,gauss_coeff] = CalibrateSensData(p,measurement)
16
17 for j = 1:length(p.dir.p_inc_str)
18     img_frame_array.dc = cat(3, measurement(3).imgs{:,j});
19     img_frame_array.ac = cat(3, measurement(1).imgs{:,j});
```

```
20
21        mean_imgs.dc = mean(img_frame_array.dc,3);
22        mean_imgs.ac = mean(img_frame_array.ac,3);
23
24        ac_crop = mean_imgs.ac.*p.ROI1.cmask;
                                               % Crops circular ROI
              from ac images
25        dc_crop = mean_imgs.dc.*p.ROI1.cmask;
                                               % Crops circular ROI
              from dc images
26
27
28        % Fitting gaussian profile to mean images
29        [gauss_coeff.dc{j},resnorm{j},res{j}] = lsqcurvefit(p.
              signalmodel.gauss, p.signalmodel.initialguess(1:5),...
30                        p.signalmodel.Z, dc_crop, p.
                              signalmodel.lb(1:5), p.signalmodel
                              .ub(1:5));
31
32        Area_beam_dc = pi*gauss_coeff.dc{j}(3)*gauss_coeff.dc{j
              }(5); % Effective beam mode area on camera of DC beam
33
34        I_dc_0 = (2*p.signal.Psensor)/Area_beam_dc; % Number of
              electrons per pixel with light sensitive area A_pix (
              DC)
35
36        Isensor_coeff = [I_dc_0, gauss_coeff.dc{j}(2),
              gauss_coeff.dc{j}(3),...
37                        gauss_coeff.dc{j}(4), gauss_coeff.dc{j}(5)
                              ];
38
39        Isensor_gauss = p.signalmodel.gauss(Isensor_coeff,p.
              signalmodel.Z); % Gaussian profile of incident beam
```

```matlab
40
41        Np_gauss_dc = (Isensor_gauss.*p.camera.t_exp)./p.constant
              .E_photon;
42        Ne_gauss_dc = p.camera.QE.*Np_gauss_dc;
43        Ne_gauss_ac = Ne_gauss_dc.*p.signal.gamma(j);
44
45
46        S_dn_dc = sum(dc_crop(:));
47        S_dn_ac = sum(ac_crop(:));
48
49        g.dc(j) = (p.camera.pixelarea*sum(sum(Ne_gauss_dc.*p.ROI1
              .cmask)))/S_dn_dc;
50        g.ac(j) = (p.camera.pixelarea*sum(sum(Ne_gauss_ac.*p.ROI1
              .cmask)))/S_dn_ac;
51
52
53   end
54
55   g.dc = mean(g.dc(1:4));
56   g.ac = mean(g.ac(1:4));
57
58
59   %% ——Plot Data——
60
61   % % Plot 3D Data and Fitted curve for DC image
62   %
63   % % Plot AC signal and fit
64   %
65   % hf1=figure(100); set(hf1,'Position',[1000 600 800 500]);
66   % C = del2(gauss(A,Z));
67   % s = mesh(p.grid.xpos(1:320),p.grid.ypos(1:240),gauss(A,Z),C
          );
68   % s.FaceColor = 'flat'; hold on
```

```
69 % surface(p.grid.xpos,p.grid.ypos,dc_sig,'EdgeColor','none');
       alpha(0.5);
70 % colormap('jet'); view(-35,40); grid on;
71 % xlabel('Position (mm)','FontName','Helvetica','FontWeight
       ','bold','FontSize',14,'Rotation',15)
72 % ylabel('Position (mm)','FontName','Helvetica','FontWeight
       ','bold','FontSize',14,'Rotation',-27)
73 % zlabel('Digital Number (DN)','FontName','Helvetica','
       FontWeight','bold','FontSize',20)
74 %
75 %
76 %
77 % hf2=figure(105); set(hf2,'Position',[1000 600 800 500]);
78 % C2 = del2(gauss(A2,Z));
79 % s = mesh(p.grid.xpos(1:320),p.grid.ypos(1:240),gauss(A2,Z),
       C2); hold on
80 % s.FaceColor = 'flat'; hold on
81 % surface(p.grid.xpos,p.grid.ypos,A_sig,'EdgeColor','none');
       alpha(0.5);
82 % colormap('pink'); view(-35,40); grid on;
83 % xlabel('Position (mm)','FontName','Helvetica','FontWeight
       ','bold','FontSize',14,'Rotation',15)
84 % ylabel('Position (mm)','FontName','Helvetica','FontWeight
       ','bold','FontSize',14,'Rotation',-27)
85 % zlabel('Digital Number (DN)','FontName','Helvetica','
       FontWeight','bold','FontSize',20)
86 %
87 %
88 % figure(105)
89 % s = mesh(p.grid.xpos(1:320),p.grid.ypos(1:240),gauss(A2,Z))
       ;
90 % s.FaceColor = 'flat';
```

```matlab
91  % xlabel('Position (mm)','FontName','Helvetica','FontWeight
       ','bold','FontSize',14,'Rotation',15)
92  % ylabel('Position (mm)','FontName','Helvetica','FontWeight
       ','bold','FontSize',14,'Rotation',-27)
93  % zlabel('Digital Number (DN)','FontName','Helvetica','
       FontWeight','bold','FontSize',20)
94  %
95  % figure(106)
96  % s1 = mesh(p.grid.xpos(1:320),p.grid.ypos(1:240),A_sig);
97  % s1.FaceColor = 'flat';
98  % xlabel('Position (mm)','FontName','Helvetica','FontWeight
       ','bold','FontSize',14,'Rotation',15)
99  % ylabel('Position (mm)','FontName','Helvetica','FontWeight
       ','bold','FontSize',14,'Rotation',-27)
100 % zlabel('Digital Number (DN)','FontName','Helvetica','
       FontWeight','bold','FontSize',20)
101 %
102 % figure(107)
103 % s2 = mesh(p.grid.xpos(1:320),p.grid.ypos(1:240),res2);
104 % s2.FaceColor = 'flat';
105 % xlabel('Position (mm)','FontName','Helvetica','FontWeight
       ','bold','FontSize',14,'Rotation',15)
106 % ylabel('Position (mm)','FontName','Helvetica','FontWeight
       ','bold','FontSize',14,'Rotation',-27)
107 % zlabel('Digital Number (DN)','FontName','Helvetica','
       FontWeight','bold','FontSize',20)
108 %
109 % figure(103)
110 % mesh(p.grid.xpos(1:320),p.grid.ypos(1:240),g_dc.*dc_sig)
111 % xlabel('Position (mm)','FontName','Helvetica','FontWeight
       ','bold','FontSize',14,'Rotation',15)
112 % ylabel('Position (mm)','FontName','Helvetica','FontWeight
       ','bold','FontSize',14,'Rotation',-27)
```

```matlab
113 % zlabel('Generated Photoelectrons','FontName','Helvetica','
        FontWeight','bold','FontSize',20)
114 %
115 % figure(108)
116 % mesh(p.grid.xpos(1:320),p.grid.ypos(1:240),g_ac.*A_sig)
117 % xlabel('Position (mm)','FontName','Helvetica','FontWeight
        ','bold','FontSize',14,'Rotation',15)
118 % ylabel('Position (mm)','FontName','Helvetica','FontWeight
        ','bold','FontSize',14,'Rotation',-27)
119 % zlabel('Generated Photoelectrons','FontName','Helvetica','
        FontWeight','bold','FontSize',20)
120 %
121 % figure(109)
122 % s = mesh(p.grid.xpos(1:320),p.grid.ypos(1:240),g_ac.*gauss(
        A2,Z));
123 % s.FaceColor = 'flat';
124 % xlabel('Position (mm)','FontName','Helvetica','FontWeight
        ','bold','FontSize',14,'Rotation',15)
125 % ylabel('Position (mm)','FontName','Helvetica','FontWeight
        ','bold','FontSize',14,'Rotation',-27)
126 % zlabel('Generated Photoelectrons','FontName','Helvetica','
        FontWeight','bold','FontSize',20)
127 %
128 % figure(110)
129 % s = mesh(p.grid.xpos(1:320),p.grid.ypos(1:240),(g_ac.*A_sig
        -g_ac.*gauss(A2,Z)));
130 % s.FaceColor = 'flat';
131 % xlabel('Position (mm)','FontName','Helvetica','FontWeight
        ','bold','FontSize',14,'Rotation',15)
132 % ylabel('Position (mm)','FontName','Helvetica','FontWeight
        ','bold','FontSize',14,'Rotation',-27)
133 % zlabel('Generated Photoelectrons','FontName','Helvetica','
        FontWeight','bold','FontSize',20)
```

Calculating Noise in RF Amplitude and Phase

```
1  %
2  %

3  % function [pix2pix_noise,fr2fr_noise,sig_calc] = MeasNoise(p
       ,measurement,gauss_coeff,g)
4  %
5  %
6  % Inputs: p, measurement, gaussian coefficients from fit, and
        calibration factor
7  % Outputs: pix2pix_noise, fr2fr_noise, and measured signal −
       sig_calc
8  %
9  % MeasNoise takes input frame files from dc and ac
       measurements and
10 % calculates noise fluctuations between neighboring pixels (
       spatial) and
11 % fluctuations between frames (temporal) by taking the
       standard deviation
12 % of these quantities.
13 %
14 %
15 % Erik Muniz 07.01.2020
16 %

17 %
18
19 function [sig_calc,sub_avgrms,frameavg1] = MeasNoise(p,
       measurement,g)
20
```

```matlab
21  for  j  =  1:length(p.dir.p_inc_str)
22      img_frame_array  =  cat(3,  measurement.imgs{:,j});
23
24      mean_imgfr  =  mean(img_frame_array,3);
25      %mean_imgcrop  =  mean_imgfr.*p.ROI1.cmask;
26      mean_imgcrop  =  mean_imgfr(p.ROI2.y1:p.ROI2.y2,p.ROI2.x1:p
            .ROI2.x2,:);
27
28      % Compute  average  of  10  frames
29      frameavg1  =  [1,4,16,36,49];
30      for  l  =  1:length(frameavg1)
31          r  =  randperm(50,frameavg1(l));
32          for  k  =  1:length(r)
33              m  =  r(k);
34              if  k  ==  1
35                  img_sum  =  img_frame_array(:,:,m);
36              elseif  k>1
37                  img_sum  =  img_sum  +  img_frame_array(:,:,m);
38              end
39          end
40          img_avg1{l}  =  img_sum(p.ROI2.y1:p.ROI2.y2,p.ROI2.x1:p
                .ROI2.x2,:)./frameavg1(l);
41  %           subtracted_avgimgs  =  img_avg-mean_imgfr;
42  %           subtracted_avgimgs_rms{l,j}  =  g*rms(
                subtracted_avgimgs(:));
43      end
44
45      for  l  =  1:length(frameavg1)
46          r  =  50+randperm(50,frameavg1(l));
47          for  k  =  1:length(r)
48              m  =  r(k);
49              if  k  ==  1
50                  img_sum  =  img_frame_array(:,:,m);
```

```matlab
51              elseif k>1
52                  img_sum = img_sum + img_frame_array (: ,: ,m) ;
53              end
54          end
55          img_avg2{l} = img_sum (p.ROI2.y1:p.ROI2.y2 ,p.ROI2.x1:p
                .ROI2.x2 ,:) ./ frameavg1(l) ;
56          %           subtracted_avgimgs = img_avg−mean_imgfr ;
57          %           subtracted_avgimgs_rms{l ,j} = g∗rms (
                subtracted_avgimgs (:) ) ;
58          sub_avg = (img_avg1{l} − img_avg2{l}) ./ sqrt (2) ;
59          sub_avgrms{l ,j} = g∗std (sub_avg (:) ) ;
60      end
61
62
63 %      for l = 1:length (frameavg)
64 %          for m = 1:frameavg(l)
65 %              subtracted_img (: ,: ,m) = img_frame_array (: ,: ,m)−
    img_frame_array (: ,: ,m+1) ;
66 %              if m == 1
67 %                  sub_sum = subtracted_img (: ,: ,m) ;
68 %                  img_sum = img_frame_array (: ,: ,m) ;
69 %              elseif m>1
70 %                  sub_sum = sub_sum + subtracted_img (: ,: ,m) ;
71 %                  img_sum = img_sum + img_frame_array (: ,: ,m) ;
72 %              end
73 %          end
74 %          img_avg = img_sum (p.ROI2.y1:p.ROI2.y2 ,p.ROI2.x1:p.
    ROI2.x2 ,:) ./ frameavg(l) ;
75 %          sig_mean{l ,j} = g∗mean(img_avg (:) ) ;
76 %          sub_avg = sub_sum ./ frameavg(l) ;
77 %          sub_avgstd{l ,j} = g∗rms (sub_avg (:) ) ;
78 %          fr2fr_se{l ,j} = g∗(std (sub_avg (:) )/sqrt (2) ) ;
79 %      end
```

```matlab
80
81 %        subtracted_img = img_frame_array(:,:,1)-mean_imgfr;
82 %        subtracted_imgfr2fr = img_frame_array(:,:,1)-
       img_frame_array(:,:,2);
83 %
84       sig_calc(j) = g*mean(mean_imgcrop(:));
85      %pix2pix_noise(j) = g*rms(subtracted_img(:));
86 %        fr2fr_std(j) = g*(mean(subtracted_imgfr2fr(:))/sqrt(2))
       ;
87 %        fr2fr_se(j) = g*(std(subtracted_imgfr2fr(:))/sqrt(2));
88      % pixstd_frames{j} = g*std(img_frame_array,0,3);
89
90
91 end
92
93 % sig_calc = cell2mat(sig_calc);
94  sub_avgrms = cell2mat(sub_avgrms);
95 % fr2fr_se = cell2mat(fr2fr_se);
96
97 % figure(114)
98 % subplot(1,2,1),
99 % imagesc(img_frame_array(:,:,1))
100 % set(gca,'TickLength',[0  0]);
101 %        set(gca,'XTickLabel',{});
102 %        set(gca,'YTickLabel',{});
103 %        colormap(gca,'bone')
104 %        hcb1 = colorbar;
105 %        hcb1.Location = 'northoutside';
106 %        hcb1.Label.String = 'Digital Number (DN)';
107 %        hcb1.Label.FontName = 'Helvetica';
108 %        hcb1.Label.FontSize = 14;
109 % subplot(1,2,2)
110 % imagesc(subtracted_imgfr2fr)
```

```
111 % set(gca,'TickLength',[0  0]);
112 %       set(gca,'XTickLabel',{});
113 %       set(gca,'YTickLabel',{});
114 %       colormap(gca,'bone')
115 %       hcb1 = colorbar;
116 %       hcb1.Location = 'northoutside';
117 %       hcb1.Label.String = 'Digital Number (DN)';
118 %       hcb1.Label.FontName = 'Helvetica';
119 %       hcb1.Label.FontSize = 14;
120 %

  1 %
```

```
  2 % function [pix2pix_noise,fr2fr_noise,sig_calc] =
        MeasPhaseNoise(p,measurement,gauss_coeff,g)
  3 %
  4 %
  5 % Inputs: p, measurement, gaussian coefficients from fit, and
          calibration factor
  6 % Outputs: pix2pix_noise, fr2fr_noise, and measured signal -
        sig_calc
  7 %
  8 % MeasNoise takes input frame files from dc and ac
          measurements and
  9 % calculates noise fluctuations between neighboring pixels (
          spatial) and
 10 % fluctuations between frames (temporal) by taking the
        standard deviation
 11 % of these quantities.
 12 %
 13 %
 14 % Temporal noise is measured as the std of pixel values
```

```matlab
15 % between multiple frames. This gives the noise for every
      pixel value in
16 % the image. The average of all the noise values in the std
17 % map is then calculated to determine the temporal noise. This ensures that
18 % fixed pattern noise and other spatial noise is averaged out
      .
19 %
20 %
21 % Erik Muniz 07.01.2020
22 %
```

```matlab
23 %
24
25 function [phasestdnoise_map, phase_noisesingleval] =
      MeasPhaseNoise(p, measurement)
26
27 for j = 1:length(p.dir.p_inc_str)
28     img_frame_array = cat(3, measurement.imgs{:,j});
29     mean_imgfr = mean(img_frame_array,3);
30     mean_imgcrop = mean_imgfr(p.ROI2.y1:p.ROI2.y2,p.ROI2.x1:p
          .ROI2.x2,:);
31
32     phasestdnoise_map{j} = sqrt(length(img_frame_array(1,1,:)
          )...
33                          /(length(img_frame_array(1,1,:))-1))...
34                          .*std(img_frame_array,0,3);
                                    % Map of std between
                          pixel values stdperpix = sqrt(N/N-1)*
                          sqrt(1/N*sum_{i=1}^{N}(X_{j,i}-X_{AVG,
                          j}^2)
```

```matlab
35        phasestdnoise_maproi = phasestdnoise_map{j}(p.ROI2.y1:p.
              ROI2.y2,p.ROI2.x1:p.ROI2.x2,:); % Restricts analysis
              of noise to region of interest
36        phase_noisesingleval(j) = mean(phasestdnoise_maproi(:));
37
38
39  end
40
41  %sigma_phase = temp_noise./avg_sig;
42
43  figure(114)
44  imagesc(mean_imgcrop)
45  set(gca,'FontWeight','bold')
46      colormap(gca,'parula')
47      hcb1 = colorbar;
48      hcb1.Location = 'eastoutside';
49      hcb1.Label.String = '\phi (rad)';
50      hcb1.Label.FontName = 'Helvetica';
51      hcb1.Label.FontSize = 16;
52      hcb1.FontWeight = 'bold';
53  set(gcf,'Units','inches');
54  screenposition = get(gcf,'Position');
55  set(gcf,...
56  'PaperPosition',[0 0 screenposition(3:4)],...
57  'PaperSize',[screenposition(3:4)]);
58  print('PhaseSig','-dpdf','-fillpage')
59  figure(115)
60  imagesc(phasestdnoise_maproi)
61  set(gca,'FontWeight','bold')
62      colormap(gca,'parula')
63      hcb1 = colorbar;
64      hcb1.Location = 'eastoutside';
65      hcb1.Label.String = '\phi (rad)';
```

```matlab
66        hcb1.Label.FontName = 'Helvetica';
67        hcb1.Label.FontSize = 16;
68        hcb1.FontWeight = 'bold';
69   set(gcf,'Units','inches');
70   screenposition = get(gcf,'Position');
71   set(gcf,...
72   'PaperPosition',[0 0 screenposition(3:4)],...
73   'PaperSize',[screenposition(3:4)]);
74   print('PhaseStd','-dpdf','-fillpage')
75
76   % figure(39)
77   % loglog(avg_sig,phase_noisesingleval(1:3),'square')
78   % hold on
79   % grid on
80   % ylim([2e-1 5e-1])
81   % xlim([.7e4 1.7e4])
82   % loglog(avg_sig,sigma_phase,'^')
83   % legend({'Measured Total Noise in Phase','Estimated Noise in
            Phase: \sigma_{\phi} = \sigma_{AC}/<AC>'},'FontSize',12,'
        FontName','Helvetica');
84   %
85   % ylabel('Noise (rad)','FontName','Helvetica','FontSize',18,'
        FontWeight','bold');
86   % xlabel('(Averaged Signal - Offset) [e^{-}]','FontName','
        Helvetica','FontSize',18,'FontWeight','bold');
87   % set(gcf,'Units','inches');
88   % screenposition = get(gcf,'Position');
89   % set(gcf,...
90   % 'PaperPosition',[0 0 screenposition(3:4)],...
91   % 'PaperSize',[screenposition(3:4)]);
92   % print('PhaseNoise','-dpdf','-fillpage')
```
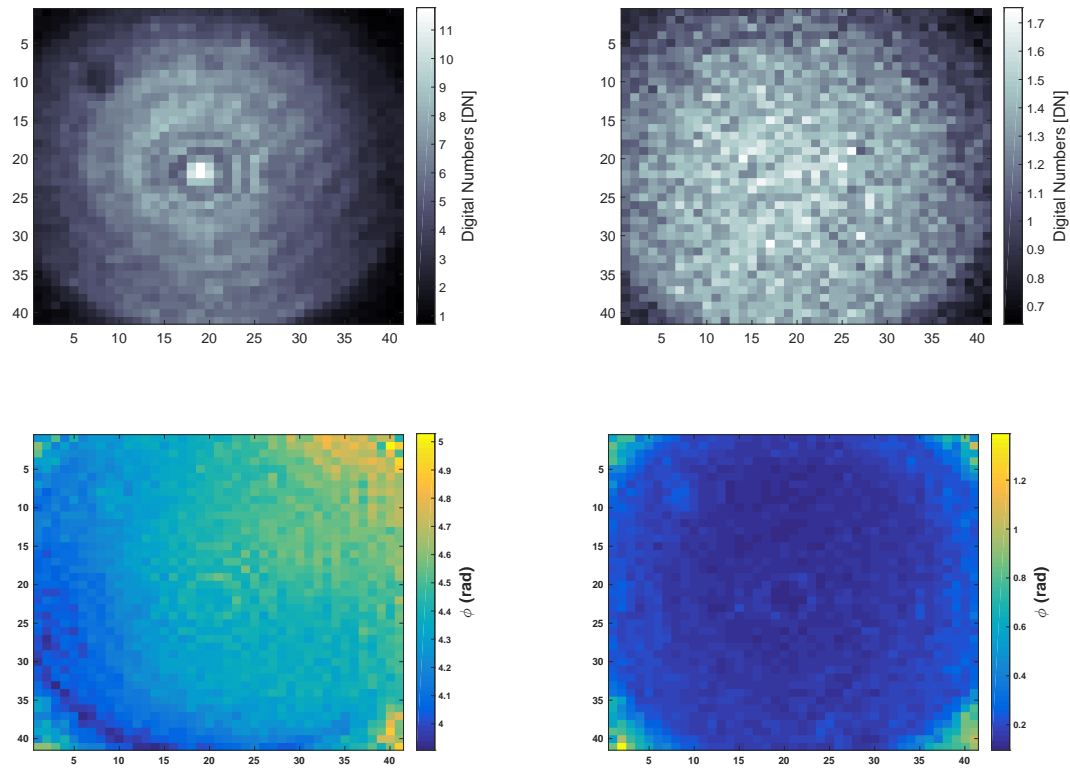
Figure 48: Left: Subregions of illuminated image ($P_{inc} = 6\mu W$, $\Gamma = 0.046$ – @32 ms exposure) for both phase and amplitude. Amplitude images are averaged over 40x40x101 pixels to determine average signal per frame per pixel. Right: Standard deviation computed for every pixel in the subregion for 101 frames for both phase and amplitude. The resulting standard deviation map is spatially averaged to get a single value for temporal noise.

Appendix E

Simple Point Absorber Model Calculation

We use Equation 4.8 to describe the modulated field incident on the beam splitter picture in Figure 38. In this case we assume that the incident carrier and the sidebands fields primarily the TEM_{00} mode, such that $E_c = U_{00} = \Psi_0$. The power in the fundamental mode is then given by $P_0 = \int \Psi_0^* \Psi_0$ In our simple model we consider the prompt reflection off the beam splitter such that the induced phase shift of the beam splitter can be ignored for the reflected field in this case, the field of the carrier for both arms can be written as:

$$E_c^x = \frac{1}{\sqrt{2}} \Psi_0 e^{i\phi_{s_x}} \cdot e^{i\phi_{DARM}^x} \tag{E.1}$$

$$E_c^y = \frac{1}{\sqrt{2}} \Psi_0 e^{i\phi_{s_y}} \cdot e^{i\phi_{DARM}^y} \tag{E.2}$$

The factor of $1/\sqrt{(2)}$ appears from transmission through the beam splitter and the exponential terms are due to the single bounce phase accumulation of the DARM offset and Schnupp asymmetry. Considering the symmetry between the arms:

$$\phi_{s_x} = \frac{\phi_s}{2} \qquad\qquad \phi_{s_y} = -\frac{\phi_s}{2} \tag{E.3}$$

$$\phi_{DARM}^x = \frac{\phi_{DC}}{2} \qquad\qquad \phi_{DARM}^y = -\frac{\phi_{DC}}{2} \tag{E.4}$$

One should note that ϕ_{DC}, by definition includes the round trip number of bounces for the Fabry-Perot cavity. In this case $\phi_{DC} = N\phi_{DARM}$, where N is the number of round trip bounces in the arm cavity. Additionally, the phase shift produced by the Schnupp asymmetry is defined by $\phi_s = \omega_{c,s}l_s/c$, where ω is the respective frequency of the carrier or sideband, l_s is the Schnupp length, and c is the speed of light.

Carrier

The carrier field in each arm at the beam splitter after a single round trip is

$$E_c^{x,BS} = \frac{\Psi_0}{\sqrt{2}} e^{i\phi_s} e^{i\frac{\phi_{DC}}{2}} \tag{E.5}$$

$$E_c^{y,BS} = \frac{\Psi_0}{\sqrt{2}} e^{-i\phi_s} e^{-i\frac{\phi_{DC}}{2}} \tag{E.6}$$

and the recombined carrier field at the anti-symmetric port is

$$E_c^{AS} = \frac{1}{2} \left(E_c^{x,BS} - E_c^{y,BS} \right) \tag{E.7}$$

$$= \frac{\Psi_0}{2} \left[e^{i(\phi_s + \phi_{DC}/2)} - e^{-i(\phi_s + \phi_{DC}/2)} \right] \tag{E.8}$$

letting $\theta = \phi_s + \phi_{DC}/2$,

$$= \frac{\Psi_0}{2} \left[e^{i\theta} - e^{-i\theta} \right] \tag{E.9}$$

Using Euler's identity $e^{i\theta} = \cos\theta + i\sin\theta$

$$= \frac{\Psi_0}{2} \left[(i\sin\theta + \cos\theta) - (-i\sin\theta + \cos\theta) \right] \tag{E.10}$$

$$= i\Psi_0 \sin\theta \tag{E.11}$$

$$= i\Psi_0 \sin(\phi_s + \phi_{DC}/2) \tag{E.12}$$

By design, when the MICH degree of freedom is held on resonance phase term containing the Schnupp asymmetry goes to zero ($\phi_s = 0$)

$$\therefore E_c^{AS} = i\Psi_0 \sin\left(\frac{\phi_{DC}}{2}\right) \tag{E.13}$$

Sidebands

Here I will derive the field propagation for the sidebands. Note that the only difference between the positive and negative sidebands is a difference in sign. For this reason we only need to solve for a single sideband. The incident field for the positive sideband is given by

$$E_{in}^+ = \Psi_0 \frac{i\Gamma}{2} e^{i\Omega t},\tag{E.14}$$

where Γ is the modulation index and Ω is the sideband frequency. Again, we consider the prompt reflection of the sideband off the beam splitter which contributes a factor of $1/\sqrt{2}$. Since the sideband is anti-resonant in the cavity, it only experiences a single pass through the test mass, which results in a round trip accumulation of the phase distortion in both arms (i.e. $2k\mathrm{X}(\vec{x},\vec{y})$, $2k\mathrm{Y}(\vec{x},\vec{y})$). Therefore, the field at the beam splitter, for say the x-arm, after the round trip will only include the phase distortion due to the point absorber, i.e.:

$$E_{sb+}^{x,BS} = i\frac{\Psi_0}{\sqrt{2}}\frac{\Gamma}{2} e^{i\Omega t} \left[e^{i\phi_s/2} \cdot e^{i\phi_s/2} \cdot e^{i2k\mathrm{X}(\vec{x},\vec{y})/2} \right]\tag{E.15}$$

$$= i\frac{\Psi_0}{\sqrt{2}}\frac{\Gamma}{2} e^{i\Omega t} \left[e^{i\phi_s} \cdot e^{ik\mathrm{X}(\vec{x},\vec{y})} \right]\tag{E.16}$$

Similarly for the y-arm,

$$E_{sb+}^{y,BS} = i\frac{\Psi_0}{\sqrt{2}}\frac{\Gamma}{2} e^{i\Omega t} \left[e^{-i\phi_s} \cdot e^{-ik\mathrm{Y}(\vec{x},\vec{y})} \right]\tag{E.17}$$

The recombined field at the AS port is then given by

$$E_{sb+}^{AS} = \frac{i}{2}\frac{\Psi_0}{2}\Gamma e^{i\Omega t} \left[e^{i(\phi_s+k\mathrm{X}(\vec{x},\vec{y}))} - e^{-i(\phi_s+k\mathrm{Y}(\vec{x},\vec{y}))} \right]\tag{E.18}$$

To simplify calculations, we assume that the Schnupp asymmetry can be tuned such that the phase distortion is symmetric to both arms $\Phi(x,y) = k\mathrm{X}(\vec{x},\vec{y}) = -k\mathrm{Y}(\vec{x},\vec{y})$. In this case, we can treat the calculation similar to the carrier field by making the substitution $\theta = \phi_s + \Phi(x,y)$:

$$E_{sb+}^{AS} = \frac{i}{2}\frac{\Psi_0}{2}\Gamma e^{i\Omega t}\left[e^{i(\phi_s+\Phi(x,y))} - e^{-i(\phi_s+\Phi(x,y))}\right] \tag{E.19}$$

$$= \frac{i}{2}\frac{\Psi_0}{2}\Gamma e^{i\Omega t}\left[e^{i\theta} - e^{-i\theta}\right] \tag{E.20}$$

$$= \frac{i}{2}\Psi_0\Gamma e^{i\Omega t}\left[i\sin(\phi_s + \Phi(x,y))\right] \tag{E.21}$$

Using common trigonometric identities we can expand and considering that the path distortion produced by the absorber is much smaller than the wavelength, we can use expansions for sine and cosine to approximate the effect of the absorber to first order (i.e. $\sin(\Phi(x,y)) \approx \Phi(x,y)$). Therefore,

$$= i\Psi_0\frac{\Gamma}{2}e^{i\Omega t}\left[i\sin(\phi_s) + i\cos(\phi_s)\Phi(x,y)\right] \tag{E.22}$$

For the negative sideband we get a similar expression,

$$E_{sb-}^{AS} = i\Psi_0\frac{\Gamma}{2}e^{-i\Omega t}\left[-i\sin(\phi_s) + i\cos(\phi_s)\Phi(x,y)\right] \tag{E.23}$$

therefore,

$$E_{sb+}^{AS} = -\Psi_0\frac{\Gamma}{2}e^{i\Omega t}\left[\sin(\phi_s) + \cos(\phi_s)\Phi(x,y)\right] \tag{E.24}$$

$$E_{sb-}^{AS} = -\Psi_0\frac{\Gamma}{2}e^{-i\Omega t}\left[-\sin(\phi_s) + \cos(\phi_s)\Phi(x,y)\right] \tag{E.25}$$

adding up both of the sidebands at the AS port we get:

$$E_{sb}^{AS} = E_{sb+}^{AS} + E_{sb-}^{AS} \tag{E.26}$$

$$= \Psi_0\frac{\Gamma}{2}\left\{\sin(\phi_s)\left[-e^{i\Omega t} + e^{-i\Omega t}\right] + \cos(\phi_s)\Phi(x,y)\left[-e^{i\Omega t} - e^{-i\Omega t}\right]\right\} \tag{E.27}$$

Again, we apply Euler's formula and using properties of odd and even functions we can cancel some of the sine and cosine terms

$$\therefore E_{sb}^{AS} = -\Psi_0\Gamma\left[\sin(\phi_s)\cdot i\sin(\Omega t) + \cos(\phi_s)\Phi(x,y)\cdot\cos(\Omega t)\right] \tag{E.28}$$

Heterodyne beat of carrier and sideband for fundamental mode

For the measurement, what we are really interested in, is the intensity modulation of the beat signal. This can be found by calculating $P = |E_{out}|^2$; where E_{out} is given by the combined sideband and carrier field at the output port. Therefore,

$$P_{out} = |E_{out}|^2 = |E_c^{AS} + E_{sb}^{AS}|^2 \tag{E.29}$$

Here we let $\delta = \sin(\frac{\phi_{DC}}{2})$, $A = \sin(\Omega t)\sin(\phi_s)$, and $B = \cos(\phi_s)\Phi(x,y)\cos(\Omega t)$ to make the calculation a bit easier. We can then write the beat signal as

$$\tag{E.30}$$

$$= (-i\Psi_0^*\delta + i\Psi_0^*\Gamma A + \Psi_0^*\Gamma B) \cdot (i\Psi_0\delta - i\Psi_0\Gamma A + \Psi_0\Gamma B) \tag{E.31}$$

where I have denoted the complex conjugate by the *

$$= \Psi_0^* \cdot \Psi_0 \left[(i\delta - iA\Gamma + \Gamma B) \cdot (-i\delta + i\Gamma A + \Gamma B) \right] \tag{E.32}$$

$$= P_0 \left[-i^2\delta^2 + i^2\Gamma A\delta + i\delta\Gamma B + i^2 A\Gamma\delta - i^2\Gamma^2 A^2 - iA\Gamma^2 B - i\delta\Gamma B + i\Gamma^2 AB + \Gamma^2 B^2 \right] \tag{E.33}$$

Canceling cross terms and evaluating factors of i we get. Note here that since the modulation depth is small (i.e. $\Gamma \ll 1$, almost all of the power is in the carier and first order sidebands, or $P_c + 2P_{sb} \approx P_0$. We can also ignore all second order terms in Γ since higher frequencies are filtered out by the detector bandwidth. Therefore the measured power at the output is

$$= P_0\delta^2 - 2P_0\Gamma A\delta \tag{E.34}$$

$$= P_0\sin(\frac{\Phi_{DC}}{2}) - 2P_0\Gamma\sin(\phi_s)\sin(\frac{\phi_{DC}}{2})\sin(\Omega t) \tag{E.35}$$

we are only interested in the first order term in Γ, which gives us the relative beat between the carrier and sideband fields at the modulation frequency. We can extract the phase information of the beat signal by demodulating (multiplying by sine and cosine) at the modulation frequency. Thus, we obtain the results given by Equations 5.5 and 5.6:

$$\mathcal{I}(\vec{x}, \vec{y}) = 0 \tag{E.36}$$

$$-\mathcal{Q}(\vec{x}, \vec{y}) = \Gamma p_{in}(\vec{x}, \vec{y})\sin(\frac{\Phi_{DC}}{2})\sin(\frac{\omega_s L_s}{c}) \tag{E.37}$$

Considering homodyne readout

As mentioned in Section 5.1, the proposed upgrade for A+ is to transition to a homodyne readout scheme. This will replace the the carrier field at the AS port produced by the DARM offset with a separate reference beam of equal amplitude. The injected reference beam at the AS port will be of the form:

$$E_{ref}^{AS} = \Psi_r \sin(\alpha_{HOM}) \tag{E.38}$$

where α_{HOM} is the phase of the reference beam. The combined reference and sideband field is then given by

$$E_{out} = \Psi_r \sin(\alpha_{HOM}) - \Psi_0 \left[\Gamma i \sin(\Omega t) \sin(\phi_s) + \cos(\phi_s) \Phi(x,y) \cos(\Omega t) \right] \tag{E.39}$$

Again, we let $A = \sin(\Omega t) \sin(\phi_s)$, and $B = \cos(\phi_s) \Phi(x,y) \cos(\Omega t)$

$$= \Psi_r \sin(\alpha_{HOM}) - \Psi_0 \Gamma (B + iA) \tag{E.40}$$

Calculating the power at the detector we get

$$P_{out} = |E_{out}|^2 = |E_{ref}^{AS} + E_{sb}^{AS}|^2 \tag{E.41}$$

$$= \left[\Psi_r^* \sin(\alpha_{HOM}) - \Psi_0^* \Gamma (B - iA) \right] \cdot \left[\Psi_r \sin(\alpha_{HOM}) - \Psi_0 \Gamma (B + iA) \right] \tag{E.42}$$

$$= \Psi_r^* \Psi_r \sin^2(\alpha_{HOM}) - \Psi_r^* \Psi_0 \Gamma \left[(B + iA) \sin(\alpha_{HOM}) \right] \tag{E.43}$$

$$- \Psi_0^* \Psi_r \Gamma \left[(B - iA) \sin(\alpha_{HOM}) \right] + \Psi_0^* \Psi_0 \Gamma^2 \left(B^2 + A^2 \right) \tag{E.44}$$

$$= |\Psi_r|^2 \sin^2(\alpha_{HOM}) + |\Psi_0|^2 \left(B^2 + A^2 \right) \Gamma^2 - 2\Psi_0^* \Psi_r \sin(\alpha_{HOM}) B \tag{E.45}$$

Again, we are only interested in the beat signal the modulation frequency Ω. Therefore, the RF beat term in a homodyne scheme is given by:

$$P_\Omega = -2\Psi_0^* \Psi_r \Gamma \sin(\alpha_{HOM}) \cdot \cos(\phi_s) \Phi(x,y) \cos(\Omega t) \tag{E.46}$$

Appendix F

Imaging of Multiple Modulation Frequencies with the CMOS phase camera

As discussed in Section 4.2.1, a flip-flop (FF) can be integrated with the CMOS phase camera to support four or six quad exposures. The flip-flop also allows the camera to subsequently image beat signals at different modulation frequencies. The electronic setup for this operation is shown in Fig. 49. An RF-switch is used to switch between the modulating frequencies of the local oscillators following the frame capture sequence governed by the microcontroller. The frequency and phase stepped output of the DDS are phase-locked by ensuring the updates are triggered on the rising edge of the local-oscillator by the flip-flop. The functionality of other elements in this scheme is the same as discussed in Section 4.2.1. This setup is particularly useful for application in Advanced LIGO, which allows the CMOS phase camera to image beat signals at 9 MHz and 45 MHz in real time. Using this technique, the CMOS phase camera can image beat signals at different modulation frequencies with a low-latency of 1 Hz.
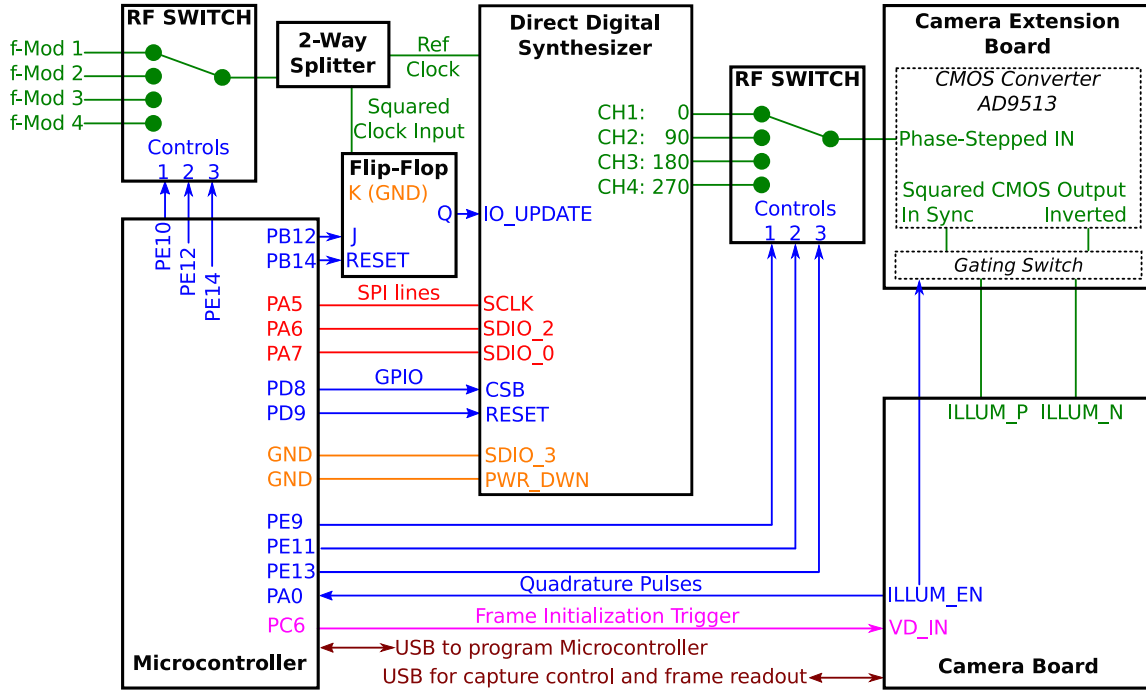
Figure 49: Alternate capture scheme mentioned in section §**??**. It allows simultaneous imaging of RF signals with different modulation frequencies by selecting a separate modulation frequencies for every frame. In this scheme, the microcontroller controls an additional RF switch at the input off the DDS board. A 2-way splitter is used to provide a clock signal input to a flip-flop circuit. The flip-flop ensures a phase-locked output from the DDS by triggering the DDS update on the rising edge of the external local oscillator. The rest of the design block functionality is the same as discussed in Fig. 30. The RF switch at the output of the DDS can be discarded if six sub-quads are desired for image capture. In this scenario, the DDS is configured to phase-step one particular channel in synchronization with the quadrature pulses received by the microcontroller.

Bibliography

[1] Erik Muñiz, Varun Srivastava, Subham Vidyant, and Stefan W. Ballmer. High frame-rate phase camera for high-resolution wavefront sensing in gravitational-wave detectors. *Phys. Rev. D*, 104:042002, Aug 2021.

[2] Aaron Buikema, Craig Cahillane, GL Mansell, CD Blair, R Abbott, C Adams, RX Adhikari, A Ananyeva, S Appert, K Arai, et al. Sensitivity and performance of the advanced ligo detectors in the third observing run. *Physical Review D*, 102(6):062003, 2020.

[3] S Hild, H Grote, J Degallaix, S Chelkowski, K Danzmann, A Freise, M Hewitson, J Hough, H Lück, M Prijatelj, and et al. Dc-readout of a signal-recycled gravitational wave detector. *Classical and Quantum Gravity*, 26(5):055012, Feb 2009.

[4] Rudolf Schwarte, Zhanping Xu, Horst-Guenther Heinol, Joachim Olk, and Bernd Buxbaum. New optical four-quadrant phase detector integrated into a photogate array for small and precise 3d cameras. In *Three-Dimensional Image Capture*, volume 3023, pages 119–128. International Society for Optics and Photonics, 1997.

[5] Analog Devices. *4-Channel, 500 MSPS DDS with 10-Bit DACs AD9959*, 2008. Rev. B.

[6] Aidan F Brooks, Gabriele Vajente, Hiro Yamamoto, Rich Abbott, Carl Adams, Rana X Adhikari, Alena Ananyeva, Stephen Appert, Koji Arai, Joseph S Areeda, et al. Point absorbers in advanced ligo. *Applied Optics*, 60(13):4047–4063, 2021.

[7] Junaid Aasi, BP Abbott, Richard Abbott, Thomas Abbott, MR Abernathy,

Kendall Ackley, Carl Adams, Thomas Adams, Paolo Addesso, RX Adhikari, et al. Advanced ligo. *Classical and quantum gravity*, 32(7):074001, 2015.

[8] F Acernese, M Agathos, K Agatsuma, D Aisa, N Allemandou, A Allocca, J Amarni, P Astone, G Balestri, G Ballardin, et al. Advanced virgo: a second-generation interferometric gravitational wave detector. *Classical and Quantum Gravity*, 32(2):024001, 2014.

[9] Benjamin P Abbott, Richard Abbott, TD Abbott, MR Abernathy, Fausto Acernese, Kendall Ackley, Carl Adams, Thomas Adams, Paolo Addesso, RX Adhikari, et al. Observation of gravitational waves from a binary black hole merger. *Physical review letters*, 116(6):061102, 2016.

[10] BP Abbott, Richard Abbott, TD Abbott, S Abraham, F Acernese, K Ackley, C Adams, RX Adhikari, VB Adya, C Affeldt, et al. Gwtc-1: a gravitational-wave transient catalog of compact binary mergers observed by ligo and virgo during the first and second observing runs. *Physical Review X*, 9(3):031040, 2019.

[11] R Abbott, TD Abbott, S Abraham, F Acernese, K Ackley, A Adams, C Adams, RX Adhikari, VB Adya, C Affeldt, et al. Gwtc-2: Compact binary coalescences observed by ligo and virgo during the first half of the third observing run. *arXiv preprint arXiv:2010.14527*, 2020.

[12] A Einstein. The foundations of the theory of general relativity. *Annalen der Physik*, pages 769–882, 1916.

[13] Albert Einstein. Über gravitationswellen. *SPAW*, pages 154–167, 1918.

[14] Felix AE Pirani. On the physical significance of the riemann tensor. *AcPP*, 15:389–405, 1956.

[15] Albert A Michelson and Edward W Morley. On the relative motion of the earth and of the luminiferous ether. *Sidereal Messenger, vol. 6, pp. 306-310*, 6:306–310, 1887.

[16] Rainer Weiss and Dirk Muehlner. Electronically coupled broadband gravitational antenna. *Quarterly Progress Report, Research Laboratory of Electronics*, 105, 1972.

[17] Tobin T Fricke, Nicolás D Smith-Lefebvre, Richard Abbott, Rana Adhikari, Katherine L Dooley, Matthew Evans, Peter Fritschel, Valery V Frolov, Keita Kawabe, Jeffrey S Kissel, et al. Dc readout experiment in enhanced ligo. *Classical and Quantum Gravity*, 29(6):065005, 2012.

[18] Tobin Thomas Fricke. Homodyne detection for laser-interferometric gravitational wave detectors. 2011.

[19] J Abadie, Benjamin P Abbott, R Abbott, Thomas D Abbott, M Abernathy, Carl Adams, R Adhikari, Christoph Affeldt, B Allen, GS Allen, et al. A gravitational wave observatory operating beyond the quantum shot-noise limit. *Nature Physics*, 7(12):962, 2011.

[20] Peter Fritschel, Matthew Evans, and Valery Frolov. Balanced homodyne readout for quantum limited gravitational wave detectors. *Optics express*, 22(4):4224–4234, 2014.

[21] Peter Fritschel, David Shoemaker, and Rainer Weiss. Demonstration of light recycling in a michelson interferometer with fabry–perot cavities. *Applied optics*, 31(10):1412–1418, 1992.

[22] Brian J Meers. Recycling in laser-interferometric gravitational-wave detectors. *Physical Review D*, 38(8):2317, 1988.

[23] Jun Mizuno, Kenneth A Strain, PG Nelson, JM Chen, Roland Schilling, Albrecht Rüdiger, Walter Winkler, and Karsten Danzmann. Resonant sideband extraction: a new configuration for interferometric gravitational wave detectors. *Physics Letters A*, 175(5):273–276, 1993.

[24] Eric D Black. An introduction to pound–drever–hall laser frequency stabilization. *American journal of physics*, 69(1):79–87, 2001.

[25] David H Reitze, Peter R Saulson, and Hartmut Grote. *Advanced Interferometric Gravitational-wave Detectors*. World Scientific, 2019.

[26] Anand Sengupta. The sensitivity of the advanced ligo detectors at the beginning of gravitational wave astronomy. 2016.

[27] Nergis Mavalvala, Daniel Sigg, and David Shoemaker. Experimental test of an alignment-sensing scheme for a gravitational-wave interferometer. *Applied optics*, 37(33):7743–7746, 1998.

[28] Peter Fritschel, Nergis Mavalvala, David Shoemaker, Daniel Sigg, Michael Zucker, and Gabriela González. Alignment of an interferometric gravitational wave detector. *Applied Optics*, 37(28):6734–6747, 1998.

[29] Dana Z Anderson. Alignment of resonant optical cavities. *Applied Optics*, 23(17):2944–2949, 1984.

[30] Euan Morrison, Brian J Meers, David I Robertson, and Henry Ward. Experimental demonstration of an automatic alignment system for optical interferometers. *Applied optics*, 33(22):5037–5040, 1994.

[31] Aninon Yariv. Optical electronics, cbs college publishing. *New York*, 50, 1985.

[32] Lisa Barsotti and Matt Evans. Modeling of alignment sensing and control for advanced ligo. *Technical note, LIGO*, 2010.

[33] Katherine Laird Dooley. *Design and performance of high laser power interferometers for gravitational-wave detection*. University of Florida, 2011.

[34] Rich Abbott, Rana Adhikari, Stefan Ballmer, Lisa Barsotti, Matt Evans, Peter Fritschel, Valera Frolov, Guido Mueller, Bram Slagmolen, and Sam Waldman. Advligo interferometer sensing and control conceptual design. *LIGO Technical Document, T070247-01-I*, 2008.

[35] Aidan F Brooks, Benjamin Abbott, Muzammil A Arain, Giacomo Ciani, Ayodele Cole, Greg Grabeel, Eric Gustafson, Chris Guido, Matthew Heintze, Alastair Heptonstall, et al. Overview of advanced ligo adaptive optics. *Applied optics*, 55(29):8256–8265, 2016.

[36] James C Wyant and Katherine Creath. Basic wavefront aberration theory for optical metrology. *Applied optics and optical engineering*, 11(part 2):28–39, 1992.

[37] Ryan Christopher Lawrence. *Active wavefront correction in laser interferometric gravitational wave detectors*. PhD thesis, Massachusetts Institute of Technology, 2003.

[38] D. Sigg. Sideband power levels. LHO alog 59058, May 2021.

[39] R. Schofield P. Nguyen. Vibration coupling at psl down by nearly 10 after itmy replacement; no change in ham5-6 coupling. LHO alog 58976, May 2021.

[40] Craig Cahillane. *Controlling and Calibrating Interferometric Gravitational Wave Detectors*. PhD thesis, California Institute of Technology, 2021.

[41] Carlton M Caves. Quantum-mechanical radiation-pressure fluctuations in an interferometer. *Physical Review Letters*, 45(2):75, 1980.

[42] Carlton M Caves. Quantum-mechanical noise in an interferometer. *Physical Review D*, 23(8):1693, 1981.

[43] Junaid Aasi, J Abadie, BP Abbott, Richard Abbott, TD Abbott, MR Abernathy, Carl Adams, Thomas Adams, Paolo Addesso, RX Adhikari, et al. Enhanced sensitivity of the ligo gravitational wave detector by using squeezed states of light. *Nature Photonics*, 7(8):613–619, 2013.

[44] Sheila Elizabeth Dwyer. *Quantum noise reduction using squeezed states in LIGO*. PhD thesis, Massachusetts Institute of Technology, 2013.

[45] L McCuller, SE Dwyer, AC Green, Haocun Yu, L Barsotti, CD Blair, DD Brown, A Effler, M Evans, A Fernandez-Galiana, et al. Ligos quantum response to squeezed states. *arXiv preprint arXiv:2105.12052*, 2021.

[46] Nutsinee Kijbunchoo. Squeezer installation and updates (part ii). Technical Report G1901583, LSC, 2019.

[47] Eric Glenn Oelker. *Squeezed states for advanced gravitational wave detectors*. PhD thesis, Massachusetts Institute of Technology, 2016.

[48] New Focus. *DC-250 MHz Electro-Optic Phase Modulators*, 2007. Rev. G.

[49] Keiko Kokeyama, Kiwamu Izumi, William Z Korth, Nicolas Smith-Lefebvre, Koji Arai, and Rana X Adhikari. Residual amplitude modulation in interferometric gravitational wave detectors. *JOSA A*, 31(1):81–88, 2014.

[50] Wan Wu. *Instrumentation of the next generation gravitational wave detector: triple pendulum suspension and electro-optic modulator*, volume 69. 2007.

[51] Edward A Whittaker, Manfred Gehrtz, and Gary C Bjorklund. Residual amplitude modulation in laser electro-optic phase modulation. *JOSA B*, 2(8):1320–1326, 1985.

[52] Fabian Magaña Sandoval, Thomas Vo, Daniel Vander-Hyde, J. R. Sanders, and Stefan W. Ballmer. Sensing optical cavity mismatch with a mode-converter and quadrant photodiode. *Phys. Rev. D*, 100:102001, Nov 2019.

[53] Thomas V Vo. *Adaptive Mode Matching in Advanced LIGO and Beyond.* PhD thesis, Syracuse University, 2019.

[54] Kazuhiro Agatsuma, Laura van der Schaaf, Martin Van Beuzekom, David Rabeling, and Jo van Den Brand. High-performance phase camera as a frequency selective laser wavefront sensor for gravitational wave detectors. *Optics express*, 27(13):18533–18548, 2019.

[55] Hang Yu. Script for decomposing camera images into hg modes. LHO alog 44008, September 2018.

[56] Miguel H. Conde. *Compressive Sensing for the Photonic Mixer Device.* Springer Vieweg, 2017.

[57] *Demodulation pixels in CCD and CMOS technologies for time-of-flight ranging*, volume 3965, 2000.

[58] Robert Lange. *3D time-of-flight distance measurement with custom solid-state image sensors in CMOS/CCD-technology.* PhD thesis, Universität Siegen, 2000.

[59] Terrence Cole Millar, Navid Sarhangnejad, Nikola Katic, Kyros Kutulakos, and Roman Genov. The effect of pinned photodiode shape on time-of-flight demodulation contrast. *IEEE transactions on Electron Devices*, 64(5):2244–2250, 2017.

[60] Samuel Osei Achamfuo-Yeboah. *Design and implementation of a CMOS Modulated Light Camera.* PhD thesis, University of Nottingham, 2012.

[61] Texas Instruments. *OPT8241 3D Time-of-Flight Sensor*, 6 2015. Rev. B.

[62] Texas Instruments. *Introduction to the Time-of-Flight (ToF) System Design*, 5 2014. Rev. D.

[63] Faisal Mufti and Robert Mahony. Statistical analysis of signal measurement in time-of-flight cameras. *ISPRS journal of photogrammetry and remote sensing*, 66(5):720–731, 2011.

[64] Mihail Georgiev, Robert Bregović, and Atanas Gotchev. Fixed-pattern noise modeling and removal in time-of-flight sensing. *IEEE Transactions on Instrumentation and Measurement*, 65(4):808–820, 2015.

[65] William Ralph Bennett. Spectra of quantized signals. *The Bell System Technical Journal*, 27(3):446–472, 1948.

[66] Charles Boncelet. Image noise models. In *The essential guide to image processing*, pages 143–167. Elsevier, 2009.

[67] Vlad Toronov, Enrico D'Amico, Dennis Hueber, Enrico Gratton, Beniamino Barbieri, and Andrew Webb. Optimization of the signal-to-noise ratio of frequency-domain instrumentation for near-infrared spectro-imaging of the human brain. *Optics Express*, 11(21):2717–2729, 2003.

[68] Holger Rapp, Mario Frank, Fred A Hamprecht, and B Jahne. A theoretical and experimental investigation of the systematic errors and statistical uncertainties of time-of-flight-cameras. *International Journal of Intelligent Systems Technologies and Applications*, 5(3-4):402–413, 2008.

[69] Application Note. Group and phase delay measurements with vector network analyzer zvr.

[70] S. Shrestha, F. Heide, W. Heidrich, and G. Wetzstein. Computational imaging with multi-camera time-of-flight systems. *ACM Trans. Graph. (SIGGRAPH)*, 2016.

[71] Ieee standard definitions of physical quantities for fundamental frequency and time metrology-random instabilities. *IEEE Std 1139-1999*, pages 1–40, 1999.

[72] M. Granata, C. Buy, R. Ward, and M. Barsuglia. Higher-order laguerre-gauss mode generation and interferometry for gravitational wave detectors. *Phys. Rev. Lett.*, 105:231102, Nov 2010.

[73] Ludovico Carbone, Paul Fulda, Charlotte Bond, Frank Brueckner, Daniel Brown, Mengyao Wang, Deepali Lodhia, Rebecca Palmer, and Andreas Freise. The generation of higher-order laguerre-gauss optical beams for high-precision interferometry. *JoVE (Journal of Visualized Experiments)*, (78):e50564, 2013.

[74] Evan D Hall, Kevin Kuns, Joshua R Smith, Yuntao Bai, Christopher Wipf, Sebastien Biscans, Rana X Adhikari, Koji Arai, Stefan Ballmer, Lisa Barsotti, et al. Gravitational-wave physics with cosmic explorer: limits to low-frequency sensitivity. *arXiv preprint arXiv:2012.03608*, 2020.

[75] M Punturo, M Abernathy, F Acernese, B Allen, Nils Andersson, K Arun, F Barone, B Barr, M Barsuglia, M Beker, et al. The einstein telescope: a third-generation gravitational wave observatory. *Classical and Quantum Gravity*, 27(19):194002, 2010.

[76] Koji Arai. On the accumulated round-trip gouy phase shift for a general optical cavity. *LIGO Technical Note*, 1300189:1–11, 2013.

Curriculum Vitae

Title of Dissertation

     A Solid-State Phase Camera for Advanced Gravitational-Wave Inteferometers

Full Name

     Erik A. Muñiz

Place and Date of Birth

     Anaheim, California   August 31, 1992

Colleges and Universities,	Years attended and degrees
California State University, Fullerton	2013–2015, B.S.
Syracuse University	2015–2021, Ph.D.

Publications

- Padilla, C., Fritschel, P., Magaña-Sandoval, F., Muniz, E., Smith, J.R. and Zhang, L., 2014. Low scatter and ultra-low reflectivity measured in a fused silica window. Applied optics, 53(7), pp.1315-1321.

- Muñiz, E., Srivastava, V., Vidyant, S., & Ballmer, S. W. (2021). High Frame-Rate Phase Camera for High-Resolution Wavefront Sensing in Gravitational-Wave Detectors. Phys. Rev. D, 104:042002.

Awards and Fellowships

2015-2019 Partnership in Astronomy & Astrophysics Research and Education (PAARE) Fellow

2014 Dan Black Scholarship

Major Department
   Physics